# Study of Microlensing Exoplanets with Combination of Light Curves and AO Images

Naoki Koshimoto

Department of Earth and Space Science,
Graduate School of Science,
Osaka University

February 1, 2018

**Abstract**

Gravitational microlensing is the only method that is capable of detecting exoplanets with a mass down to that of the Earth, beyond the snow line of their respective star. This region is thought to play a crucial role in planet formation and corresponds to the region including the orbits of Jupiter, Saturn, Uranus and Neptune in the solar system. When light is bent by a gravitational lens consisting of two objects, we can precisely measure the mass ratio between them from the analysis of the light curve, and thus can detect a planet. A difficulty associated with the microlensing method is in the measurement of the physical mass of the lens system (host star + planet). In microlensing, there are up to three observable quantities that can be used to calculate the mass–distance relations of the lens: the Einstein angular radius; the microlens parallax; and the lens flux. If any two of these are measured, we can break the degeneracy between the lens mass and the distance to the lens. However, not all of these variables are always measured. Compared to the former two observables, the lens flux can be obtained even after the end of an event by imaging the lens and source stars with high-angular resolution using an adaptive optics (AO) system, or observation from space. The requirement of a high-angular resolution observation comes from the fact that our observation field of the Galactic bulge is too dense to resolve other stars unrelated to the microlensing event by seeing-limited observations.

In this thesis, the analysis of two planetary microlensing events, OGLE-2012-BLG-0950 and MOA-2016-BLG-227, is presented. Each event is observed by the Keck telescope with an AO system, and we find an excess flux at the position of the source star in each of the images. Even with the AO observations, we need to consider the possibility that the excess flux is not due to the lens, but due to a companion to the source or lens star, or an unrelated star. For OGLE-2012-BLG-0950, we conclude that, from the evaluation of the possibilities in previous studies, a large fraction of the excess flux originates from the lens. Combining the lens flux and the microlens parallax measured in the light curve reveals that the planet has a mass of $M_{\rm p} = 35^{+17}_{-9} M_{\oplus}$ and an orbit at a planet-host projected separation of $r_{\perp} = 2.7^{+0.6}_{-0.7}$ AU around its host star, which has a mass of $M_{\rm host} = 0.56^{+0.12}_{-0.16} M_{\odot}$. This is the first mass measurement made only from the microlens parallax and the lens flux. The planet mass is located in a valley of the mass distribution histogram of planets discovered to date. In contrast to the core accretion theory, which predicts a moderate abundance of such planets outside the snow line, this is the second planet observed through microlensing with a reliable mass measurement discovered so far in the region. In contrast, using a Bayesian analysis, a new method was applied to MOA-2016-BLG-227 to evaluate the probability of contamination. We

find that it is unlikely that a large fraction of the excess flux comes from the lens, unless solar-type stars are much more likely to host planets of this mass ratio than lower mass stars. Nevertheless, our conclusion is that the lens system consists of either an M or K-dwarf host star with a gas-giant planet located in the Galactic bulge, regardless of the dependency of planet hosting probability on the host mass. Such systems are predicted to be rare by the core accretion theory of planet formation.

# Contents

# List of Figures

# List of Tables

# Chapter 1

# Introduction

Until the first detection of an exoplanet in 1995, planet formation theories were based on the formation of the Solar System. The standard core accretion model (Safronov 1972, Hayashi et al. 1985, Lissauer 1993) was believed to be fairly well established, although some problems, such as the formation of planetesimals (Weidenschilling & Cuzzi 1993, Dominik & Tielens 1997:e.g.), remained. According to this theory, the solar system planets are formed by the following scenario:

1. Dust and gas with angular momenta in the molecular cloud form into a protoplanetary disk around a protostar when the star is formed;
2. Dusts in the disk settle to the center plane and ∼km sized planetesimals are formed by the buildups;
3. Planetesimals gradually grow through several collisions and coalescence, and eventually become massive bodies;
4. The massive bodies gravitationally capture planetesimals and grow into protoplanets. (Formation of rocky planets);
5. Some protoplanets are sufficiently massive to capture all of the gas in the vicinity ($M \gtrsim 10M_{\oplus}$) and grow further into gas giants. (Formation of gas giants);
6. Gas in disk are dispersed completely;
7. Planets with mass of $M \gtrsim 10M_{\oplus}$ are formed at a large distance from the host star after the gas has dispersed. (Formation of ice giants).

In this scenario, dust is the material of protoplanets, and gas giants, such as Jupiter or Saturn, are formed slightly outside the "snow line" where the protoplanetary disk becomes sufficiently cold for water to condense, i.e., to become one of the

component materials. However, this theory did not predict the discovery of "Hot Jupiters," which are gas giants with orbits far inside the snow line. The hot Jupiter 51 Peg b (Mayor & Queloz 1995) was the first detected exoplanet orbiting a star at a distance closer than Mercury, but has around one Jupiter mass. Since then, over 3600 exoplanets have been detected. The five main methods of detecting planets used today are explained below.

- Radial Velocity Method

  A bound planet causes its host star to move into a Keplerian orbit around the common center of mass. The radial velocity method detects the slight variation of the line-of-sight velocity of the star induced by its planet, using the Doppler shift of absorption lines (Butler et al. 2006, Bonfils et al. 2013). About 20% of all detected planets, including the first exoplanet (Mayor & Queloz 1995), have been detected by this method. Because only line-of-sight velocities can be measured, only a lower limit for the mass $M_{\rm P} \sin i$ can be inferred, because the orbital inclination is not *a priori* known. With increasing distance from the host star, the amplitude and the period of radial velocity variation - induced by a planet - decreases and increases, respectively. For this reason, the radial velocity method is sensitive to close and relatively massive planets.

- Transit Method

  The transit method detects planets by observing periodic variations in the stellar flux, caused by planetary eclipses (Borucki et al. 2011). The proportion of the decrease enables us to know the planet's diameter compared to the star. An eclipse requires the orbital plane of the planet to be perfectly aligned with the line of sight of the observer. The probability for this to occur decreases with increasing distance from the host star. For this reason, planets that have a relatively small semimajor axis are more likely to be detected by this method, just as is the case with the radial velocity method. Because the orbital inclination of a transit planet is $i \simeq 90°$, we can know both its mass and diameter by combining the results from radial velocity observation.

  More than 2700 planets have been detected by this method. Most of them were detected by the *Kepler* space telescope, and a large fraction of them are objects with known planetary radii from transit studies, but have an undetermined mass. This is because a spectroscopic observation, which is needed for the radial velocity measurement, requires more flux from a target compared to a photometric observation, which is needed for the transit method. Therefore, only relatively bright (i.e., close) host stars detected by transit method can also be observed by the radial velocity method.

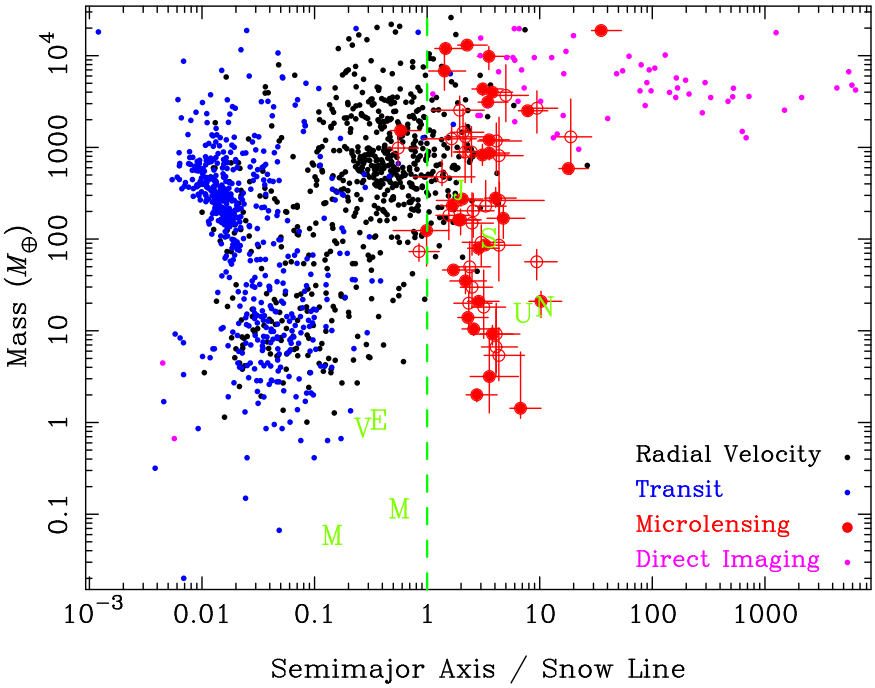


Figure 1.1: Mass versus host star-planet separation distribution of exoplanets which have been detected so far. The horizontal axis is the semimajor axis normalized by the snow line, which is assumed to depend on the host star's mass as $\sim 2.7\,\mathrm{AU}\,(M/M_\odot)$ (Kennedy & Kenyon 2008). The color of a dot corresponds to the method of its detection. A green letter indicates a solar system planet by its initial. Note that some fraction of exoplanets that have been discovered by the transit method is not on this plot due to a lack of their mass measurements.

- Gravitational Microlensing Method

  Gravitational microlensing is a phenomenon that causes the temporal magnification of a source object. It occurs when a foreground lens object happens to pass close to our line of sight with the source object, and its gravitational field bends the light from the source. The gravitational microlensing method uses this phenomenon to detect planets (Mao & Paczynski 1991, Gould & Loeb 1992). If the lens is a single star, the light curve of the variation in source magnification follows a symmetrical curve (Paczynski 1986). If the lens star has a planet in a suitable location, the planet's gravitational field will also perturb the source's light path, and the light curve shows an anomaly. We can understand the planet's nature through observing and analyzing the anomaly, as will be discussed in Chapter 2. The gravitational microlensing method is capable of discovering planets with a mass down to

that of the Earth, just outside of the snow line (Bennett & Rhie 1996). The number of planets detected through this method is about 50 by now, but still much less compared to the radial velocity method or transit method. However, in terms of the sensitivity region, it is very important for planetary formation theory that the microlensing method is complementary to the other methods, as is shown in Figure 1.1. Additionally, because microlensing does not rely upon any light from the host star or the planet of the lens system for detection, it is possible to detect planets around stars that are too faint to detect by the other methods (Bennett et al. 2008), and even a planetary-mass object that belongs to no host star at all, a so-called free-floating planet (Sumi et al. 2011, Mróz et al. 2017).

- Direct Imaging Method

  Although the amount of information about the planet that can be obtained by direct detection of the planet's light is much larger than by other methods, astronomers were so far more successful with indirect methods, because the bright host star drowns out the faint light emitted by (or reflected off) planets. However, by using modern methods for high-contrast imaging (e.g. ADI/LOCI, SDI, PDI) and technological developments in coronagraphy, it has become increasingly possible to increase the contrast for these observations. Especially young stellar objects are targeted as the infrared contrast between planets and stars is more favorable. About 50 planets have been detected by the direct imaging so far (Marois et al. 2008).

- Astrometry Method

  This method is historically the oldest method for exoplanet discovery. As of 1855, the astrometric calculation for an extrasolar planet was done by Jacob (1855). However, although several papers have claimed the discovery of exoplanet via the astrometry method (Pravdo & Shaklan 2009, Muterspaugh et al. 2010), so far, the existence of these planets has been ruled out, or not confirmed by other methods. Nevertheless, the astrometry method should be noted as one of the main methods of detecting exoplanets because over 10000 gas giants with $\sim$ yr period are expected to be detected by the ongoing ESA's Gaia satellite mission (Perryman et al. 2014) which has observed over a billion stars from space since 2014. This method detects the wobble of the host star around the common center of the mass due to the motion of a planet, while the radial velocity method uses the different component of the star' s motion, which is along the line of sight. In contrast to the radial velocity method, which detects the derivative of the position of the host star, the astrometry method uses the position itself. This results in a different sensitivity region compared to the radial velocity method, i.e.,

planets with large orbital period produce a large amplitude wobble in the host's motion. In 2016, the first catalog of the Gaia mission, based on its observations between July 2014 and September 2015, was released. This includes the positions and magnitudes for all sources with acceptable errors, and some other information, such as parallax and proper motion for some part of the sources. According to the Gaia webpage[1], the exoplanet list will be included in their final release for the nominal mission planned for the end of 2022.

The core accretion model was originally developed to explain the formation of our Solar System, but it has not predicted planetary systems different from our own, which are revealed through the above detection methods. It now includes the possibility of migration (Lin et al. 1996) to explain Hot Jupiters, but it still has difficulty explaining the entire population of exoplanets.

For example, the theoretical prediction of a paucity of the planets with masses of 5 - 30 $M_\oplus$ in short period orbits (Ida & Lin 2004, Ida et al. 2013) is inconsistent with the results from radial velocity studies (Howard et al. 2010). Also, a recent statistical study on microlensing planets by Suzuki et al. (2016) found a peak or break of the planet frequency in the mass ratio function beyond the snow line. The peak is at $q_{\rm br} = 1.7 \times 10^{-4}$ corresponding to 10 - 40 $M_\oplus$ for the host mass of 0.2 - 0.8 $M_\odot$. Although the theoretical simulations by Ida et al. predict some population of planets with this mass range beyond the snow line, they predict higher frequency for lower mass planets and do not predict the detected peak. Moreover, while the current core accretion model predicts a few gas giants orbiting a red dwarf at any separation (Laughlin et al. 2004, Kennedy & Kenyon 2008) - and this is confirmed by observations from the radial velocity method for massive gas giants orbiting inside the snow line (Endl et al. 2006, Johnson et al. 2007, Cumming et al. 2008, Johnson et al. 2010), the gravitational microlensing method has revealed several gas-giants orbiting just outside of the snow line of their late type host stars (e.g., Dong et al. 2009a,b, Batista et al. 2011, Koshimoto et al. 2014). However, a quantitative analysis of planetary frequency as a function of host star mass has not yet been completed.

This thesis is organized as follows. Chapter 2 describes the basics of gravitational microlensing. The analyses of OGLE-2012-BLG-0950 and MOA-2016-BLG-227 are presented in Chapters 3 and 4, respectively. These two chapters were published as Koshimoto et al. (2017a) and Koshimoto et al. (2017b), respectively. There are some overlapping explanations throughout this thesis. However, they were not edited as to retain the context of the discussion of each paper. Chapter 5 summarizes the results of the two works and gives further discussions. Appendix A

[1] https://www.cosmos.esa.int/web/gaia/release

is an introduction of the annual parallax effect. Appendices B and C corresponds to those of Koshimoto et al. (2017a) and Koshimoto et al. (2017b), respectively.

# Chapter 2

# Gravitational Microlensing

Einstein's general theory of relativity said that light rays bend in a gravitational field. Due to this effect, light from a source object is bent by gravitational fields around a lens object along its path, and its image appears separated and/or distorted. In this case, the gravitational fields act just like a lens, and, therefore, this phenomenon is called a gravitational lens effect. This can be considered as an astronomical phenomenon because it is significant when both the source and the lens are on the scale of celestial bodies, or more massive. In case that the mass of a lens object is on the scale of a galaxy or a galaxy cluster, images of the source objects can be observed separately. On the other hand, in case that a lens object is a star or a planet, the elongation between images is too small to be resolved. Instead, the phenomenon is identified as an instantaneous magnification of the source object. Gravitational lens effects like this are called gravitational microlensing effects. In this section, the basics of the gravitational microlensing effect is described, and its application for detections of planets.

## 2.1 The Lens Equation and Light Curve

While optical convex lenses concentrate all parallel light passing through them into a single focus, creating a single image, the gravitational lenses bend differently and so create elongated, or multiple images. The total area of all separated or merged images is larger than that of its original image without the lens. Hence, it appears magnified. Below is the lens equation, which shows the general case of how the gravitational field of lens objects creates images. This is then expanded on to describe, firstly, the case where the lens is either a single point mass (single lens event), or, secondly, where the lens is a two point mass system (binary lens event).

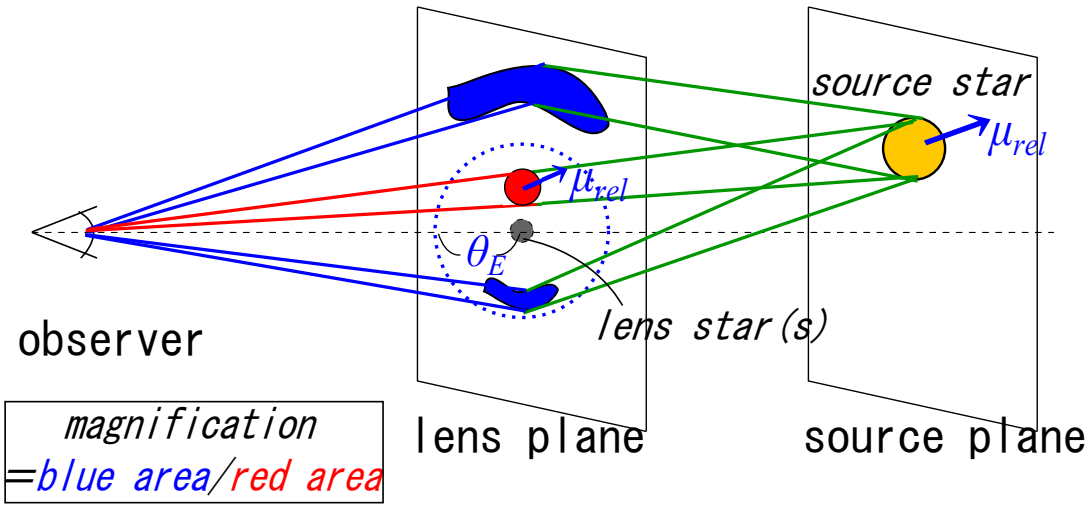


Figure 2.1: Schematic illustration of the magnification by a single lens. When the projection of the source star (red circle) passes an area within the angular Einstein radius, $\theta_E$, from the lens star in the lens plane, the light from the source follows the blue path and is magnified. $\theta_E$ is typically $\theta_E \sim$ 300-400$\mu$arcsec. This means the lens and source align along the line of sight. Note that $\mu_{rel}$ is the lens-source relative proper motion.

### 2.1.1 The Lens Equation

According to the theory of general relativity, light rays passing at a distance of $r_m$ from a point mass with mass of $M$ will be bent by an angle (Schneider et al. 1992),

$$\alpha(r_m) = \frac{4GM}{r_m c^2} \quad (r_m \gg \frac{2GM}{c^2}). \tag{2.1}$$

The planes normal to the line of sight toward both the lens star and source star, like Figure 2.1, are referred to as a lens plane and a source plane, respectively. As shown in Figure 2.2, the $\xi_x, \xi_y$ axes are defined on a lens plane and the $\eta_x, \eta_y$ axes are defined on a source plane, where $D_S$ and $D_L$ are distances to the source and to the lens from the observer, respectively. $D_{LS}$ is the distance between the lens and the source. When a mass point of mass $dM$ is located at $\boldsymbol{\xi'}$ on the lens plane, a light ray passing through $\boldsymbol{\xi}$ bends following Equation (2.1),

$$d\boldsymbol{\alpha}(\boldsymbol{\xi}) = \frac{4G\,dM}{c^2} \frac{\boldsymbol{\xi} - \boldsymbol{\xi'}}{|\boldsymbol{\xi} - \boldsymbol{\xi'}|^2}. \tag{2.2}$$

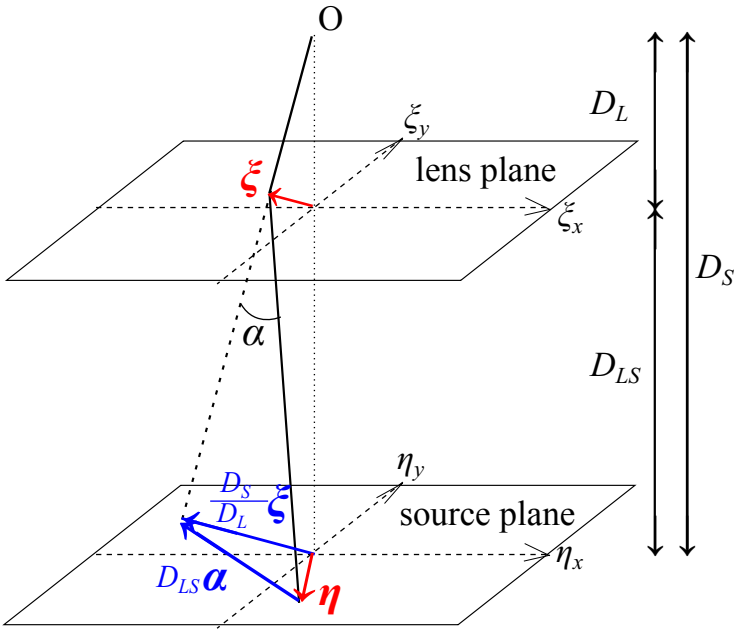


Figure 2.2: Geometry of a microlensing event. O and $\boldsymbol{\eta}$ indicate an observer and the source object, respectively. The lens object is distributed near the lens plane. The observed images are located at $\boldsymbol{\xi}$ on the lens plane.

When a lens object has a surface mass density projected onto a lens plane, $\Sigma(\boldsymbol{\xi'})$, the deflection angle is derived by the integration of Equation (2.2) as

$$\boldsymbol{\alpha}(\boldsymbol{\xi}) = \int \frac{4G\,dM}{c^2}\frac{\boldsymbol{\xi}-\boldsymbol{\xi'}}{|\boldsymbol{\xi}-\boldsymbol{\xi'}|^2} \tag{2.3}$$

$$= \frac{4G}{c^2}\int_{S_L}\frac{(\boldsymbol{\xi}-\boldsymbol{\xi'})\Sigma(\boldsymbol{\xi'})}{|\boldsymbol{\xi}-\boldsymbol{\xi'}|^2}d^2\boldsymbol{\xi'} \tag{2.4}$$

where the integral area $S_L$ is all regions of the lens plane. Here, we assume that the spread of the lens object along the normal direction to the lens plane is much less than $D_L$ (thin lens approximation).

The relationship between the source position $\boldsymbol{\eta}$ and the image positions on the lens plane $\boldsymbol{\xi}$ are driven geometrically, as shown in Figure 2.2,

$$\boldsymbol{\eta} = \frac{D_S}{D_L}\boldsymbol{\xi} - D_{LS}\boldsymbol{\alpha}(\boldsymbol{\xi}). \tag{2.5}$$

By dividing this equation by $D_S$, the lens equation is defined as follows,

$$\frac{\boldsymbol{\eta}}{D_S} = \frac{\boldsymbol{\xi}}{D_L} - \frac{D_{LS}}{D_S}\boldsymbol{\alpha}(\boldsymbol{\xi}). \tag{2.6}$$

### 2.1.2 Single Lens

#### The Lens Equation and Positions of The Images for Single Lens

Consider the case that the lens object is a single star. As the size of the effective area of the gravitational field, $R_E$, is much larger than the physical size of star, we can approximate the lens is the point mass at the origin on the lens plane, $\Sigma(\boldsymbol{\xi'}) = M_L\delta(\boldsymbol{\xi'})$. Therefore, the angle of refraction takes the form

$$\boldsymbol{\alpha}(\boldsymbol{\xi}) = \frac{4GM_L}{c^2}\frac{\boldsymbol{\xi}}{|\boldsymbol{\xi}|^2}. \tag{2.7}$$

By substituting this formula into the lens equation (2.6) and dividing the both sides by the angular Einstein radius

$$\theta_E = \frac{R_E}{D_L} = \frac{1}{D_L}\sqrt{\frac{4GM_LD_S}{c^2}\nu(1-\nu)}, \qquad (\nu = \frac{D_L}{D_S}) \tag{2.8}$$

the lens equation can be written as,

$$\begin{aligned}\boldsymbol{u} &= \boldsymbol{x} - \boldsymbol{\alpha}(\boldsymbol{x}) \\ &= \boldsymbol{x} - \frac{\boldsymbol{x}}{|\boldsymbol{x}|^2}. \qquad (\boldsymbol{x} = \frac{\boldsymbol{\xi}}{R_E}, \boldsymbol{u} = \nu\frac{\boldsymbol{\eta}}{R_E})\end{aligned} \tag{2.9}$$

We can calculate positions of images for a given source position, $\boldsymbol{u}$, by solving Equation (2.9) for $\boldsymbol{x}$. In a single lens case, $\boldsymbol{x}$ runs parallel with $\boldsymbol{u}$, and the lens equation (2.9) can be rewritten in a simple quadric scalar form as follows,

$$x^2 - ux - 1 = 0 \tag{2.10}$$

with solutions of

$$x_\pm = \frac{u \pm \sqrt{u^2+4}}{2}. \tag{2.11}$$

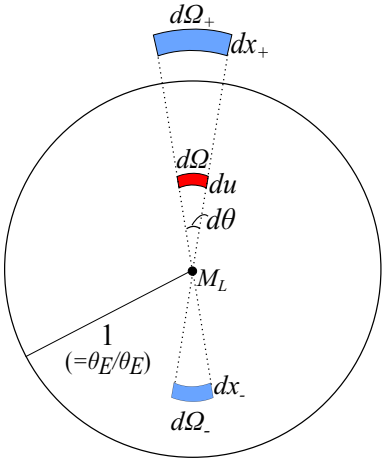


Figure 2.3: Images created by single lens. The source object with an infinitesimal solid angle of $d\Omega$ are indicated in red, and the two created images, with infinitesimal solid angles of $d\Omega_+$ and $d\Omega_-$ at $x_+$ and $x_-$, are indicated in blue.

This means that the two images are created
at $x_+$ and $x_-$ on a straight line joining the lens object and the source object on the surface of a celestial sphere (see Figure 2.3).

In the case of $\boldsymbol{u} = 0$, Equation (2.9) becomes

$$\boldsymbol{x} - \frac{\boldsymbol{x}}{|\boldsymbol{x}|^2} = 0. \tag{2.12}$$

The solution of this equation is $|x_\pm| = 1$, with no constraint on the direction, i.e., a circle image with a radius of unity. This ring image is called the Einstein ring, which appears at the moment of $\boldsymbol{u} = 0$, i.e., when the source and lens are exactly aligned. Its radius on the lens plane, $R_E = \theta_E D_L$, is called Einstein radius. The size of Einstein radius, $R_E$, and the angular Einstein radius, $\theta_E$, are

$$R_E \simeq 2\,\mathrm{AU} \left(\frac{M_L}{0.3\,M_\odot}\right)^{1/2} \left(\frac{D_S}{8\,\mathrm{kpc}}\right)^{1/2} \left\{\frac{\nu}{0.75}\left(\frac{1-\nu}{1-0.75}\right)\right\}^{1/2} \tag{2.13}$$

and

$$\theta_E = \frac{R_E}{D_L} \simeq 320\,\mu\mathrm{arcsec} \left(\frac{M_L}{0.3\,M_\odot}\right)^{1/2} \left(\frac{D_S}{8\,\mathrm{kpc}}\right)^{-1/2} \left(\frac{(1-\nu)/(1-0.75)}{\nu/0.75}\right)^{1/2}. \tag{2.14}$$

As seen in the next section, typical microlensing events have values of $0 < u \lesssim 1 \Leftrightarrow 2 < |x_+ - x_-| \lesssim \sqrt{5}$. Hence, the elongation between two images expressed in $|x_+ - x_-|$ have the same order as $\theta_E$ of Equation (2.14), up to $\sim$1 marcsec. It is too small to be resolved by any telescopes with optical or near-infrared cameras today.

### Magnification and Light Curve for Single Lens

In order to consider the magnification by single lens simply, let's assume that the source object has an infinitesimal solid angle of $d\Omega$, as indicated in Figure 2.3. In this case, the magnification $A(u)$ is equal to the area ratio between the source and images (see Fig 2.1), that is,

$$\begin{aligned} A(u) &= \frac{d\Omega_+}{d\Omega} + \frac{d\Omega_-}{d\Omega} \\ &= \frac{x_+ d\theta dx_+}{u d\theta du} + \frac{x_- d\theta dx_-}{u d\theta du} \\ &= \frac{u^2+2}{u\sqrt{u^2+4}} \simeq \frac{1}{u} \quad (u \ll 1). \end{aligned} \tag{2.15}$$

In the case of the single lens, the magnification, $A(u)$, monotonically decreases with respect to $u$. The magnification of $A = 1.34$ at $u = 1$ is often used as the threshold to detect the microlensing event, considering the typical photometric uncertainty of the ground base 1 m class telescopes. Therefore, it is usually called a microlensing event when the source enters into the Einstein ring of a lens object, as in Figure 2.1. The magnification diverges to infinity at $u = 0$.

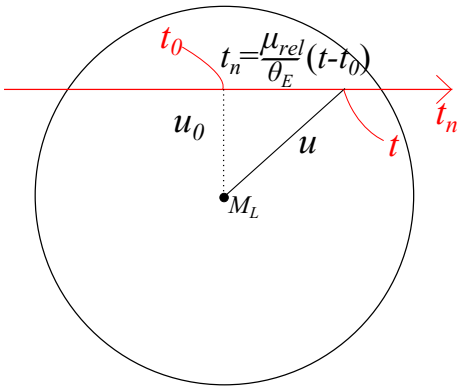


Figure 2.4: Source trajectory on the celestial sphere surface. The red line indicates the source trajectory. The black dot indicates the lens position. The black circle represents the Einstein radius.

In general, the source, lens and observer have some relative velocity to each other, and the magnification varies over the time for the galactic objects. In the simplest model, one can approximate that a source object travels with a uniform linear motion, with lens-source relative proper motion, $\mu_{rel}$, as shown in Figure 2.4. In this case, the time variation of $u(t)$ can be geometrically given by,

$$u(t) = \sqrt{u_0^2 + t_n^2} = \sqrt{u_0^2 + \left(\frac{\mu_{rel}}{\theta_E}(t - t_0)\right)^2}$$
$$= \sqrt{u_0^2 + \left(\frac{t - t_0}{t_E}\right)^2} \tag{2.16}$$

where $t_0$ is the time of the source's closest approach to the lens object, and $u_0$ is the minimum impact parameter. $t_E$ is defined as the duration of the source crossing the Einstein radius,

$$t_E \equiv \frac{\theta_E}{\mu_{rel}} = \frac{1}{\mu_{rel}}\sqrt{\frac{4GM_L}{c^2 D_S}\frac{1-\nu}{\nu}} \tag{2.17}$$

and is called the Einstein radius crossing time, or just an event timescale. Additionally, $t_n$ is defined as

$$t_n = \frac{\mu_{rel}}{\theta_E}(t - t_0) = \frac{t - t_0}{t_E}. \tag{2.18}$$

By substituting Equation (2.16) into Equation (2.15), the magnification $A(t)$ forms

$$A(t) = \frac{t_n^2 + u_0^2 + 2}{\sqrt{t_n^2 + u_0^2}\sqrt{t_n^2 + u_0^2 + 4}}. \tag{2.19}$$

This light curve is symmetrical in time about $t_0$, and its peak magnification increases with the decreasing value of $u_0$ (Figure 2.5).

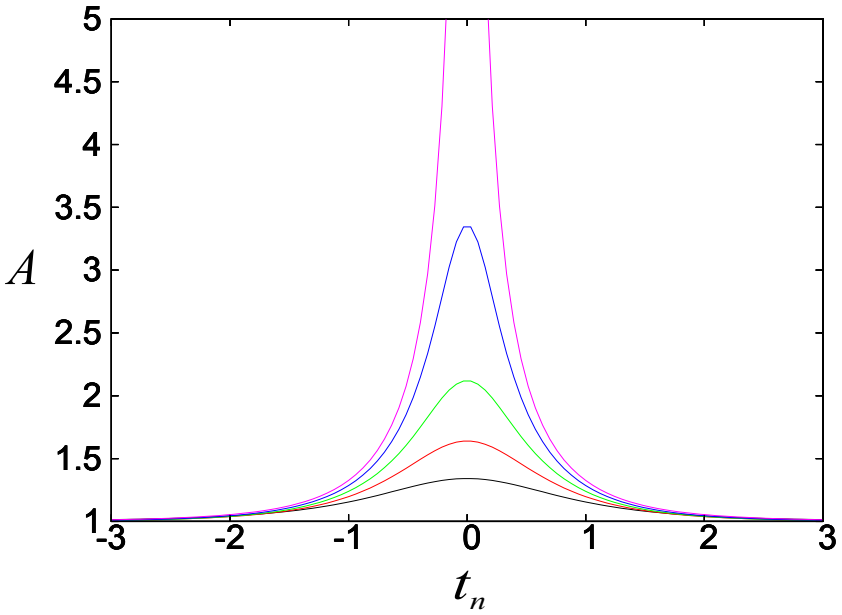


Figure 2.5: Light curves of single lens events. The light curve with $u_0 = 1, 0.7, 0.5, 0.3, 0.1$ are drawn from the bottom to the top, respectively.

#### Observables of Single Lens Event

When a single lens event is observed, we can obtain event parameters by fitting Equation (2.19) to the light curves. The fitting parameters of Equation (2.19) are $(t_E, t_0, u_0)$. Only $t_E$ includes the physical lens information, where the distance to the lens object $D_L$, the lens mass $M_L$, and the relative proper motion $\mu_{rel}$ degenerate in $t_E$ and cannot be determined uniquely. In most cases, the distance to the source object, $D_S$, is assumed to be $\sim 8$ kpc as the probability of microlensing event with the source stars around the galactic center is highest.

### 2.1.3 Binary Lens

A microlensing event caused by two lens objects is called a binary lens event. The probability that two random, unrelated stars in the Galactic bulge and disk are aligned to the line of sight of another star is extremely low ($\sim 10^{-6}$). Thus, the existence of two lens objects in a single event implies that these lens objects are gravitationally bound, such as in a binary or planetary system. The most notable feature of binary lens events is that there are a number of points on a source plane where the magnification diverges as follows.

**The Lens Equation and Images for Binary Lens**

Consider two lens objects. Put their center of mass on the origin of a lens plane of $\boldsymbol{\xi}$, and take their projected positions on the plane as $\boldsymbol{\xi_{L1}}, \boldsymbol{\xi_{L2}}$, aligned on $\xi_x$ axis. The total mass is defined as $M_L$, and their fractional mass is $\mu_1 : \mu_2$ ($\mu_1 + \mu_2 = 1$). In practice, one can safely assume the lenses are point masses, $\Sigma(\boldsymbol{\xi'}) = \mu_1 M_L \delta(\boldsymbol{\xi'} - \boldsymbol{\xi_{L1}}) + \mu_2 M_L \delta(\boldsymbol{\xi'} - \boldsymbol{\xi_{L2}})$. By following the case of the single lens, we can derive the binary lens equation as

$$\boldsymbol{u} = \boldsymbol{x} - \mu_1 \frac{\boldsymbol{x} - \boldsymbol{x_{L1}}}{|\boldsymbol{x} - \boldsymbol{x_{L1}}|^2} - \mu_2 \frac{\boldsymbol{x} - \boldsymbol{x_{L2}}}{|\boldsymbol{x} - \boldsymbol{x_{L2}}|^2} \quad (\boldsymbol{x_{Li}} = \frac{\boldsymbol{\xi_{Li}}}{R_E}, \boldsymbol{u} = \nu \frac{\boldsymbol{\eta}}{R_E}). \tag{2.20}$$

However, we can no longer follow the discussion of the case of single lens because $\boldsymbol{u}$ and $\boldsymbol{x}$ are not parallel, and we cannot consider it in one dimension. Because it is complicated to continue the discussion with vectors in general, below we use an alternative method using complex scalar numbers. Replacing the source plane $(u_x, u_y)$ with the source complex plane $(w_x, w_y)$ that includes a source object at $w$, and the lens plane $(x_x, x_y)$ with the lens complex plane $(z_x, z_y)$ that includes 2 lens objects at $z_{L1}, z_{L2}$ and created images at $z$. The binary lens equation (2.20) can then be rewritten as

$$w = z - \frac{\mu_1}{\overline{z} - \overline{z_{L1}}} - \frac{\mu_2}{\overline{z} - \overline{z_{L2}}}. \tag{2.21}$$

This equation includes not only $z$ but also $\overline{z}$. In order to remove $\overline{z}$, $\overline{z}$ must be isolated using the conjugate of Equation (2.21),

$$\overline{w} = \overline{z} - \frac{\mu_1}{z - z_{L1}} - \frac{\mu_2}{z - z_{L2}} \tag{2.22}$$

and substituting it into Equation (2.21), the complex lens equation for only $z$,

$$\begin{aligned}
&(z-w)\{(\overline{w} - \overline{z_{L1}})(z - z_{L1})(z - z_{L2}) + \mu_1(z - z_{L2}) + \mu_2(z - z_{L1})\} \\
&\quad \times \{(\overline{w} - \overline{z_{L2}})(z - z_{L1})(z - z_{L2}) + \mu_1(z - z_{L2}) + \mu_2(z - z_{L1})\} \\
&+\mu_1(z - z_{L1})(z - z_{L2})\{(\overline{w} - \overline{z_{L2}})(z - z_{L1})(z - z_{L2}) + \mu_1(z - z_{L2}) + \mu_2(z - z_{L1})\} \\
&+\mu_2(z - z_{L1})(z - z_{L2})\{(\overline{w} - \overline{z_{L1}})(z - z_{L1})(z - z_{L2}) + \mu_1(z - z_{L2}) + \mu_2(z - z_{L1})\} = 0
\end{aligned} \tag{2.23}$$

is obtained. This is a 5th-order polynomial equation for $z$, and shows that a binary lens creates 5 images at max. In fact, 3 images are created outside the caustic, and 5 images are created inside the caustic (see below about the caustic.). It is difficult to solve this equation analytically. We solve this equation numerically instead.

### Critical Curves and Caustics

The complex lens equation (2.21) represents the mapping of the source plane onto the lens plane, i.e., the mapping of $w \to z$. Therefore, when $\det J$ is defined as the Jacobian of $z \to w$:

$$\det J = \left|\frac{\partial w}{\partial z}\right|^2 - \left|\frac{\partial w}{\partial \overline{z}}\right|^2 \tag{2.24}$$

$$= 1 - \left|\frac{\mu_1}{(z - z_{L1})^2} + \frac{\mu_2}{(z - z_{L2})^2}\right|^2, \tag{2.25}$$

the magnification $A$ is the sum of the contribution from all images created,

$$A = \sum_{i=1}^{n} \frac{1}{\det J_i}, \tag{2.26}$$

where $\det J_i$ is the value of Equation (2.25) for the $i$th image position $z_i$, which satisfies Equation (2.21) when $n = 3$ or 5.

We can find that the magnification diverges to infinity when $\det J = 0$, that means that, from Equation (2.25),

$$\left|\frac{\mu_1}{(z - z_{L1})^2} + \frac{\mu_2}{(z - z_{L2})^2}\right|^2 = 1 \tag{2.27}$$

$$\Rightarrow \frac{\mu_1}{(z - z_{L1})^2} + \frac{\mu_2}{(z - z_{L2})^2} = e^{-i\varphi}, \quad \varphi \in [0, 2\pi) \tag{2.28}$$

This formula can be reduced to a 4th-order polynomial by clearing its fractions. Four curves of $z_a(\varphi), \ldots, z_d(\varphi)$ are obtained as its solutions, which are the critical curves. By mapping the critical curves to the source plane using the lens equation (2.21), we can obtain the corresponding four curves of $w_a(\varphi), \ldots, w_d(\varphi)$, which are called caustics. The magnification diverges when the source star crosses a caustic. While there is only one point at which the magnification diverges to infinity in the case of single lens ($u = 0$), it becomes curve(s) in the case of binary lens.

Equation (2.28) can be solved analytically when $\mu_1 = \mu_2 = 0.5$, or $q \equiv \mu_2/\mu_1 = 1$ as

$$z(\varphi) = \pm\sqrt{\frac{e^{i\varphi}}{2} + \frac{s^2}{4} \pm \frac{e^{i\varphi}}{2}\sqrt{1 + 2e^{-i\varphi}s^2}}, \tag{2.29}$$

where $s \equiv |z_{L1} - z_{L2}|$ is the projected separation between two lenses, normalized by $R_E$. Hereafter, the mass ratio is referred to as $q$, and the separation as $s$, instead of $\mu_1$ and $\mu_2$, and $z_{L1}$ and $z_{L2}$, respectively. The shapes and locations of caustics and critical curves are then determined by $q$ and $s$. There are two $\pm$ signs in

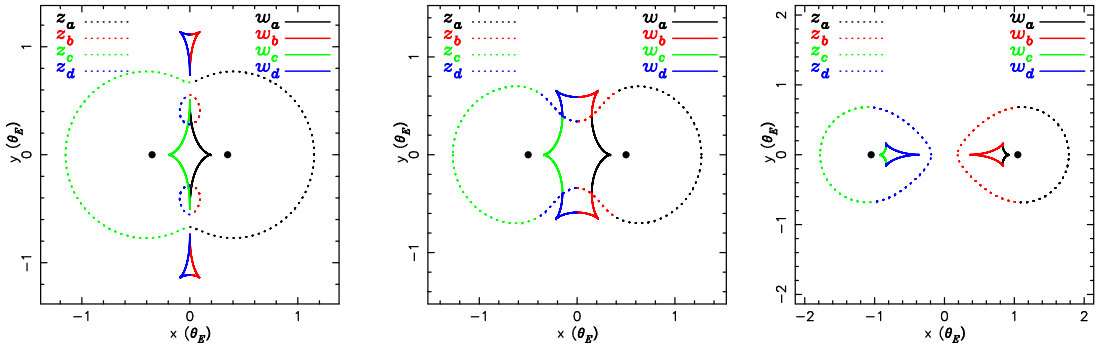


Figure 2.6: Critical curves (dotted lines) and caustics (solid lines) with $q = 1$. (Left) $s = 0.7$, (Middle) $s = 1$ and (Right) $s = 2.1$. The color codings represent each of one of the four solutions, $z_a(\varphi), \ldots, z_d(\varphi)$ or $w_a(\varphi), \ldots, w_d(\varphi)$. The two black dots indicate the positions of the two lenses.

the formula, and the four combinations of them correspond to the four curves of $z_a(\varphi), \ldots, z_d(\varphi)$. Figure 2.6 shows the four curves of $z_a(\varphi), z_b(\varphi), z_c(\varphi)$ and $z_d(\varphi)$ which are the $++$, $+-$, $-+$ and $--$ solutions of Equation (2.29) shown in dashed curves, respectively, and the corresponding four curves of $w_a(\varphi), w_b(\varphi), w_c(\varphi)$ and $w_d(\varphi)$, shown in solid curves. These four curves are linked with each other and produce one, two or three closed curves depending on the $s$ value. When the separation, $s$, is moderately smaller or larger than 1, the number of closed curves is 3 or 2, respectively. All curves link together when the separation $s$ is close to 1. This behavior of the number of critical curves and caustics is qualitatively true for any mass ratio value of $q$, although the border value of $s$ - which changes the number of closed curves - depends on the value of $q$.

When $q \neq 1$, Equation (2.28) can be solved numerically. While the positions of the caustics are symmetrical with respect to the $y$ axis ($x = 0$) when $q = 1$, as shown in Figure 2.6, the positions of the caustics become more asymmetrical as $q$ gets smaller. This is particularly true when the lens system has a planetary mass ratio ($q = \mu_2/\mu_1 \lesssim 0.03$); one of the caustics always appears near to the primary star, and is referred to as the central caustic. Figures 2.7-2.9 show the caustics and critical curves for $q = 0.01$ with $s = 0.8$, $s = 1.0$ and $s = 1.35$, respectively, and the light curves corresponding to the source trajectory are shown as blue arrowed line in the (a) sub-plots. In Figure 2.7 (a) with $s = 0.8$ and Figure 2.9 (a) with $s = 1.35$, two and one caustics - other than the central caustic - appear on the opposite, and same side of, the secondary lens with respect to the $y$ axis, respectively, which are called planetary caustics. When the separation, $s$, is close to 1, planetary caustics are located near to the central caustic, and they merge to a single curve when $s \sim 1$ (Figure 2.8). The united caustic is called resonant caustic.

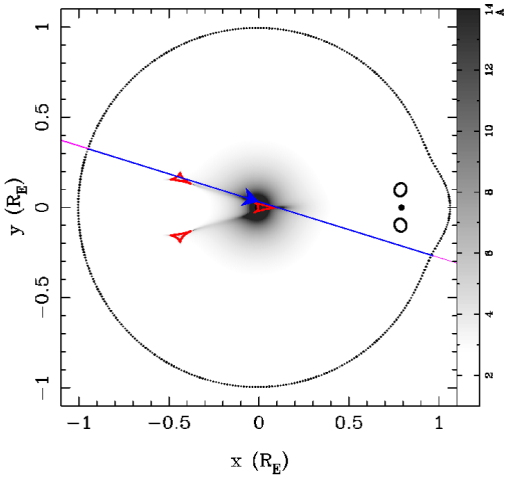


(a)

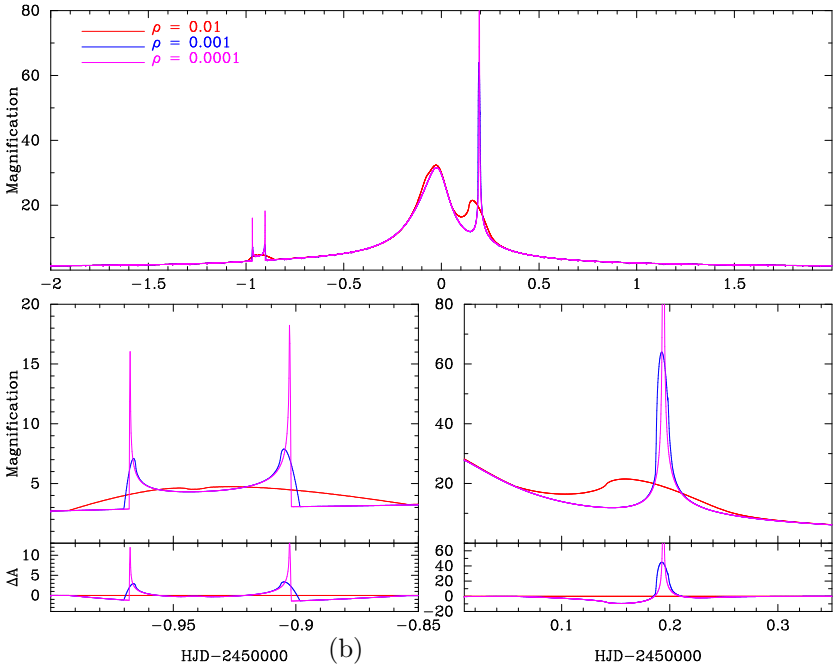


(b)

Figure 2.7: (a) Critical curves and caustics with $q = 0.01, s = 0.8$. The black and red closed curves are critical curves and caustics, respectively. The black dot indicates a secondary lens object. The magnification map is represented in gray scale, and the blue arrowed line runs along the source trajectory. (b) The light curve corresponding to the source trajectory, (a). Red, blue and magenta lines indicate the light curves with a finite source effect parameter, $\rho \equiv \theta_*/\theta_E$, as shown in upper left, respectively. The anomaly highlighted in the bottom left panel occurs when the source crosses the planetary caustic, and the first and second sharp peaks locate its entry and exit, except the case of $\rho = 0.01$. The anomaly highlighted in the bottom right panel occurs when the source brushes the cusp of the central caustic. The bottom insets show the light curve residuals relative to $\rho = 0.01$.

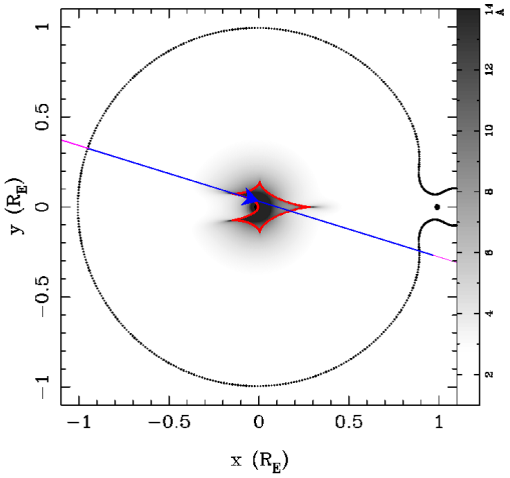


(a)

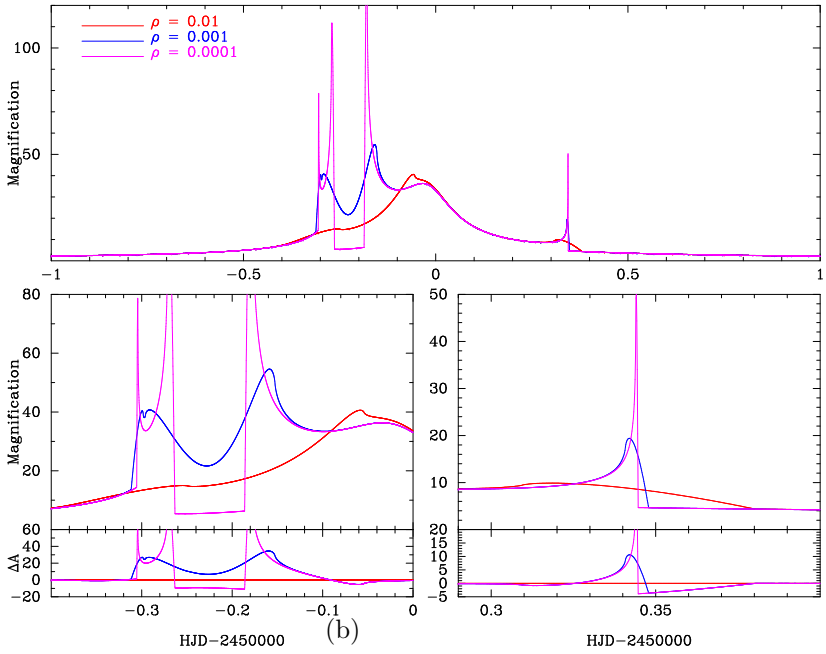


(b)

Figure 2.8: Same as Figure 2.7, but with $q = 0.01, s = 1.0$. In this case, the source experiences entry/exit of the caustic twice, and therefore the light curve has up to 4 peaks.

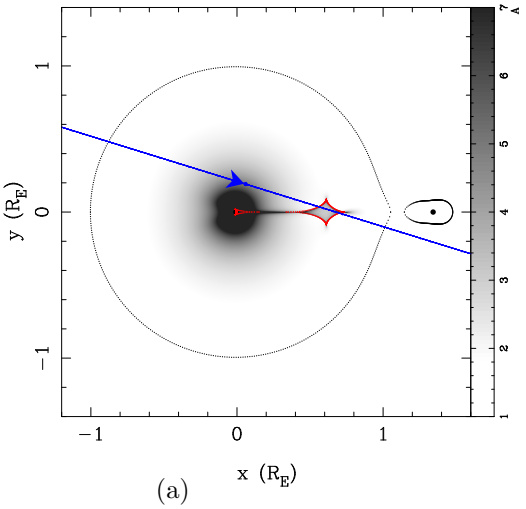


(a)

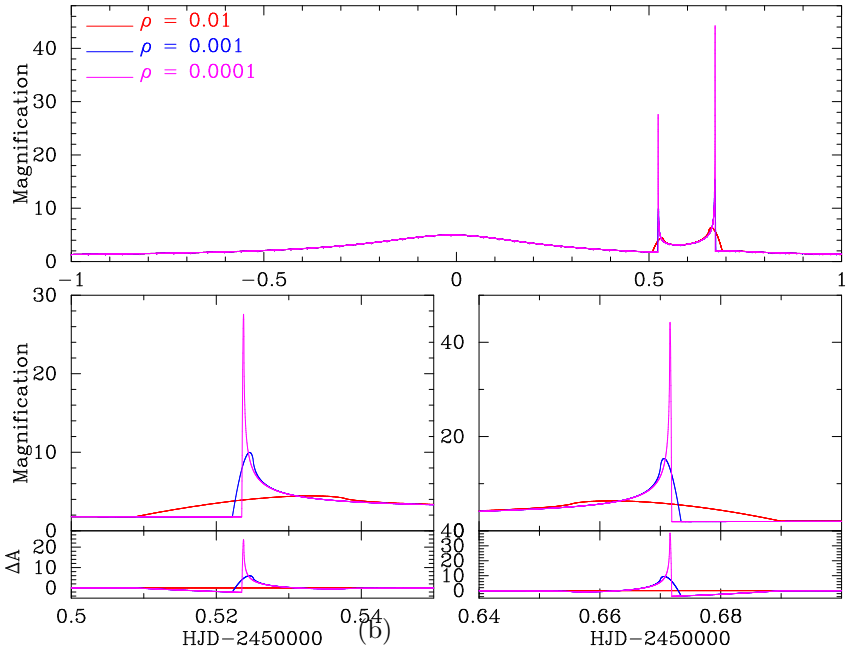


(b)

Figure 2.9: Same as Figure 2.7, but with $q = 0.01, s = 1.35$. The source experiences entry/exit of the caustic only once, and therefore the light curve has 2 peaks.

In the light curves in Figures 2.7-2.9, the difference between binary lenses and single lenses is clearest only when the source passes around the caustics, and no difference can be observed at the other parts. We call this deviation an "anomaly", and observing an anomaly is only way to detect a planet via microlensing light curves. In other words, we cannot know the existence of planet around the primary lens star, even when the planet exists there, if we miss the anomaly, or the source does not pass around any caustic.

#### Observables of Binary Lens Event

To fit a binary lens event, some parameters are added to those of the single lens event. The three new parameters are the secondary-primary mass ratio of $q$, the projected separation between two lens objects normalized by $R_E$ of $s$ that determines the shapes and locations of caustics, and the angle of a source trajectory of $\alpha$. Binary lens events are more sensitive to high order effects, such as the finite source effect or the microlensing parallax effect that are described in next section, than single lens events. The finite source effects can be especially well-detected in most planetary events. Hence, the standard binary lens model generally includes the finite source parameter of $\rho$.

## 2.2 High Order Effects

As already described, the distance to the lens object $D_L$, the lens mass $M_L$ and the relative proper motion $\mu_{rel}$ degenerate into a single parameter, Einstein timescale $t_E$, and cannot be determined uniquely. However, the degeneracy can be broken down by detection of high order effects. Here we explain two main high-order effects: the finite source effect, and the parallax effect.

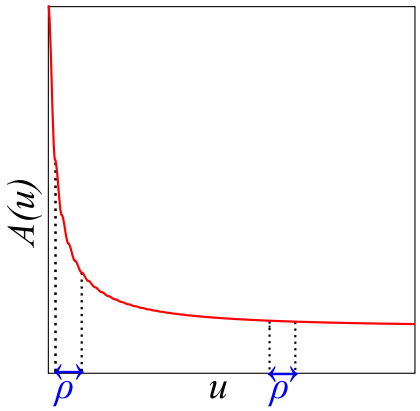


Figure 2.10: Magnification by a single lens for $u$ and a source size of $\rho$. When $u$ is relatively large, the magnification is almost flat in a $\rho$, but it can dramatically vary in the same $\rho$ when $u$ is small.

### 2.2.1 Finite Source Effect

We have assumed a point source so far. However, the finite size of the source cannot be neglected when the spatial variation of the magnification in the source plane is large within the source surface, $S_\rho$. The finite source can be introduced in the light

curve model by adding a parameter,

$$\rho = \frac{r_*/D_S}{R_E/D_L} \tag{2.30}$$

$$= \frac{\theta_*}{\theta_E} \tag{2.31}$$

where $r_*$ and $\theta_*$ are the radius and the angular radius of the source star, respectively. In the case of a single lens for example, the magnification is given by Equation (2.15). As shown in Figure 2.10, when the variation of the magnification is small in $S_\rho$, the values at each $d^2u$ are almost equal, and it does not matter that we consider the source as a point. Contrary to this, when the variation is large, we cannot neglect the source size of $\rho$. In this case, the surface brightness density of the source, $S(\boldsymbol{u})$, also varies at each $d^2u$ because of limb darkening. Hence, the magnification at $\boldsymbol{u}$ can be evaluated by integrating the point source magnification $A(\boldsymbol{u})$ and the surface brightness $S(\boldsymbol{u})d^2u$ over the source surface $S_\rho$ as follows,

$$A_f(\boldsymbol{u}) = \frac{\displaystyle\int_{S_\rho} A(\boldsymbol{u'})S(\boldsymbol{u'})d^2u'}{\displaystyle\int_{S_\rho} S(\boldsymbol{u'})d^2u'} \tag{2.32}$$

where $\boldsymbol{u}$ is the center of the source, $S_\rho$ is assumed to be a circle, and $\int_{S_\rho} S(\boldsymbol{u'})d^2u' = F_S$.

It has previously been described that the magnification diverges to infinity on the caustics in Section 2.1.3, but the observed light curve does not diverge because of the finite source effect. Figure 2.7 and Figure 2.8 show the light curves with $\rho$ = 0.0001, 0.001 and 0.01. From the figures, we find that the peaks of the anomaly become duller as $\rho$ increases.

If the finite source effect is seen in the observed light curve, we can obtain a new observable, $\rho$, from which the angular Einstein radius, $\theta_E$, and lens-source relative proper motion, $\mu_{rel}$, can be derived by using Equation (2.31) as follows,

$$\theta_E = \frac{\theta_*}{\rho} \tag{2.33}$$

$$\mu_{rel} = \frac{\theta_E}{t_E} = \frac{\theta_*}{t_E\,\rho}. \tag{2.34}$$

Here the source angular radius, $\theta_*$, can be obtained by using the source color and magnitude, as described in Section 2.3. Moreover, from Equation (2.8), we can find the relationship between the mass, $M_L$, and the distance, $D_L$ (mass–distance

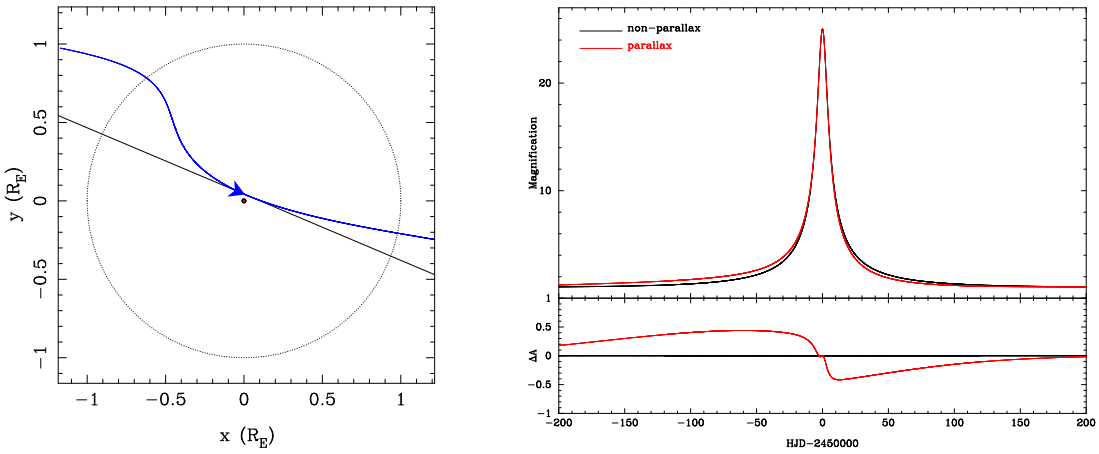


(a) (b)

Figure 2.11: (a) A source trajectory affected by the parallax effect and (b) the corresponding light curve. In (b), the light curve with and without the parallax effect are shown in red and black lines, respectively. The residual from the non-parallax model is shown in the bottom inset. The light curve becomes asymmetric with this effect.

relation),

$$M_L = \frac{c^2}{4G}\theta_E^2 \frac{D_S\,\nu}{1-\nu}. \tag{2.35}$$

If we have any constrains on $D_L$, we could estimate $M_L$ from this formula.

While single lenses create only one caustic, i.e., the point at the center of the lens, a binary lens creates up to three caustics which are wide-spread on the source plane, and, therefore, binary lens events are more sensitive to the finite source effect than single lens events.

### 2.2.2 Parallax Effect

#### Annual parallax

In the above sections, we assumed that the relative motion of the source, lens and observers were linear. However, the observers on the Earth orbit around the Sun. When the event timescale $t_E$ is relatively long, typically $t_E > 50$ days, and/or the lens object is relatively close, the light curve can be affected by the non-linear motion of the line of sight due to the Earth's orbital motion, which called the microlens parallax, or annual/orbital parallax to distinguish from the space parallax described in next section. Then, we can measure new physical quantities, $\pi_{E,N}, \pi_{E,E}$, which are the north and east component of the relative parallax vector between the source and the lens, $\boldsymbol{\pi_E}$, respectively. A more detailed introduction

to the annual parallax effect is presented in Appendix A. Figure 2.11 shows an example of a light curve and the source trajectory with the annual parallax effect.

The magnitude of $\boldsymbol{\pi_E}$ is represented by the ratio between the lens-source relative parallax, $\pi_{rel}$, and the angular Einstein radius $\theta_E$,

$$\pi_E = \frac{\pi_{rel}}{\theta_E} = \frac{(D_S - D_L) \times 1\mathrm{AU}/D_S D_L}{R_E/D_L} = \frac{1\mathrm{AU}}{\tilde{r}_E} \tag{2.36}$$

where

$$\tilde{r}_E = \frac{R_E D_S}{D_S - D_L} = \frac{R_E}{1-\nu} \tag{2.37}$$

is the projected Einstein ring radius from the source star to the observer plane.

By squaring both sides of Equation (2.37), one can derive the relationship between the lens' mass, $M_L$, and the distance, $D_L$,

$$M_L = \frac{c^2}{4G}\left(\frac{1\mathrm{AU}}{\pi_E}\right)^2 \frac{1-\nu}{D_S\,\nu} \tag{2.38}$$

which is similar, but independent to, the relation from the finite source effect. Hence, by obtaining the microlens parallax, $\pi_E = \sqrt{\pi_{E,N}^2 + \pi_{E,E}^2}$, the finite source effect, $\rho$, and the source angular radius, $\theta_*$, the degeneracies of the lens properties in $t_E$ can be broken entirely, i.e., one can exactly calculate the mass from Equation (2.35) and Equation (2.38) as

$$M_L = \frac{c^2(1\mathrm{AU})}{4G}\frac{\theta_E}{\pi_E} \tag{2.39}$$

$$= \frac{\theta_E}{\kappa \pi_E} \qquad (\kappa = 8.144\,\mathrm{mas}\,M_\odot^{-1}), \tag{2.40}$$

then the distance, $D_L$, as

$$D_L = \frac{1\mathrm{AU}}{\pi_E \theta_E - \frac{1AU}{D_S}} \qquad (D_S \sim 8\,\mathrm{kpc}) \tag{2.41}$$

where the source star is assumed to be located in the Galactic Bulge. The relative proper motion, $\mu_{rel}$, can be given by Equation (2.34).

In the case of a binary lens event, the probability of detecting both the finite source effect and the parallax effect is much higher, compared to that of a single lens event. We can calculate the primary and secondary masses of $M_{L1}$ and $M_{L2}$ using the mass ratio $q$. Also, the projected separation of the lens system to the lens plane is derived as

$$r_\perp = D_L\,\theta_E\,s. \tag{2.42}$$

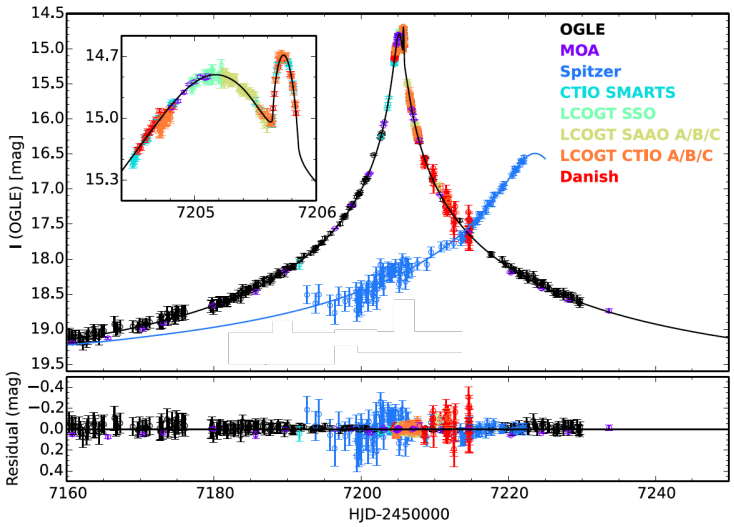


Figure 2.12: The light curve of OGLE-2015-BLG-0966 as an example of space parallax. The top panel shows the light curve, and the bottom panel shows the residual from the best-fit planetary model. The top left inset highlights the anomaly at the peak. The blue dots and line indicate the data and model seen from *Spitzer*, respectively. The figure is modified from Street et al. (2016).

Therefore, in the case that the lens is a planetary system, we can obtain the planetary mass, $M_{\rm P}$, and projected separation, $r_\perp$. Assuming the inclination of the planetary orbit and the phase of the planet is totally random, the probability distribution of the projected separation $r_\perp$ given by a planet with the actual separation $a$ is

$$p(r_\perp) = \frac{r_\perp}{a^2}\left(1 - \frac{r_\perp^2}{a^2}\right)^{-1/2} \tag{2.43}$$

and its median value is $\sqrt{3}/2\, a \simeq 0.87\, a$ (Gould & Loeb 1992). From this formula, we can calculate the probability distribution of the actual separation $a$ from the derived $r_\perp$.

### Space parallax and terrestrial parallax

In addition to the parallax effect due to the Earth's motion described above, we can obtain the same physical quantity $\boldsymbol{\pi_E}$ by conducting simultaneous observations from the Earth and space. This is because the geometry of a microlensing event depends on the direction of the line of sight, which indicates that an event can be observed with a different peak time and a different magnification at the

peak depending on the location of the observatory. When the separation between the Earth and the satellite is projected toward a target $D_\perp$ is comparable to $\tilde{r}_E$ (typically $\sim$ AU), the impact parameter $u_{0,\oplus}$ and the corresponding time $t_{0,\oplus}$ from the Earth diverge from those parameters measured from the separated satellite $u_{0,\rm sat}$ and $t_{0,\rm sat}$. The microlens parallax vector is then given by

$$\boldsymbol{\pi_E} = \frac{\rm AU}{D_\perp}\left(\frac{\Delta t_0}{t_E}, \Delta u_0\right), \tag{2.44}$$

where $\Delta t_0 = t_{0,\rm sat} - t_{0,\oplus}$ and $\Delta u_0 = u_{0,\rm sat} - u_{0,\oplus}$. Note that the observed $t_E$ can also be different because of the difference between the transverse velocities of the Earth and the satellite, but usually the difference is negligible compared with the uncertainty. Over one hundred events - including single and binary lens events - have been simultaneously observed by ground-based telescopes and the *Spitzer* telescope (Yee et al. 2015, Zhu et al. 2017b). Figure 2.12 shows an example of a light curve simultaneously observed from the Earth and the *Spitzer* satellite, OGLE$-$ 2015$-$ BLG$-$ 0966 (Street et al. 2016).

For an extremely high-magnification event, typically $A_{\rm max} \gtrsim 1000$, the peak of the event becomes extremely sharp, and thus we can measure the $u_0$ and $t_0$ very precisely if we can densely observe the peak of the light curve . In such an event, the differences between $\Delta t_0$ and $\Delta u_0$ can be observed even among observatories at different places on the Earth, and thus, the microlens parallax vector $\boldsymbol{\pi_E}$ is also measurable, which is called the terrestrial parallax effect. This effect has only been observed in two events so far, OGLE-2007-BLG-224 (Gould et al. 2009) with $A_{\rm max} \simeq 2500$ and OGLE-2008-BLG-279 (Yee et al. 2009) with $A_{\rm max} \simeq 1600$.

## 2.3 Observable Fluxes

In the above sections, the observable parameters from the variation of magnification have been described. In practice, what we observe is the flux from the target,

$$F(t) = A(\boldsymbol{x}, t)F_S + F_b, \tag{2.45}$$

where $A(\boldsymbol{x}, t)$ is the model of magnification variation as a function of time, and $F_S$ and $F_b$ are the unmagnified source flux and the blending flux, respectively. Therefore, $F_S$ and $F_b$ are also the fitting parameters - in addition to $\boldsymbol{x} = (t_0, t_E, u_0)$ for a single lens event, or $\boldsymbol{x} = (t_0, t_E, u_0, q, s, \alpha)$ for a binary lens event. $F_S$ and $F_b$ can be easily determined by a linear fit to the observed flux $F(t)$, once a model of magnification variation $A(\boldsymbol{x}, t)$ is given.

If the light curve data of an event is obtained in multi-bands, the source color information, in addition to its magnitude, can be found by the linear fitting of each

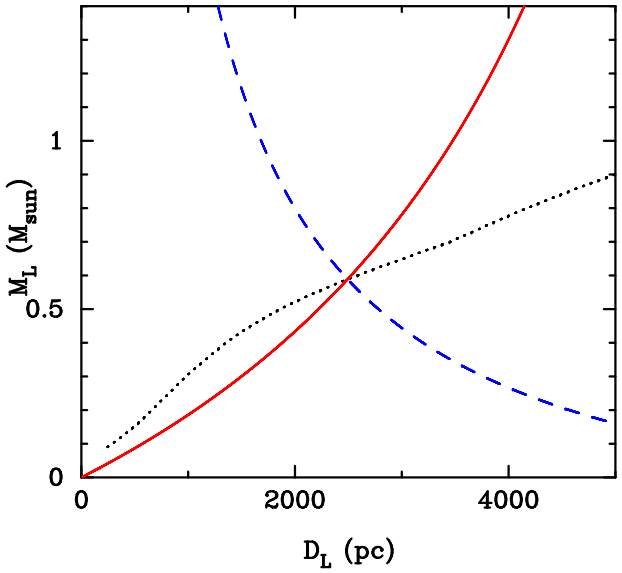


Figure 2.13: Three mass–distance relations. The red solid, blue dashed, and black dotted lines are from $\theta_E$, $\pi_E$ and $F_L$, corresponding to Equations (2.35), (2.38) and (2.46), respectively. Here, the angular Einstein radius, microlens parallax, and the magnitude of the lens flux in the $H$-band are assumed to be $\theta_E = 1.15$ mas, $\pi_E = 0.24$, and $H_L = 17.51$ mag, respectively. The source distance is fixed at $D_S = 8$ kpc.

of the light curves in different bands. This is because the magnification $A(\boldsymbol{x}, t)$ does not depend on the wavelength. Having magnitude and color information about the source star roughly indicates its spectral type and the distance to the source star, which are related to the angular radius of the source star, $\theta_*$. In practice, an empirical relation between the angular radius of a star and its color and magnitude is used to estimate $\theta_*$ (Kervella et al. 2004, Boyajian et al. 2014). Although our interest is usually in the lens system, this information is important to obtain the angular Einstein radius, $\theta_E$, as described in the next section. Therefore, it is desirable to observe an event through a multi-band filter.

It should be noted that the blending flux, $F_b$, can be informative about the lens property, because it includes the flux from the lens. If we can determine the lens flux, $F_L$, it also provides a mass–distance relation of the lens, in addition to the other two relations of Equations (2.35) from $\theta_E$ and (2.38) from $\pi_E$. This is because the mass-luminosity relation $\mathcal{L}_\lambda(M)$ of a star for various pass bands of $\lambda$ is well studied, both theoretically and observationally (Bressan et al. 2012, Delfosse et al. 2000). Thus, the measured lens flux - corrected for extinction - gives

a mass–distance relation,

$$F_{L,\lambda} = \frac{\mathcal{L}_\lambda(M_L)}{4\pi D_L^2} \tag{2.46}$$

when the $M_L$ is dominated by a primary star. The three mass–distance relations of Equations (2.35), (2.38) and (2.46) are plotted in Figure 2.13. In $\sim 70\%$ of planetary events so far, the parallax measurement is not known, and thus the lens mass cannot be determined solely from the light curve. Therefore, the measurement of $F_L$ is very important to calculate a mass measurement for such events, and also to confirm the parallax and the finite source measurement for other events. However, with limited seeing observations toward the Galactic bulge, the blending flux $F_b$ is usually dominated by the brightness from unrelated ambient stars, and the lens flux $F_L$ cannot be resolved. This is because typically more than two bright bulge main sequence stars exists per seeing disk with the full width at half maximum (FWHM) of $\sim$1 arcsec. Therefore, we usually use $F_b$ just as an upper limit of the lens flux (Koshimoto et al. 2014). But, with high angular resolution imaging by a large, ground-based telescope with adoptive optics (AO), or the Hubble Space Telescope (*HST*), the contribution from ambient stars can be dramatically reduced, and the blending flux can be used as a strong constraint on the lens property (Batista et al. 2014, 2015, Bennett et al. 2015, Fukui et al. 2015, Koshimoto et al. 2017a,b). The blending flux from AO or *HST* observations is referred to as the "excess flux" throughout this thesis, and this is a key word of the work in Chapters 3 and 4.

## 2.4 Practical Application

The two main requirements for exoplanet search via microlensing are "large field of view (FOV)" and "high cadence" observations. This is because, firstly, microlensing is an extremely rare phenomenon, one event per $10^6$ stars, even toward a dense field of the Galactic bulge, and secondly, because the anomaly due to a planet is very short - typically a few days for a Jupiter-mass planet, and a few hours for an Earth-mass planet.

### 2.4.1 First Generation: Survey and Follow-Up

To overcome the two requirements, Gould & Loeb (1992) proposed a strategy two decades ago - even before the first detection of an exoplanet - consisting of two stages. In the first stage, telescopes with a wide FOV camera monitor millions of stars, reduce the images, and check the light curves in real time, to find new microlensing events as soon as possible. Note that the original paper

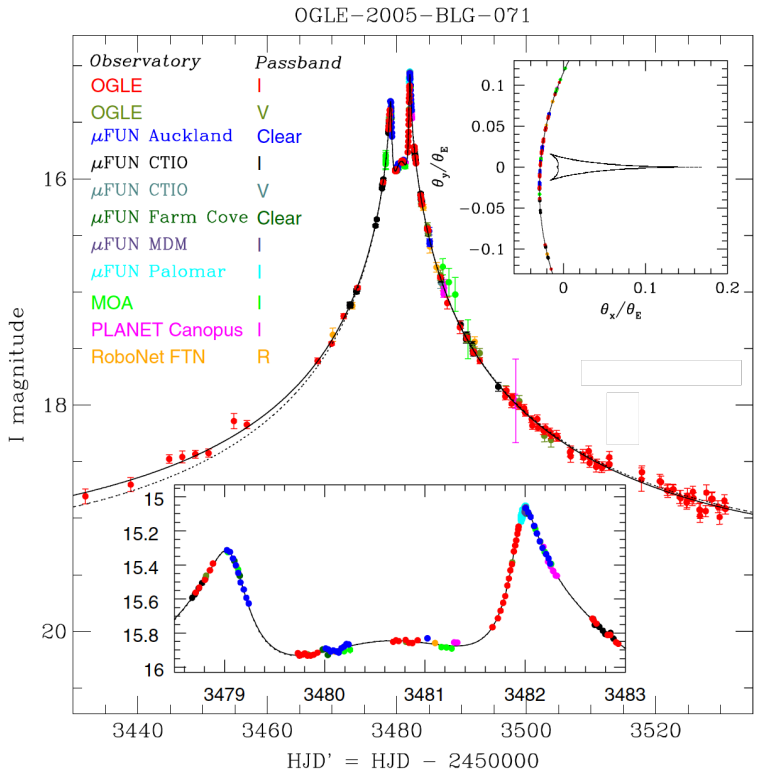


Figure 2.14: Light curve of a high-magnification planetary event OGLE-2005-BLG-071. The top right inset shows the source trajectory, which passed near the central caustic. This figure is modified from Dong et al. (2009a).

assumed $\sim 0.5\,\mathrm{deg}^2$ FOVs, which covers the entire bulge twice per night, as the survey observation. In the second stage, follow-up groups, which have many small telescopes in different time zones, pick good candidates from the catalogue of events based on their criteria, and conduct intensive observations toward the selected targets to catch the short planetary signal.

This strategy worked well and led the early stage of exoplanet search via microlensing, especially for high-magnification events (Gould et al. 2006, Gaudi et al. 2008, Dong et al. 2009b, Gould et al. 2010). As described in Section 2.1.3, the central caustic always appears near the primary lens for planetary events. Thus, a high-magnification event ($u_0 \lesssim 0.01$) has a very high sensitivity to a planet if the peak of the event is densely covered. Figure 2.14 shows the light curve of a high-magnification planetary event OGLE-2005-BLG-071. Two follow-up groups of the Microlensing Follow Up Network ($\mu$FUN) and RoboNet started their follow-up observations before the peak where the anomaly occurred, because this event was predicted to become a high-magnification event by real-time fitting using the data of survey groups. This mode of search is classified as the first-generation microlensing search (Gaudi et al. 2009, Gaudi 2012).

### 2.4.2 Second Generation: Survey with Large FOV Camera

Currently, a large fraction of planetary microlensing events have been discovered and characterized by survey data alone (Yee et al. 2012, Shvartzvald et al. 2014, Koshimoto et al. 2014, 2017a, Bond et al. 2017) as technology has developed, and thus the number of telescopes equipped with very large FOV ($> 1$ deg$^2$ ) cameras for the microlensing survey has increased, which corresponds to the second-generation survey mode.

The Microlensing Observations in Astrophysics (MOA; Bond et al. 2001, Sumi et al. 2003) group first started a microlensing survey with very wide FOV cameras in 2005. They use the $2.2\,\mathrm{deg}^2$ FOV MOA-cam3 (Sako et al. 2008) CCD camera mounted on the 1.8 m MOA-II telescope at the Mt. John University Observatory in New Zealand. Figure 2.15 shows their survey field toward the Galactic bulge. The large FOV camera is capable of observing the entire $\sim$50 deg$^2$ sky area with a 30-min cadence, on average. They alert the community about 600 microlensing events per year.

The Optical Gravitational Lensing Experiment group (OGLE; Udalski 2003) has been conducting a microlensing survey with the 0.34 deg$^2$ FOV OGLE-III during 2001-2009, and upgraded their camera to the 1.4 deg$^2$ FOV OGLE-IV camera in 2010 (Udalski et al. 2015a). They now discover more than 2000 microlensing events per year, with the camera mounted on the 1.3 m Warsaw telescope at the Las Campanas Observatory, Chile.

In 2015, the Korean Microlensing Telescope Network (KMTNet; Kim et al.

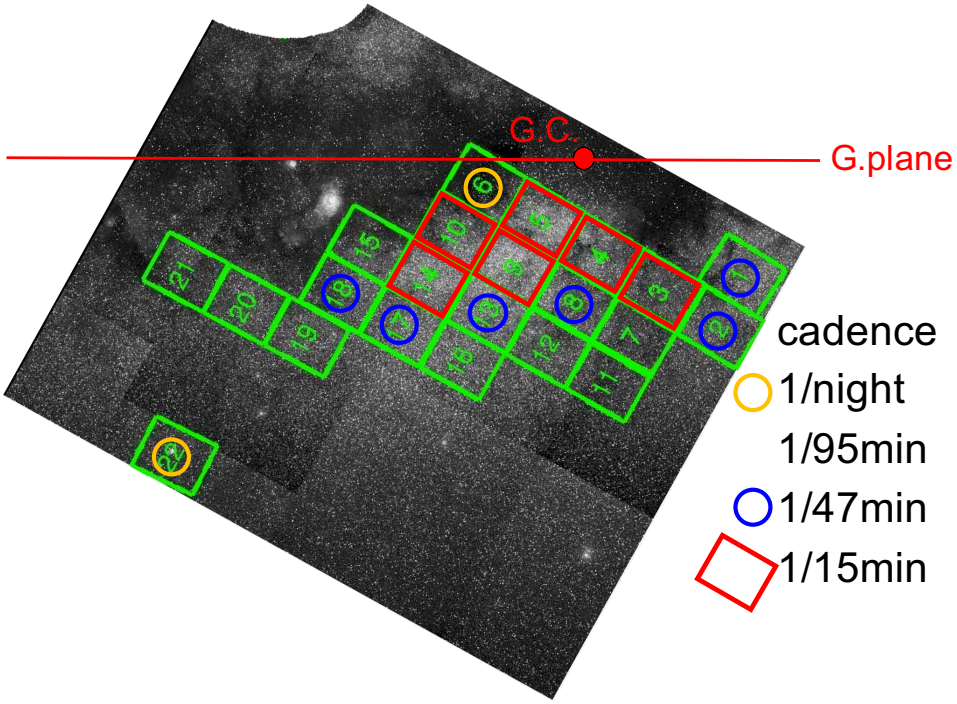


Figure 2.15: MOA-II observation fields toward the Galactic bulge. A mark in each field corresponds to the cadence of the field shown on the bottom right, which is determined based on the event rate of each field.

2016) also started their survey observations. The KMTNet has three 1.6 m telescopes at the Cerro Tololo Interamerican Observatory (CTIO) in Chile, the South African Astronomical Observatory (SAAO) in South Africa, and the Siding Spring Observatory (SSO) in Australia, each of which has a 4 $deg^2$ FOV camera mounted. Their survey, by globally distributed three telescopes with 4 $deg^2$ FOV cameras, is solely capable of round-the-clock monitoring of microlensing events with a 10-min cadence through a few months in the mid-bulge season, as long as the weather is clear.

Now, the equipment requirements for second-generation microlensing surveys are Fulfilled, and the number of planet detections is predicted to increase over the next few years.

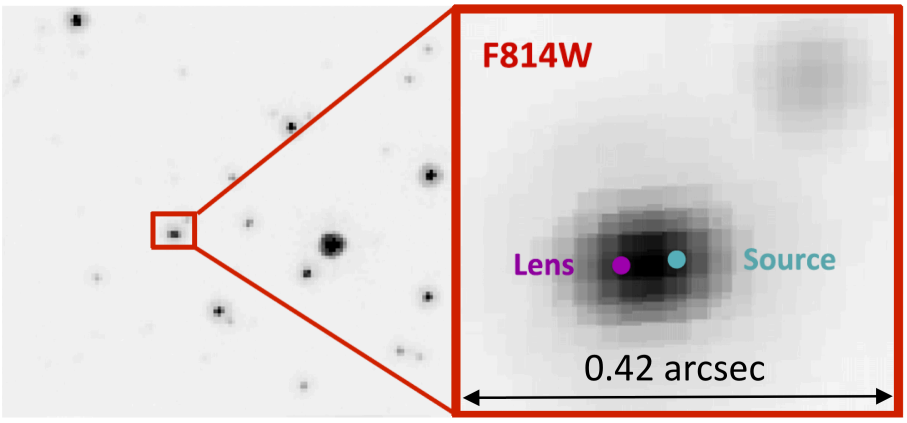


Figure 2.16: *HST* image of OGLE-2005-BLG-169, which is taken 6.5 years after the discovery of the event. The lens and the source are so separated that the target is elongated. The figure is modified from Bennett et al. (2015).

### 2.4.3 High Resolution Follow-Up Observation

Another kind of follow-up observation has been conducted for planetary microlensing events, not to cover the planetary signal in the light curves, but to determine the lens flux $F_L$. As described in Section 2.3, this kind of observation requires high angular-resolution imaging, typically with the FWHM of $< 0.2$ arcsec to reduce the contamination probability, which is only achievable by using AO observation or observation from space. The lens-source relative proper motion is typically $\mu_{rel} =$ 1 - 10 mas yr$^{-1}$. Thus, the information obtained from the high angular-resolution imaging is different depending on the time when the observation is conducted.

If we observe a planetary event when the angular separation between the lens and the source is typically larger than $\sim 20$ mas (this value depends on fluxes of the source and the lens), we can see that the target is elongated, in addition to the brightness information. Bennett et al. (2015) and Batista et al. (2015) observed a planetary event OGLE-2005-BLG-109 with $\mu_{rel} \sim 7.4$ mas yr$^{-1}$ 6.5 years and 8.2 years after the discovery of the event by *HST* and Keck, respectively. The target was elongated in the *HST* image (see Figure 2.16) and was separated (i.e., the lens is resolved) in the *Keck* image. They derived the relative proper motion value from each of the elongations, and confirmed the value from the finite source effect in the light curve observations, as well as the lens mass measurement of $M_L = 0.69 \pm 0.02 M_\odot$ (Bennett et al. 2015) and $M_L = 0.65 \pm 0.05 M_\odot$ (Batista et al. 2015) by combining the lens flux $F_L$ from their observation and the angular Einstein radius $\theta_E$ from the finite source effect. In other words, the object, elongated from the source, can be confirmed as the lens (or a lens companion) by comparing the two independent relative proper motion measurements in this case.

On the other hand, if the images are taken without a sufficient interval from the magnification, the target is not elongated, and thus the information included is only about its brightness. As described in Section 2.3, the excess flux $F_{\rm excess}$ is obtained in this case by subtracting the source flux $F_S$ from the target flux. Sometimes there is no excess when the lens is too faint compared to the quadrature sum of the source flux and the target flux uncertainties. In that case, a stronger upper limit can be put on the lens flux than that from the blending flux $F_b$ (Sumi et al. 2010, 2016, Bennett et al. 2014). When there is a significant detection of the excess flux, it - or some part of it − can be used as the lens flux, after a careful consideration of the contamination probability in the excess. A number of previous studies have considered the probabilities that observations of excess flux might be contaminated by excess flux due a star, or stars, other than the lens star (Janczak et al. 2010, Batista et al. 2014, Fukui et al. 2015). The analysis of OGLE-2012-BLG-0950 in Chapter 3 follows their method, but a different approach is used for the analysis of MOA-2016-BLG-227 in Chapter 4. This is because the previous approach has a problem, which is explained in Chapter 5.

### 2.4.4 Third Generation: Survey from Space

An final generation of the microlensing search is a survey from space. It has many decisive advantages compared with ground-based survey, even with a 1-m telescope (Bennett & Rhie 2002);

1. Continuous monitoring is possible without any gap due to weather or daytime;

2. The accuracy of photometry is much better and more stable because there is no sky background and also little blending effect, which results in its potential to detect sub-Earth mass planets;

3. It is easy to detect the lens flux because all images correspond to high-angular resolution imaging;

4. Concurrent observations with ground-based telescope can measure the space parallax.

The Wide-Field InfraRed Survey Telescope (*WFIRST*, Spergel et al. 2015) was selected as the top priority for a large space mission in the 2010 Astronomy and Astrophysics Decadal Survey. The mirror size of its current design is 2.4 m, and the observation will start in 2020s. A total 432 days (72 days $\times$ 6 bulge seasons) of microlense surveying is currently planned, which is expected to detect about 3000 planets including $\sim$ 100 that are Earth-sized. Figure 2.17 shows its simulated

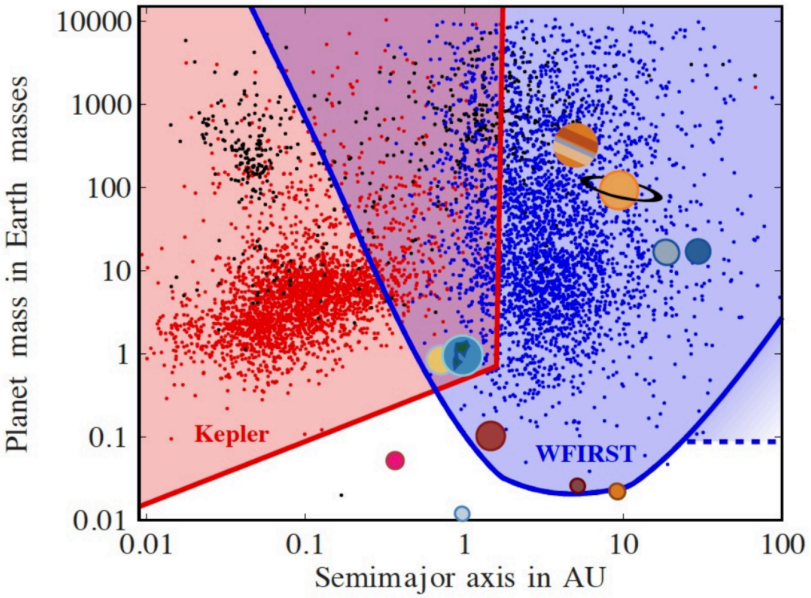


Figure 2.17: Sensitivity of *Kepler* survey (red shaded region) and of *WFIRST* survey (blue shaded region) for exoplanets (Spergel et al. 2013). Objects in the solar system, the Moon, Ganymede and Titan as well as the eight planets, are also shown. The red points are *Kepler* candidates of planets, while the blue points are simulated detections by *WFIRST*.

exoplanet detections (Spergel et al. 2013). *WFIRST* is sensitive to all the solar planets except for Mercury. The covered region is complementary to the region surveyed by *Kepler*, and together they can cover almost all area of the parameter space shown, which will enable the study of the entire population of exoplanets comprehensively.

Three campaigns of continuous observations by space telescopes will have been completed before the *WFIRST* era. The first one is the *Spitzer* microlensing campaign (Yee et al. 2015, Calchi Novati et al. 2015, Zhu et al. 2015, 2017b). This is not a survey observation, but a kind of follow-up observation. Some candidates are selected based on their criteria (Udalski et al. 2015b) from ongoing events, and are observed by *Spitzer* to detect the space parallax. Over 100 events - including some planetary events (Udalski et al. 2015b, Street et al. 2016, Shvartzvald et al. 2017b, Ryu et al. 2017) - have been observed through this campaign, and their microlens parallax has been detected. Recently, Shvartzvald et al. (2017b) measured the lens mass of OGLE-2016-BLG-1195 by combining the finite source effect and the space parallax. They revealed that the lens system consists of a $M_p = 1.43^{+0.45}_{-0.32} M_\oplus$ planet orbiting a $M_h = 0.078^{+0.016}_{-0.012} M_\odot$ ultra-cool dwarf, which is the lowest-mass microlensing planet so far. The second and third campaigns are *K2* Campaign 9 (*K2*C9, Henderson et al. 2016) and *K2* Campaign 11 (*K2*C11). These campaigns

also aim to detect the space parallax using the *Kepler* satellite, but they are especially focused on the first mass determination of a free-floating planet (Sumi et al. 2011, Mróz et al. 2017). However, *Kepler*'s huge pixel scale of 4 arcsecs/pixel makes the photometry of microlensing events challenging, because over 20 bright stars are blended into a pixel on average. Recently Zhu et al. (2017a) provided the first method to extract microlensing light curves from the *K2*C9 data. Zhu et al. (2017c) used the method for the *K2*C9 photometry of a single lens event, MOA-2016-BLG-290, and revealed that the lens has a very low mass of $77^{+34}_{-23} M_J$ and is located at $6.8 \pm 0.4$ kpc, by combining light curves from three separated locations - the Earth, *Spitzer* and *Kepler*. However, the first mass measurement of a free-floating planet has not been reported yet.

# Chapter 3

# OGLE-2012-BLG-0950Lb: First Planet Mass Measurement from Only Microlens Parallax and Lens Flux

We report the discovery of a microlensing planet OGLE-2012-BLG-0950Lb with the planet/host mass ratio of $q \simeq 2 \times 10^{-4}$. A long-term distortion detected in both MOA and OGLE light curve can be explained by the microlens parallax due to the Earth's orbital motion around the Sun. Although the finite source effect is not detected, we obtain the lens flux by the high-resolution Keck AO observation. Combining the microlens parallax and the lens flux reveal the nature of the lens: a planet with mass of $M_{\rm p} = 35^{+17}_{-9} M_\oplus$ is orbiting around an M-dwarf with mass of $M_{\rm host} = 0.56^{+0.12}_{-0.16} M_\odot$ with a planet-host projected separation of $r_\perp = 2.7^{+0.6}_{-0.7}$ AU located at $D_{\rm L} = 3.0^{+0.8}_{-1.1}$ kpc from us. This is the first mass measurement from only microlens parallax and the lens flux without the finite source effect. In the coming space observation-era with *Spitzer*, *K2*, *Euclid*, and *WFIRST*, we expect many such events for which we will not be able to measure any finite source effect. This work demonstrates an ability of mass measurements in such events.

## 3.1 Introduction

Gravitational microlensing is a technique by which planets can be detected without measurements of light from the host star (Mao & Paczynski 1991, Gould & Loeb 1992, Gaudi 2012). Microlensing can detect planets that are difficult to detect by other methods such as planetary systems in the Galactic Bulge (e.g., Batista et al. 2014), planets around late M-dwarfs or brown dwarfs (Bennett et al. 2008,

Sumi et al. 2016), and even free-floating planets not hosted by any stars (Sumi et al. 2011). Compared to other techniques, microlensing is sensitive to Earth mass planets (Bennett & Rhie 1996) orbiting just outside of the snow line where the core accretion theory (Ida & Lin 2004) predicts is the most active planet formation region. Microlensing observations so far have revealed a population of planets beyond the snow line (Gould et al. 2010, Sumi et al. 2010, Cassan et al. 2012, Shvartzvald et al. 2016, Suzuki et al. 2016). Suzuki et al. (2016) finds a steeper slope with $dN/d\log q \sim q^{-0.9}$ and a break (and possible peak) in the mass ratio function at $q \sim 1.0 \times 10^{-4}$. We are capable of studying the distance distribution of planets in our Galaxy via microlensing. Penny et al. (2016) suggests the possibility of a lack of planets in the Galactic bulge. The detection of extra solar planets by gravitational microlensing presents a number of challenges.

Firstly, gravitational microlensing is an extremely rare phenomenon with a probability of one per one million stars and a planetary deviation lasts for only hours or a few days. For these reasons, microlensing observations for exoplanets are conducted toward the Galactic bulge, the most crowded field in our Galaxy. Whereas hundreds of planets are detected by the radial velocity (RV) method (Butler et al. 2006, Bonfils et al. 2013) and thousands of planetary candidates are detected by the *Kepler* telescope (Borucki et al. 2010) to date, the microlensing method has been used to detect about 50 exoplanets so far.

Measuring the mass of a lens $M_{\rm L}$ and distance to the lens system $D_{\rm L}$ is challenging. There are three observables in microlensing which can yield a mass–distance relation of the lens system: the angular Einstein radius $\theta_{\rm E}$, the microlens parallax $\pi_{\rm E}$ and the lens flux. The first one and second one yield each mass–distance relation by combining a relationship between them;

$$M_{\rm L} = \frac{\theta_{\rm E}}{\kappa \pi_{\rm E}} \tag{3.1}$$

with the definitions of $\pi_{\rm E}$, $\pi_{\rm E} \equiv \pi_{\rm rel}/\theta_{\rm E}$, where $\kappa$ is a constant and $\pi_{\rm rel} \equiv {\rm AU}(1/D_{\rm L} - 1/D_{\rm S})$. One can calculate the mass and distance of the lens system if we can measure any two of these quantities. We can measure $\theta_{\rm E}$ in the following manner. Included in most models explaining planetary microlensing light curve data is the source star radius in units of $\theta_{\rm E}$: $\rho \equiv \theta_*/\theta_{\rm E}$. By estimating the angular radius of the source star, $\theta_*$, by an analysis of the source star's color and magnitude, and using our modeled value of $\rho$, we arrive at an estimate of $\theta_{\rm E}$. Microlens parallax can be observed only in relatively rare events and lens flux measurements need follow-up observations with high resolution imaging by an 8-m class telescope. Therefore, only half of planetary events published so far are detected with lens mass measurements and masses of the other half planetary systems are just given their probability distributions by a Bayesian analysis (e.g., Beaulieu et al. 2006; Bennett et al.2014; Koshimoto et al.2014; Skowron et al 2015).

In the microlensing planetary events published so far, there are events with the mass measurements from the angular Einstein radius and microlens parallax (e.g., Bennett et al. 2008; Gaudi et al. 2008; Muraki et al. 2011), from the angular Einstein radius and the lens flux (e.g., Bennett et al. 2006; Batista et al. 2015; Bennett et al. 2015), and from all three relations (e.g., Dong et al. 2009a; Bennett et al. 2010; Beaulieu et al. 2016; Bennett et al. 2016), but events with mass measurement from only microlens parallax and the lens flux have not been published to date. This is simply because the angular Einstein radius is observed much commonly than microlens parallax as mentioned above. However, it has been possible to measure precise microlens parallax by observing simultaneously from space and ground thanks to the *Spitzer* microlensing campaign (Calchi Novati et al. 2015, Udalski et al. 2015b, Yee et al. 2015, Zhu et al. 2015). Also, *K2* campaign 9 (*K2*C9), started in April 2016, has surveyed the Galactic bulge for three months to date. By combining *K2*C9 data and ground-based survey data, it is expected to measure microlens parallax for more than 120 events (Henderson et al. 2016). These next generation space- and ground-based simultaneous observations for microlensing can measure microlens parallax almost regardless of the event timescale. Microlens parallax should become a more common observable rather than the angular Einstein radius in coming next generation, thus, the mass measurement without the angular Einstein radius should be important (Yee 2015).

This paper reports an analysis of a microlensing planetary event OGLE-2012-BLG-0950, which is the first event where a mass measurement is possible from only the measurements of the microlens parallax and lens flux. The survey observations of this event are described in Section 3.2. Section 3.3 explains our data reduction procedure. Section 3.4 shows our modeling results. We show the constraint on the angular Einstein radius by the source angular radius derived from the color and light curve modeling in Section 3.5. We describe our Keck observations and the constraints on the excess flux in Section 3.6. We also calculate the probability of the contamination to the excess flux in the section. In Section 3.7, we derive the lens properties by combining microlens parallax and the lens flux. Finally, Section 3.8 discusses and concludes the results of this work.

## 3.2 Observations

Microlensing event OGLE-2012-BLG-0950 was discovered and alerted by the OGLE Early Warning System (EWS) on 21 June 2012 (HJD$'$ $\equiv$ HJD - 2450000 $\sim$ 6100) as a new event located at $(R.A., Dec.)_{J2000}$ = (18:08:04.62, -29:43:53.7) or $(l, b) = (1.765^\circ, -4.634^\circ)$. Another survey group, MOA, independently found the event and alerted that as MOA-2012-BLG-527 on 9 August 2012. The observations by OGLE were conducted on the $I$-band and $V$-band and the observations

Table 3.1: Data and parameters for our modeling.

| Dataset | Number of data | $k$ | $e_{\min}$ | $u_\lambda$ |
|---|---|---|---|---|
| OGLE $I$ | 1275 | 1.365 | 0 | 0.5470 |
| OGLE $V$ | 81 | 1.576 | 0 | 0.7086 |
| MOA-Red | 6324 | 0.981 | 0 | 0.5895 |
| B&C $I$ | 382 | 1.017 | 0.00611 | 0.5470 |

by MOA were conducted by the custom MOA-Red filter which is similar to the sum of the standard Cousins $R$- and $I$-band filters. MOA also observed the event in the $I$-band using the B&C telescope, a 61 cm telescope for follow-up observation at the same site. The observed light curve is shown in Figure 3.1.

The anomaly part of this event appeared as a small dip around HJD$' \sim 6149$ mainly in the MOA data. The MOA-II telescope observed the anomaly with the 47-min cadence as the regular survey mode. Because the anomaly was very short, $\sim$1 day, and started after the last OGLE observation, we could not increase the cadence nor issue the anomaly alert in a timely manner. Nevertheless, the normal cadence is enough to reveal the perturbation caused by planet. The OGLE data with a cadence of once per night until the anomaly, are also very important for the characterization of this event. In particular, the OGLE data shows us that the dip had not started by HJD$' \simeq 6147.6$, had commenced by HJD$' \simeq 6148.6$ and had almost ended by HJD$' \simeq 6149.6$.

This event does not cross any caustic curves and, unfortunately, MOA could not obtain data on HJD$' \sim 6148$, which corresponds to the start of the anomaly owing to bad weather. Because of these factors, we have no data on a steep gradient of magnification in this event, thus we cannot detect a significant finite source effect. In addition, we took AO images of the target in the year following the discovery, using the Keck telescope. We describe the details of the Keck observations and the analysis in Section 3.6.

## 3.3 Data reductions

Our data-sets for the modeling below consist of 1275 OGLE $I$-band data points, 81 OGLE $V$-band data points, 6324 MOA-Red data points and 382 B&C $I$-band data points.

The OGLE data were reduced by the OGLE Difference Image Analysis (DIA) photometry pipeline (Udalski 2003). The centroid of the catalogued star near the event, which is used for PSF photometry in the standard OGLE pipeline, is

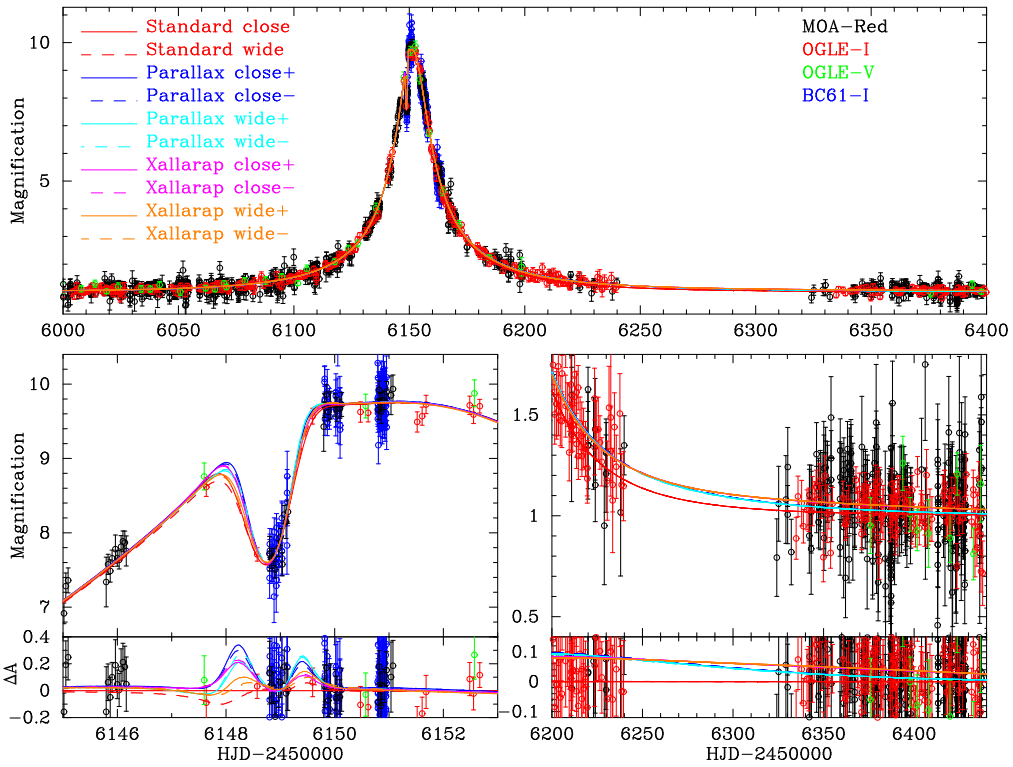


Figure 3.1: Light curve of OGLE-2012-BLG-0950 with the best-fitting models indicated in the top left. The top panel shows the whole event, the bottom left and the bottom right panels highlight the planetary anomaly and the light curve from the end of 2012 to the start of 2013, respectively. The residuals from the Standard close model are shown in the bottom insets of the bottom panels.

significantly different from that of actual event on the difference image. So, we rerun the PSF photometry with the real centroid for the event manually to obtain more accurate photometry.

The images taken by the MOA-II telescope and the B&C telescope were reduced by the MOA DIA pipeline (Bond et al. 2001). In the crowded stellar field images of the Galactic bulge, the precision of photometry is very sensitive to seeing. We found a systematic photometry bias correlated with the seeing value in the MOA-Red data. We reduced this systematic error by modeling it with a polynomial of

seeing and airmass by using the baseline;

$$\begin{aligned} F_{\rm cor} = a_0 &+ a_1\ {\rm JD} + a_2\ {\rm airmass} + a_3\ {\rm airmass}^2 + a_4\ {\rm seeing} + a_5\ {\rm seeing}^2 \\ &+ a_6\ \tan z \cos\phi + a_7\ \tan z \sin\phi + a_8\ {\rm airmass} \tan z \cos\phi\ {\rm seeing} \\ &+ a_9\ {\rm airmass} \tan z \sin\phi\ {\rm seeing} + a_{10}\ {\rm airmass} \tan z \cos\phi\ {\rm seeing}^2 \\ &+ a_{11}\ {\rm airmass} \tan z \sin\phi\ {\rm seeing}^2 \end{aligned} \tag{3.2}$$

where $z$ and $\phi$ are the elevation angle and parallactic angle of the target included to correct the differential refraction, respectively. The $F_{\rm cor}$ is the additional flux for the correction and the corrected flux $F_{\rm new}$ is $F_{\rm new} = F_{\rm cor} + F_{\rm old}$, where $F_{\rm old}$ is the original flux from the DIA pipeline. In the resulting photometry, the $\chi^2$ goodness-of-fit value for the time series of baseline is improved by $\Delta\chi^2 \sim 0.07$ per data point.

The relative error of data points given by the photometry code are robust for a given instrument. However, it is known that the absolutely value of uncertainty are underestimated in such stellar crowded fields for various reasons in general. Thus, we empirically normalize the errors in each data-set to estimate the proper uncertainties of fitted model parameters. We used the formula presented in Yee et al. (2012) for normalization, $\sigma_i' = k\sqrt{\sigma_i^2 + e_{\rm min}^2}$ where $\sigma_i$ is the original error of the $i$th data point in magnitudes, and the parameters for normalization are $k$ and $e_{\rm min}$. $k$ and $e_{\rm min}$ are adjusted so that the cumulative $\chi^2$ distribution as a function of the number of data points sorted by each magnification of the preliminary best-fit model is a straight line of slope 1. By including $e_{\rm min}$, we can correct the error bars at high magnification, which can be affected by flat-fielding errors. But we found unusually large $e_{\rm min}$ values for the OGLE $I$ and MOA-Red data (0.02 and 0.09 respectively) and the deviations from a straight line in cumulative $\chi^2$ distribution mainly arose from baseline data points, i.e., not from high magnification data points as expected. Thus, it is not reasonable to normalize errors with these values and we adopt $e_{\rm min} = 0$ for these two data-sets. This may indicate that there is some low-level systematics in the light curve. We apply $e_{\rm min} = 0,\ k = 1.364$ to OGLE $I$, $e_{\rm min} = 0,\ k = 1.576$ to OGLE $V$, $e_{\rm min} = 0,\ k = 0.907$ to MOA-Red and $e_{\rm min} = 0.0061, k = 1.021$ to B&C $I$. The normalization factors applied for the OGLE $I$ and $V$ data are consistent with those given by Skowron et al. (2016a). Note that the final best fit model parameters are consistent with the preliminary model parameters before the error normalization. Thus, this procedure of the error normalization does not affect our main result. The parameters of these data sets are also shown in Table 3.1.

## 3.4 Modeling

Here we present and compare the light curve modeling with a standard binary lens and adding the effects of parallax. We fit the light curves using a Markov Chain Monte Carlo (MCMC) approach (Verde et al. 2003), with magnification calculations from image centered ray-shooting method (Bennett & Rhie 1996, Bennett 2010).

### 3.4.1 Standard binary lens

In the case of a point lens, the magnification map on the source plane is circular symmetric around the lens. In the point source point lens (PSPL) case, we can characterize the microlensing light curve with the time of the source closest approach to the center of mass of the lens, $t_0$, the minimum impact parameter $u_0$ at $t_0$, and the Einstein radius crossing time (or timescale) $t_{\rm E} = \theta_{\rm E}/\mu_{\rm rel}$, where $u_0$ is in units of $\theta_{\rm E}$ and $\mu_{\rm rel}$ is the lens-source relative proper motion. When the lens has a companion, its gravity distort the magnification map and create the closed curves called as caustics where the magnification is infinite. In this case, three parameters are added to the fitting parameters above; the mass ratio of two lenses $q$ and their angular separation normalized by $\theta_{\rm E}$, $s$, which determine the shape and location of the caustics, and the source trajectory with respect to the binary lens axis, $\alpha$, which determines the direction of a one-dimensional slice of the distorted magnification map. When a source star crosses a region with a steep gradient near the caustics in the magnification map, we can observe the finite source effect. Because source stars of most binary lens events cross such regions, we include the source size $\rho \equiv \theta_*/\theta_{\rm E}$ as a fitting parameter for a binary lens model. With the magnification variation against time, $A(t, \boldsymbol{x})$, which is defined in terms of the above parameters $\boldsymbol{x} = (t_0, u_0, t_{\rm E}, q, s, \alpha, \rho)$, we can linearly fit

$$F(t) = f_S A(t, \boldsymbol{x}) + f_b \tag{3.3}$$

to a data set and obtain the instrumental source flux $f_S$ and the instrumental blending flux $f_b$ for every telescope and pass-band.

We adopt a linear limb-darkening law with one parameter, $u_\lambda$. According to González Hernández & Bonifacio (2009), we estimate the effective temperature, $T_{\rm eff} \sim 5500$ K from the source color which is discussed in Section 3.5 and assumed the solar metallicity. With $T_{\rm eff} = 5500$ K and assuming surface gravity $\log\ g = 4.0$ cm s$^{-2}$ and microturbulence parameter $\xi = 1.0$ km s$^{-1}$, the limb-darkening coefficients selected from Claret (2000) are $u_I = 0.5470$ for OGLE $I$ and B&C $I$, $u_V = 0.7086$ for OGLE $V$, and $u_{\rm MOA-Red} = 0.5895$ for MOA-Red which is the average of standard $I$ and $R$ filters. Therefore, we used the $u_I$ for OGLE $I$ and B&C $I$, the $u_V$ for OGLE $V$ and the mean of the $u_I$ and $u_R$, 0.5895 for MOA-Red,

the filter which has the range of both the standard $I$ and $R$ filters. Although the best estimated value of $T_{\rm eff}$ and the limb-darkening coefficients depend on the source magnitude in each model, we keep using the fixed values. However, this does not affect our final result because the finite source effect is very weak in the light curve, as mentioned below. The limb-darkening coefficients we adopt are also shown in Table 3.1.

We show the parameters of the best-fit models of our standard binary lens modeling in Table 3.2, where the uncertainties shown are from 16th/84th percentile values of stationary distributions given by MCMC. We find a degeneracy between the close model of $s < 1$ and the wide model of $s > 1$ with $\Delta\chi^2 \simeq 0.7$. There is a well-known degeneracy in high magnification microlensing events between lens systems with similar mass ratios, but separations $s$ and $1/s$. In microlensing events suffering this degeneracy, the source star passes close to the central caustic which has, in each of the degenerate solutions, a similar shape. However, in this event, the close/wide degeneracy has a different nature, in terms of the caustic geometry. A single resonant caustic is seen in the wide model with $s = 1.007$ while the caustic curves are separated into central caustic and planetary caustics in the close model with $s = 0.890$. As seen in Figure 3.2, it is understood that the gradients of magnification on the source trajectories are similar in both models although the caustic shapes are different. The mass ratios are $q \simeq 2 \times 10^{-4}$ in both models indicating the companion has a planetary mass. We find that the finite source effect is weak and the $\rho$ value is consistent with $\rho = 0$ at the 1 $\sigma$ level. Because a larger $\rho$ value reduces the dip depth in the light curve and does not explain the data, we can place an upper limit on $\rho$.

Table 3.2: Model parameters.

| Model | $t_0$ (HJD') | $t_{\rm E}$ (days) | $u_0$ | $q$ ($10^{-4}$) | $s$ | $\alpha$ (rad) | $\rho$ ($10^{-3}$) | $\pi_{E,N}/\xi_{E,N}$ | $\pi_{E,E}/\xi_{E,E}$ | $\pi_{\rm E}/\xi_{\rm E}$ | $P_\xi$ ($10^2$ days) | $I_S$ (mag) | $\chi^2$ | $dof$ |
|---|---|---|---|---|---|---|---|---|---|---|---|---|---|---|
| Standard | | | | | | | | | | | | | | |
| close | 6151.58 | 66.4 | 0.104 | 2.3 | 0.890 | 5.098 | 4.3 | - | - | - | - | 19.26 | 8168.8 | 8047 |
| $\sigma$ | 0.03 | 1.5 | 0.003 | $^{+0.6}_{-0.3}$ | 0.008 | $^{+0.009}_{-0.003}$ | $< 7.0$ | - | - | - | - | 0.03 | - | - |
| wide | 6151.59 | 66.7 | 0.104 | 2.3 | 1.007 | 5.100 | 3.4 | - | - | - | - | 19.26 | 8168.1 | 8047 |
| $\sigma$ | 0.03 | 1.6 | 0.003 | $^{+0.6}_{-0.2}$ | 0.008 | $^{+0.008}_{-0.004}$ | $< 6.5$ | - | - | - | - | 0.03 | - | - |
| Parallax | | | | | | | | | | | | | | |
| close+ | 6151.47 | 68.4 | 0.101 | 1.9 | 0.895 | 5.081 | 0.0 | 0.14 | -0.19 | 0.24 | - | 19.29 | 8053.2 | 8045 |
| $\sigma$ | 0.03 | 1.5 | 0.003 | $^{+0.5}_{-0.1}$ | $^{+0.004}_{-0.007}$ | 0.006 | $< 3.2$ | $^{+0.11}_{-0.06}$ | 0.02 | $^{+0.09}_{-0.04}$ | - | 0.03 | - | - |
| close− | 6151.48 | 68.5 | -0.100 | 1.9 | 0.893 | 1.195 | 0.0 | 0.08 | -0.17 | 0.19 | - | 19.30 | 8055.8 | 8045 |
| $\sigma$ | 0.03 | 1.6 | 0.003 | $^{+0.5}_{-0.2}$ | 0.006 | $^{+0.004}_{-0.007}$ | $< 3.0$ | $^{+0.12}_{-0.07}$ | 0.02 | $^{+0.08}_{-0.02}$ | - | 0.03 | - | - |
| wide+ | 6151.49 | 68.7 | 0.101 | 1.9 | 1.004 | 5.083 | 0.0 | 0.17 | -0.20 | 0.26 | - | 19.29 | 8054.7 | 8045 |
| $\sigma$ | 0.03 | 1.4 | 0.003 | $^{+0.6}_{-0.1}$ | $^{+0.008}_{-0.004}$ | 0.006 | $< 3.0$ | 0.08 | 0.02 | 0.06 | - | 0.03 | - | - |
| wide− | 6151.48 | 67.8 | -0.101 | 1.9 | 1.004 | 1.195 | 0.0 | 0.09 | -0.17 | 0.19 | - | 19.29 | 8057.3 | 8045 |
| $\sigma$ | 0.02 | 1.4 | 0.003 | $^{+0.6}_{-0.1}$ | $^{+0.009}_{-0.003}$ | $^{+0.003}_{-0.009}$ | $< 3.1$ | $^{+0.10}_{-0.08}$ | 0.02 | $^{+0.07}_{-0.03}$ | - | 0.03 | - | - |
| Xallarap | | | | | | | | | | | | | | |
| close+ | 6151.50 | 67.2 | 0.103 | 2.0 | 0.894 | 5.085 | 3.5 | 0.0 | -0.6 | 0.6 | 5.3 | 19.27 | 8026.5 | 8042 |
| $\sigma$ | $^{+0.04}_{-0.02}$ | $^{+2.8}_{-1.1}$ | $^{+0.002}_{-0.005}$ | $^{+0.5}_{-0.2}$ | 0.006 | $^{+0.012}_{-0.002}$ | $^{+2.2}_{-0.6}$ | $^{+0.1}_{-0.6}$ | $^{+1.0}_{-0.1}$ | $^{+0.3}_{-0.2}$ | $^{+1.9}_{-0.4}$ | $^{+0.06}_{-0.02}$ | - | - |
| close− | 6151.50 | 66.8 | -0.103 | 2.0 | 0.895 | 1.197 | 3.8 | 0.1 | -0.6 | 0.6 | 5.3 | 19.26 | 8026.4 | 8042 |
| $\sigma$ | $^{+0.04}_{-0.01}$ | $^{+3.6}_{-0.7}$ | $^{+0.006}_{-0.001}$ | $^{+0.5}_{-0.2}$ | 0.006 | $^{+0.003}_{-0.010}$ | $^{+2.0}_{-0.8}$ | $^{+0.1}_{-0.6}$ | $^{+1.0}_{-0.2}$ | $^{+0.4}_{-0.2}$ | $^{+2.4}_{-0.5}$ | $^{+0.07}_{-0.02}$ | - | - |
| wide+ | 6151.50 | 66.7 | 0.104 | 2.1 | 1.005 | 5.088 | 2.9 | -0.5 | -0.3 | 0.6 | 5.2 | 19.26 | 8027.5 | 8042 |
| $\sigma$ | $^{+0.04}_{-0.01}$ | $^{+3.6}_{-0.9}$ | $^{+0.002}_{-0.006}$ | $^{+0.5}_{-0.3}$ | $^{+0.007}_{-0.006}$ | $^{+0.009}_{-0.005}$ | $^{+2.6}_{-0.1}$ | $^{+0.6}_{-0.1}$ | $^{+0.1}_{-0.6}$ | $^{+0.5}_{-0.2}$ | $^{+2.7}_{-0.4}$ | $^{+0.07}_{-0.02}$ | - | - |
| wide− | 6151.50 | 66.4 | -0.104 | 2.3 | 1.006 | 1.194 | 3.6 | 0.0 | -0.6 | 0.6 | 5.3 | 19.26 | 8027.9 | 8042 |
| $\sigma$ | $^{+0.04}_{-0.01}$ | $^{+4.0}_{-0.3}$ | $^{+0.007}_{-0.001}$ | $^{+0.3}_{-0.4}$ | $^{+0.006}_{-0.007}$ | $^{+0.006}_{-0.009}$ | $^{+2.0}_{-0.7}$ | $^{+0.1}_{-0.6}$ | $^{+1.1}_{-0.2}$ | $^{+0.5}_{-0.2}$ | $^{+2.5}_{-0.5}$ | $^{+0.08}_{-0.01}$ | - | - |

**Notes.** A superscript/subscript indicates the difference parameter's 84/16 percentile from the best-fit value, respectively.

### 3.4.2 Parallax

In long timescale microlensing events, such as this one, the effect of Earth's orbital motion around the Sun may be detectable (Gould 1992, Alcock et al. 1995). This effect is expressed by the microlens parallax vector $\boldsymbol{\pi_{\rm E}} = (\pi_{\rm E,N}, \pi_{\rm E,E}) = \pi_{\rm E}\, \boldsymbol{\mu_{\rm rel}}/\mu_{\rm rel}$ (Gould 2000a). Here, $\pi_{\rm E,N}$ and $\pi_{\rm E,E}$ are the north and east components of $\boldsymbol{\pi_{\rm E}}$, respectively, whose direction is same as lens-source relative proper motion. The magnitude $\pi_{\rm E} \equiv 1{\rm AU}/\tilde{r}_{\rm E}$, is defined by 1 AU relative to the Einstein radius projected onto the observer plane $\tilde{r}_{\rm E} = R_{\rm E} D_S/(D_S - D_L)$.

We show our best-fit parallax models in Figure 3.1, 3.2 and Table 3.2. We found each close and wide solutions has an additional degeneracy between $u_0 > 0(+)$ and $u_0 < 0(-)$. These four degenerate solutions have $\Delta\chi^2 \lesssim 4$. The parameters of the degenerate models are consistent with each other to within $1\sigma$ error except for $s$, $\alpha$ and $u_0$. The $\chi^2$ difference between the standard models and the parallax models is significantly large, $\Delta\chi^2 > 110$ for 2 dof difference.

It is known that low-level systematics in the baseline sometime mimic a high order signal. We therefore check whether the $\Delta\chi^2$ contributions come from where we theoretically expect. The top inset in Figure 3.3 shows the cumulative distribution for $\Delta\chi^2$ between the standard close model and the parallax close+ model as a function of time. Positive $\Delta\chi^2$ values indicate that the parallax model is favored over the standard model. We find $\Delta\chi^2 \sim 90$ comes from the data during the main peak of event in 2012 in both MOA and OGLE as expected, and $\Delta\chi^2 \sim 25$ comes from the data in 2013, the next year. The bottom right panel of Figure 3.1, which is a zoom of the 2013 data, shows slight differences among the models, i.e., the parallax models have the magnification of $\sim 1.05$ in the start of 2013 while the standard models have $\sim 1.00$. The bottom panel in Figure 3.3 shows binned residuals in bins 25 days wide. This shows the clear long-term deviation from the standard model. The binned data in the first half of 2013 are mostly above the standard model in both MOA and OGLE whereas those in the other years are not, which can be well explained by the parallax model. Because these long-term distortion are consistent in both MOA and OGLE, we conclude that these long-term signatures are real, and they are better explained by the parallax models compared to the standard models. Note that adding lens orbital motion does not improve our models. We also modeled the orbital motion of the source star due to the companion, called xallarap effect, and conclude that the parallax scenario is preferred over the xallarap scenario. See Tables 3.2 and 3.3 for the modeling results, and more detail in the Appendix B. We consider only the parallax model in the following sections.

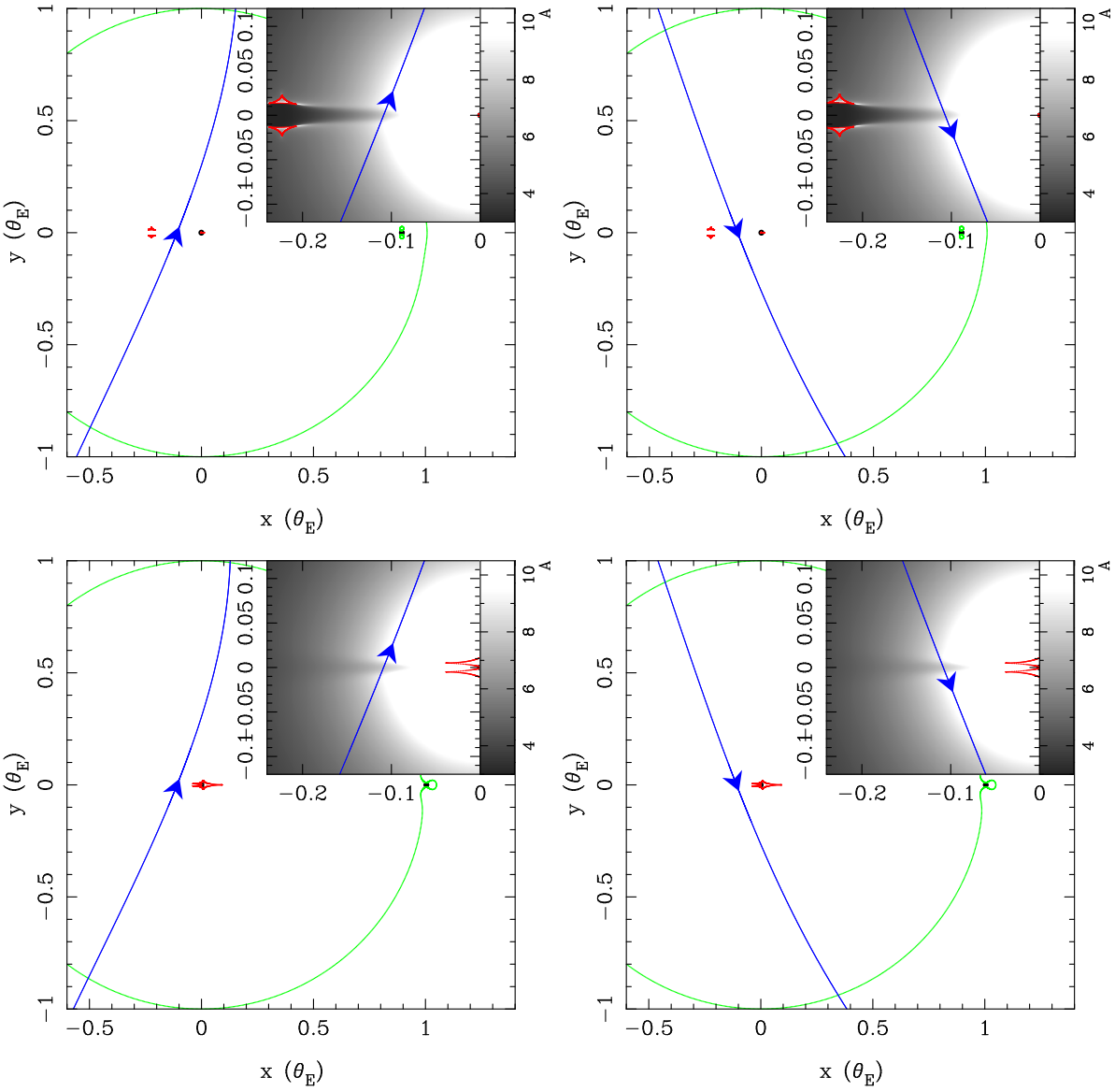


Figure 3.2: Caustics for the parallax models. The blue arrowed lines indicate the source trajectories. The top left, top right, bottom left, and bottom right shows the parallax close+, close−, wide+ and wide− models, respectively. A magnification map around the anomaly part is shown in the inset of each panel.

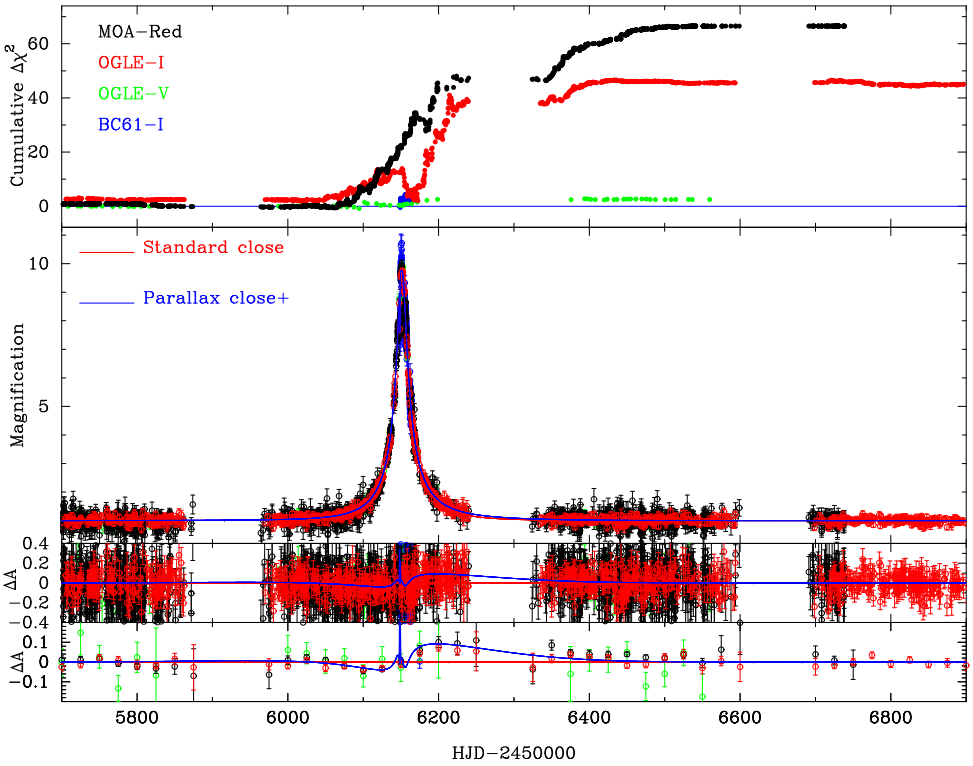


Figure 3.3: Cumulative distribution of $\Delta\chi^2$ between the Standard close model and the parallax close+ model. Top inset shows the distribution and a positive $\Delta\chi^2$ value indicates smaller $\chi^2$ value of the parallax close+ than that of the Standard close model. The second and third insets from the top shows the light curve and the residuals from the standard model, respectively. The bottom inset shows the residuals binned by 25 days for clarity.

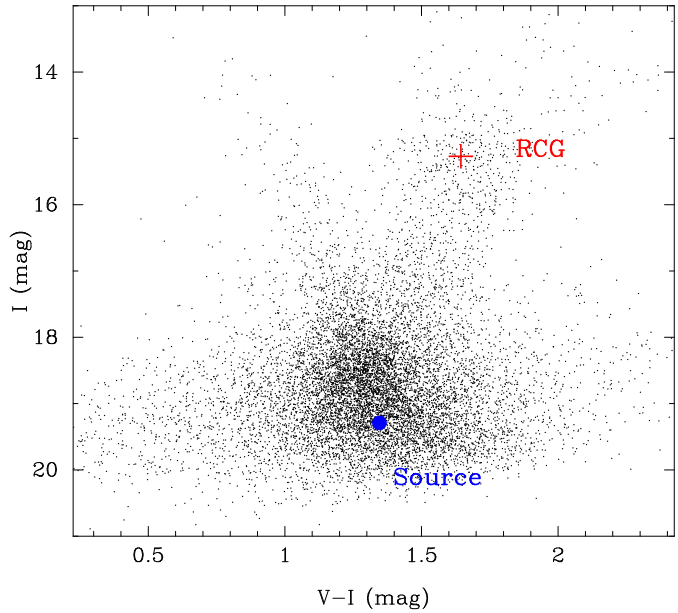


Figure 3.4: The OGLE-IV instrumental color-magnitude diagram of stars within $2' \times 2'$ around the source star. The source star and the mean of red clump giants are shown as the blue filled circle and the red cross, respectively.

## 3.5 The Angular Einstein Radius

We can place an upper limit on $\rho$ for the parallax models and a lower limit as well for the xallarap models. It is possible to derive a constraint on $\theta_{\rm E} = \theta_*/\rho$ by obtaining the angular source radius $\theta_*$. $\theta_*$ can be estimated from the source color, $(V-I)_S$, and the magnitude, $I_S$, empirically. We used the empirical relation by using a result of Boyajian et al. (2014) analysis,

$$\log\ [2\theta_*/(1\mathrm{mas})] = 0.5014 + 0.4197(V-I) - 0.2I. \tag{3.4}$$

This relation comes from a private communication with them, which is restricted to FGK stars with 3900 K $< T_{\rm eff} <$ 7000 K and the accuracy of relation is better than 2% (Fukui et al. 2015). We measured the source color and brightnesses $(V-I, I)_S = (1.346, 19.29) \pm (0.001, 0.03)$ with the OGLE-IV instrumental magnitude from the light curve fitting. Note that because the source color and magnitudes are nearly identical for all models (see Table 3.2), we adopt values of parallax close+ model in the following analysis. We correct their extinction following the standard procedure by Yoo et al. (2004) using the red clump giants (RCG) as a standard candle. Figure 3.4 shows a color-magnitude diagram (CMD) within the $2' \times 2'$ region around the source star with the OGLE-IV instrumental magnitude. The position of source and the measured RCG centroid $(V-I, I)_{RC} = (1.644, 15.27) \pm (0.011, 0.04)$ are shown as blue dot and red cross, respectively. Comparing the measured RCG centroid and the expected intrinsic position in this field $(V-$

$I, I)_{RC,0} = (1.06, 14.38) \pm (0.07, 0.04)$ by Bensby et al. (2013) and Nataf et al. (2013), we obtain the intrinsic source color and magnitude as $(V - I, I)_{S,0} = (0.76, 18.40) \pm (0.07, 0.07)$ with the assumption that the source extinction is same as that the RCG. Note that the original reddening and extinction values in the standard magnitude in this field can be measured by the catalog of OGLE-III photometry map (Szymański et al. 2011) as $E(V - I) = 0.68 \pm 0.07$ and $A_I = 0.86 \pm 0.06$. We use these original values to obtain $A_H$ in Section 3.6. Applying the intrinsic source color and magnitude to Equation (3.4), we obtain the angular source radius as $\theta_* = 0.69 \pm 0.05$ $\mu$as. From $\theta_*$, $\rho$ and $t_{\rm E}$, we can calculate the angular Einstein radius $\theta_{\rm E}$ and the lens-source relative proper motion $\mu_{rel}$,

$$\theta_{\rm E} = \theta_*/\rho > 0.22 \text{ mas}, \quad \mu_{rel} = \theta_{\rm E}/t_{\rm E} > 1.2 \text{ mas/yr}$$

for the parallax close+ model. Table 3.3 shows the derived parameters for all degenerate models using each models' values.

Table 3.3: Lens properties.

| Model | $P(f' \leq f)$ [1] % | $\theta_*$ ($\mu$as) | $\theta_{\rm E}$ (mas) | $\mu_{rel}$ (mas/yr) | $M_{\rm host}$ ($M_\odot$) | $M_{\rm p}$ ($M_\oplus$) | $D_L$ (kpc) | $r_\perp$ (AU) | $a$ (AU) |
|---|---|---|---|---|---|---|---|---|---|
| Parallax | | | | | | | | | |
| close+ | - | 0.69 ± 0.05 | $> 0.22$ | $> 1.2$ | $> 0.10$ | $> 7$ | $< 5.6$ | - | - |
| w/ KECK ($f$=0) | 62.6 | - | $1.09^{+0.16}_{-0.10}$ | $5.8^{+0.8}_{-0.6}$ | $0.57^{+0.06}_{-0.10}$ | $35^{+10}_{-6}$ | $2.6^{+0.5}_{-0.7}$ | $2.6^{+0.3}_{-0.5}$ | $3.1^{+1.5}_{-0.7}$ |
| w/ KECK ($f$=0.5) | 89.3 | - | $0.96^{+0.12}_{-0.09}$ | $5.1^{+0.6}_{-0.5}$ | $0.50^{+0.05}_{-0.09}$ | $31^{+9}_{-5}$ | $2.9^{+0.6}_{-0.8}$ | $2.4^{+0.2}_{-0.4}$ | $3.0^{+1.4}_{-0.5}$ |
| w/ KECK ($f$=0.9) | 95.4 | - | $0.64^{+0.06}_{-0.05}$ | 3.4±0.3 | $0.33^{+0.05}_{-0.08}$ | $21^{+6}_{-4}$ | $3.6^{+0.6}_{-0.8}$ | $2.1^{+0.2}_{-0.3}$ | $2.5^{+1.2}_{-0.6}$ |
| close− | - | 0.69 ± 0.05 | $> 0.22$ | $> 1.2$ | $> 0.13$ | $> 9$ | $< 5.8$ | - | - |
| w/ KECK ($f$=0) | 61.9 | - | $0.99^{+0.18}_{-0.06}$ | $5.3^{+1.0}_{-0.3}$ | $0.63^{+0.04}_{-0.11}$ | $41^{+9}_{-7}$ | $3.2^{+0.4}_{-0.9}$ | $2.8^{+0.2}_{-0.5}$ | $3.4^{+1.6}_{-0.8}$ |
| w/ KECK ($f$=0.5) | 88.8 | - | $0.86^{+0.15}_{-0.06}$ | $4.6^{+0.9}_{-0.3}$ | $0.55^{+0.03}_{-0.09}$ | $36^{+8}_{-6}$ | $3.4^{+0.4}_{-0.9}$ | $2.7^{+0.1}_{-0.4}$ | $3.3^{+1.5}_{-0.7}$ |
| w/ KECK ($f$=0.9) | 95.1 | - | $0.60^{+0.08}_{-0.04}$ | $3.2^{+0.4}_{-0.2}$ | $0.38^{+0.03}_{-0.08}$ | 25±5 | $4.2^{+0.4}_{-0.9}$ | $2.2^{+0.1}_{-0.3}$ | $2.7^{+1.3}_{-0.6}$ |
| wide+ | - | 0.69 ± 0.05 | $> 0.23$ | $> 1.2$ | $> 0.11$ | $> 8$ | $< 5.5$ | - | - |
| w/ KECK ($f$=0) | 63.3 | - | $1.14^{+0.11}_{-0.15}$ | $6.1^{+0.6}_{-0.8}$ | $0.54^{+0.09}_{-0.07}$ | $34^{+13}_{-4}$ | $2.4^{+0.8}_{-0.5}$ | 2.7±0.4 | $3.3^{+1.9}_{-0.7}$ |
| w/ KECK ($f$=0.5) | 89.4 | - | $0.99^{+0.08}_{-0.13}$ | $5.3^{+0.4}_{-0.7}$ | $0.47^{+0.08}_{-0.07}$ | $30^{+11}_{-4}$ | $2.6^{+0.8}_{-0.5}$ | 2.6±0.4 | $3.2^{+1.8}_{-0.6}$ |
| w/ KECK ($f$=0.9) | 95.6 | - | $0.66^{+0.04}_{-0.07}$ | $3.5^{+0.2}_{-0.4}$ | $0.31^{+0.07}_{-0.05}$ | $20^{+8}_{-3}$ | $3.4^{+0.8}_{-0.5}$ | 2.2±0.3 | $2.7^{+1.5}_{-0.5}$ |
| wide− | - | 0.69 ± 0.05 | $> 0.23$ | $> 1.2$ | $> 0.13$ | $> 9$ | $< 5.8$ | - | - |
| w/ KECK ($f$=0) | 62.1 | - | $0.99^{+0.17}_{-0.06}$ | $5.3^{+0.9}_{-0.4}$ | $0.63^{+0.05}_{-0.10}$ | $39^{+13}_{-4}$ | $3.2^{+0.4}_{-0.9}$ | $3.1^{+0.2}_{-0.5}$ | $3.8^{+1.9}_{-0.8}$ |
| w/ KECK ($f$=0.5) | 88.9 | - | $0.87^{+0.14}_{-0.07}$ | $4.7^{+0.8}_{-0.4}$ | $0.55^{+0.04}_{-0.09}$ | $34^{+11}_{-4}$ | $3.4^{+0.4}_{-0.9}$ | $3.0^{+0.2}_{-0.4}$ | $3.6^{+1.8}_{-0.8}$ |
| w/ KECK ($f$=0.9) | 95.1 | - | $0.60^{+0.07}_{-0.04}$ | $3.2^{+0.4}_{-0.2}$ | $0.38^{+0.04}_{-0.08}$ | $24^{+8}_{-3}$ | $4.2^{+0.4}_{-0.9}$ | $2.5^{+0.1}_{-0.3}$ | $3.1^{+1.5}_{-0.6}$ |
| **Mean** | - | **0.69 ± 0.05** | $\mathbf{0.99^{+0.26}_{-0.19}}$ | $\mathbf{5.3^{+1.4}_{-1.0}}$ | $\mathbf{0.56^{+0.12}_{-0.16}}$ | $\mathbf{35^{+17}_{-9}}$ | $\mathbf{3.0^{+0.8}_{-1.1}}$ | $\mathbf{2.7^{+0.6}_{-0.7}}$ | $\mathbf{3.4^{+2.4}_{-1.1}}$ |
| Xallarap | | | | | | | | | |
| close+ | - | $0.70^{+0.05}_{-0.06}$ | $0.20^{+0.04}_{-0.08}$ | $1.1^{+0.2}_{-0.4}$ | - | - | - | - | - |
| w/ KECK | - | - | - | - | $< 1.16$ | $< 77$ | $< 9.3$ | $< 1.7$ | - |
| close− | - | $0.70^{+0.05}_{-0.06}$ | $0.19^{+0.05}_{-0.07}$ | $1.0^{+0.3}_{-0.4}$ | - | - | - | - | - |
| wide+ | - | $0.70^{+0.05}_{-0.06}$ | $0.24^{+0.00}_{-0.11}$ | $1.3^{+0.0}_{-0.6}$ | - | - | - | - | - |
| wide− | - | $0.70^{+0.04}_{-0.07}$ | $0.20^{+0.05}_{-0.07}$ | $1.1^{+0.2}_{-0.4}$ | - | - | - | - | - |

**Notes.** A superscript or subscript of +/− 0.0 indicates that the parameter's best fit value is same as the 84/16 percentile to the given significant digits

[1] Probability of contamination fraction not exceeding $f$.

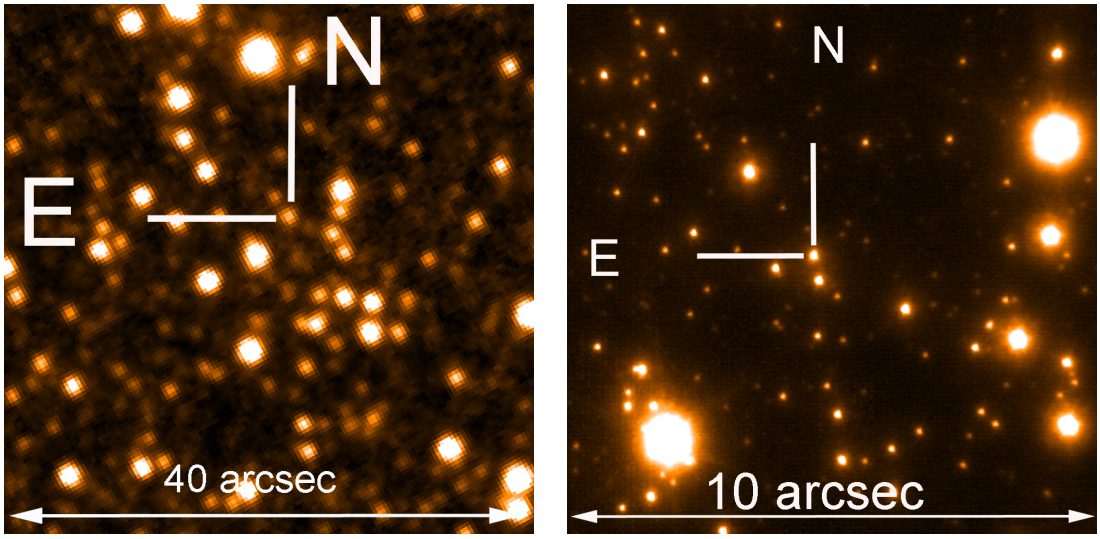


Figure 3.5: Images of the event field observed by VVV (left) and by Keck II (right). The indicated star is the target.

## 3.6 Excess Brightnesses from Keck AO Images

We have a mass–distance relation, the microlens parallax $\pi_{\rm E}$. If we can measure the lens flux which gives us an additional mass–distance relation, we could measure the mass and distance of the lens uniquely. We conducted high angular resolution observations using adaptive optics in order to measure the lens flux excluding as much flux from unrelated stars as possible.

### 3.6.1 Observations and the photometry

We observed OGLE-2012-BLG-0950 with the NIRC2 instrument on Keck II on July 18, 2013. We used the Wide camera with a pixel scale of 0.04 arcsec. We took 15 dithered $H$ frames with an exposure time of 30 seconds. We performed dark and flatfield corrections in the standard way. Furthermore, OGLE-2012-BLG-0950 was observed as part of the VVV survey (Minniti et al. 2010) using the VISTA 4m telescope at ESO. We extracted 3 arcmin VVV $JHK$ images centered on the target. We used the suite of tools developed as part of astr$O$matic (Bertin et al. 2002). We analyzed the PSF of the images using PSFEx, then we measured the fluxes with SExtractor (Bertin & Arnouts 1996) using these PSF models. We cross identified 2MASS stars with VVV sources, and derived an absolute calibration of the VVV $JHK$ images. We used the VVV images which we reprocessed as a reference to perform an astrometric calibration of one Keck frame. We then extracted the sources from this individual frame, and used them as a reference to

realign all the Keck frames. We stacked the Keck frames with the SWARP tool (Bertin et al. 2002). We then performed aperture photometry on the Keck frame (for more details, see Batista et al. 2014). We cross identified common sources between Keck and VVV, and finally derived the calibration constant for Keck $H$ band photometry.

Fig. 3.5 shows the field as observed by VVV and by Keck. First, we notice that the source in VVV is resolved in 2 objects with Keck. Using the astrometry on the amplified source, we are able to identify the source+lens of the microlensing as being the star that is marked on the frame. Its coordinates are $(R.A., Dec.)_{J2000}$ = (18:08:04.620, -29:43:53.43). It has a Keck $H$ band magnitude of

$$H_{\rm target} = 16.89 \pm 0.02 \tag{3.5}$$

in the 2MASS magnitude system. The blend to the south is at coordinates $(R.A., Dec.)_{J2000}$ = (18:08:04.612, -29:43:53.88) and is slightly fainter at $H = 16.99 \pm 0.03$.

### 3.6.2 The excess flux

Considering a full width at half maximum of the target $\rm FWHM_{target} = 90$ mas in Keck image and the lens-source relative proper motion, $H_{\rm target}$ includes the lens flux plus the source flux. Here we derive the excess brightness by subtracting the source system brightness, which can be used as the lens flux or its upper limit. Hereafter we represent our derived values for only parallax close+ model as the parallax model unless otherwise stated.

Unfortunately, we don't have a light curve in the $H$-band, so we derived the source $H$ magnitude as $H_{S,0} = 17.55 \pm 0.12$ by converting the magnitude from $(V - I, I)_{S,0}$ with the color-color relation by Bessell & Brett (1988). Next, we applied the $E(V - I)$ and $A_I$ values derived in Section 3.5 and estimated the extinction in $H$-band as $A_H = 0.25 \pm 0.02$ (Cardelli et al. 1989). The magnification at the time of Keck observation of $\rm HJD' = 6491.88$ is $A = 1.005$ for the parallax model. Thus, the source apparent $H$ magnitude at the time is $H_{S,\rm KECK} = 17.78 \pm 0.12$. This value is converted to the 2MASS magnitude system from the Bessel & Brett system using Equations (A1) - (A4) in Carpenter (2001). Subtracting this from $H_{\rm target}$ of Equation (3.5), we derive the excess brightness of

$$H_{\rm excess} = 17.52 \pm 0.10. \tag{3.6}$$

### 3.6.3 Probability of the contamination fraction $f$

We next consider the probability that part of the $H_{\rm excess}$ come from stars not the lens. To estimate the probability of the contamination fraction $f$, we consider

the following three possible sources of contamination: unrelated ambient stars, a companion to the source star and a companion to the lens star (Batista et al. 2014, Fukui et al. 2015).

### Unrelated ambient stars

First, we estimate the probability of contamination owing to unrelated ambient stars. Counting the number of stars with $H > H_{\rm excess}$ on the Keck image, we estimate the number density of stars with brightnesses corresponding to $0 < f < 1$ as 0.68 arcsec$^{-2}$. Similarly, the number density of stars corresponding to $0.5 < f < 1$ and $0.9 < f < 1$ are estimated as 0.11 arcsec$^{-2}$, 0.01 arcsec$^{-2}$, respectively.

We can resolve an ambient star only if it is separated from the source by FWHM = 90 mas or more. Thus, the probability of contamination owing to unrelated ambient stars within 90 mas around the source, $P_{\rm amb}$, are $P_{\rm amb}(0 < f < 1) = 1.74\%$, $P_{\rm amb}(0.5 < f < 1) = 0.29\%$ and $P_{\rm amb}(0.9 < f < 1) = 0.03\%$.

### Companion to the source star

Second, we estimate the probability of contamination owing to a companion to the source. Because we can detect a companion on the Keck images if the companion is located far enough from the source and the light curve will be affected if the companion is located close enough to the source, an undetectable companion should be located between the two detection limits. We put the distant limit as 90 mas from the FWHM of the target. For the close limit, we consider $a_{SC,\rm low}$ defined in the following.

As we can find in the bottom inset in Figure 3.3, the OGLE $I$ data in the light curve is sensitive enough to a deviation with an amplitude of $\Delta A \simeq 0.1$ and a duration of hundreds of days. That means we can detect a binary source signal when a companion to the source is magnified with an amplitude of $\gtrsim 0.1 f_S$ and a duration of hundreds of days. Such a small signal cannot be detected if they are longer than $10t_{\rm E} \sim 670$ days. We assume that we can detect the signal caused by a magnified companion to the source star when the time variation of the companion flux is larger than $0.1 f_S$ within $10t_{\rm E}$, that is, it requires

$$A(u_{C,0}) f_C - A\left(\sqrt{5^2 + u_{C,0}^2}\right) f_C \leq 0.1 f_S \tag{3.7}$$

to be "undetected", where 5 comes from half of "10" $t_{\rm E}$ and $u_{C,0}$ and $f_C$ are the impact parameter and the flux in $I$-band of the companion star, respectively. $A(u_C)$ is the magnification when the companion is located at $u_C$ and we use the magnification of single lens $A(u) = (u^2 + 2)/u\sqrt{u^2 + 4}$ as $A(u_C)$. Because

$A\left(\sqrt{5^2+u_{C,0}^2}\right) < A(5)$, we can express the condition more conservatively,

$$\begin{aligned} & A(u_{C,0})f_C - A(5)f_C \leq 0.1 f_S \\ \Leftrightarrow\ & u_{C,0} \geq u_C \left(1.00275 + 0.1\frac{f_S}{f_C}\right) \equiv u_{C,0,\mathrm{low}}. \end{aligned} \tag{3.8}$$

The $u_{C,0,\mathrm{low}}$ is a lower limit of the impact parameter of the companion to be undetected and it gives us a lower limit of the separation between the source and the companion as $s_{SC} > s_{SC,\mathrm{low}}$. When the time when the companion is located at $u_C = u_{C,0}$ is defined as $t_{C,0}$, it is possible to give the most conservative lower limit as $s_{SC} > s_{SC,\mathrm{low}} \equiv |u_{C,0,\mathrm{low}} - |u_0||$ when $t_{C,0} = t_0$ and the closest companion crosses the same side as the source relative to the lens. Thus, we derive the lower limit of the semi-major axis of the source system as $a_{SC,\mathrm{low}} \equiv D_S \theta_\mathrm{E} s_{SC,\mathrm{low}}$.

To calculate $u_{C,0,\mathrm{low}}$ in $a_{SC,\mathrm{low}}$, we obtain $M_{I,C}$ by converting $M_{H,C} = H_\mathrm{excess} - 2.5\log f - 5\log(D_S/10\mathrm{pc})$ to $M_{I,C}$ using PARSEC isochrones version 1.2S (Bressan et al. 2012, Chen et al. 2014, 2015, Tang et al. 2014) with $D_S = 8$kpc for the calculation of $f_S/f_C = 10^{-0.4(M_{I,S}-M_{I,C})}$ in Equation (3.8) where $M_{I,S}$ and $M_{I,C}$ are absolute $I$ magnitudes of the source and the companion.

Because $a_{SC,\mathrm{low}}$ and $\theta_\mathrm{E}$ vary with $f$, we calculate the probability of contamination owing to a companion to the source using following formula (cf. Fukui et al. 2015),

$$P(f_1 < f < f_2) = F_\mathrm{binary} \times \int_{f_1}^{f_2} F_{a_c}(f) \times F_{q_c}(f) df \tag{3.9}$$

where $F_\mathrm{binary}$ is the multiplicity of FGK-dwarfs, $F_{a_c}(f)$ is the fraction of binaries with a separation of $a_{SC,\mathrm{low}}(f) < a_c < 90\mathrm{mas} \times D_S$ and $F_{q_c}(f)df$ is the fraction of binaries with a mass ratio between $q_c(f)$ and $q_c(f+df)$. We derive $M_C(f)$ from $M_{H,C}(f)$ using the PARSEC isochrones version 1.2S for the calculation of $q_c(f)$. We use the distribution of parameters for FGK binaries by Raghavan et al. (2010): $F_\mathrm{binary} = 0.46$ as the multiplicity, a log normal distribution with the mean of $\log P_c(\mathrm{days}) = 5.03$ and the standard deviation of $\sigma_{\log P_c} = 2.28$ as the period distribution and Figure 16 in the paper as the mass ratio distribution. We apply the period distribution by converting $a_c$ to a period using Kepler's 3rd law. Then we obtain $P_{SC}(0 < f < 1) = 22.0\%$, $P_{SC}(0.5 < f < 1) = 3.2\%$, $P_{SC}(0.9 < f < 1) = 0.7\%$ for the parallax close+ model.

### Companion to the lens star

Next, we estimate the probability for contamination owing to a companion to the lens star. In this case, we again use Equation (3.9) to calculate the probability because the lens mass, the distance to the lens and the companion mass values

are dependent on the $f$ value in addition to $\theta_{\rm E}$. However, the definition of $F_{a_c}(f)$ is different here. To place close limits on $a_c$, we consider the shear given by a hypothetical lens companion (Batista et al. 2014). Assuming that we can detect the shear effect when the width of the central caustic created by the companion, $w_c \simeq 4q_c/s_c^2$, is larger than the width of that by the planet, $w$, we can place a detection limit as $w_c < w$, where $s_c$ is the projected separation normalized by $\theta_{\rm E}$ between the host and a hypothetical companion of the lens. This inequality gives us a close limit on $a_c$.

Adopting 90 mas as the distant limit again, $F_{a_c}(f)$ here is defined as the fraction of binaries with a projected separation of $2\sqrt{q_c(f)/w}\theta_{\rm E}(f)D_L(f) < a_c < 90{\rm mas} \times D_L(f)$ where $w = 4q/(s-s^{-1})^2 \simeq 0.016 \sim 0.02$ for the close models. We apply $w = 0.02$ to the wide model as well as the close model considering that the shear effect by a hypothetical companion is almost equal to that for the close model because the magnification map on the source trajectory for the wide models is almost same as the close models. Note that uncertainties arising from any assumptions here do not affect the results largely because they are too small compared to the range of $a_c$ values we are considering.

We calculate $q_c(f)$ for each $f$ value using isochrone models as well as the source companion case. Because a primary of the lens can be either an M dwarf or FGK dwarf depending on the $f$ value, we use the distributions for FGK-dwarf binaries by Raghavan et al. (2010) for $M_{\rm prim}(f) > 0.7$ and that for KM-dwarf binaries by Ward-Duong et al. (2015) for $M_{\rm prim}(f) \leq 0.7$. Ward-Duong et al. (2015) gives $F_{\rm binary} = 0.347$ as the multiplicity, a log normal distribution with the mean of $\log a_c({\rm AU}) = 0.77$ and the standard deviation of $\sigma_{\log a_c} = 1.34$ as the distribution of the projected separation and a mass ratio distribution that is flat for $0.2 < q_c < 1$ and 0 for $q_c < 0.2$. Integrating Equation (3.9) with these distributions and the detection limits, we derive $P_{LC}(0 < f < 1) = 13.7\%$, $P_{LC}(0.5 < f < 1) = 7.2\%$ and $P_{LC}(0.9 < f < 1) = 3.9\%$ for the parallax close+ model.

### Total probability of contamination

Finally, by summing the probabilities for the three sources mentioned above, we can calculate the following total probabilities of contamination: $P(0 < f < 1) = 37.4\%$, $P(0.5 < f < 1) = 10.7\%$, $P(0.9 < f < 1) = 4.6\%$ assuming the parallax close+ model. Therefore, the probabilities of the contamination fraction not exceeding $f$ shown in Table 3.3 can be calculated as $P(f = 0) = 1 - P(0 < f < 1) = 62.6\%$, $P(f \leq 0.5) = 1 - P(0.5 < f < 1) = 89.3\%$ and $P(f \leq 0.9) = 1 - P(0.9 < f < 1) = 95.4\%$ for the parallax close+ model. The probabilities for all parallax models are shown in Table 3.3.

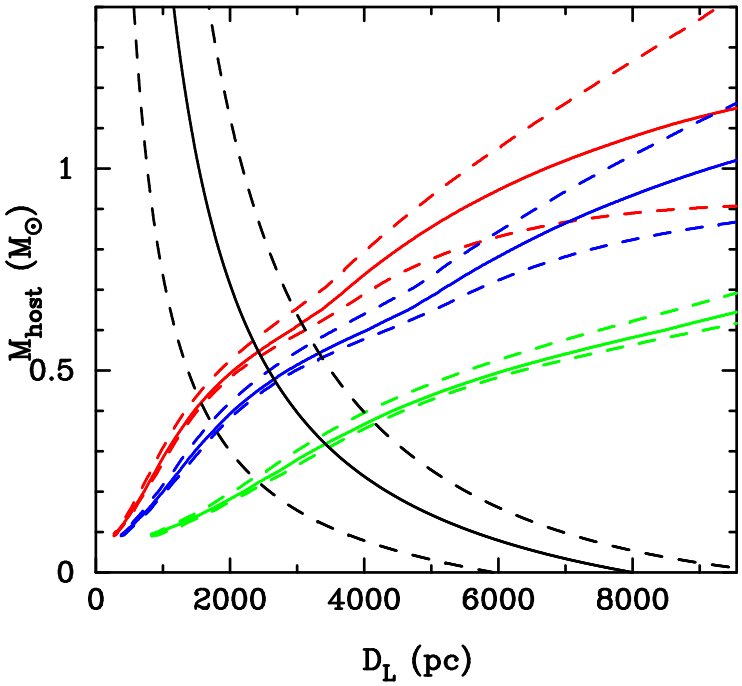


Figure 3.6: Mass–distance relations for the parallax close+ model. The relations from $M_{H,L}$ are shown in red, blue and green for a contamination fraction of $f = 0$, 0.5 and 0.9, respectively. The dashed lines indicate 1 $\sigma$ error including the uncertainty of the distance to the source, the lens age and the lens metallicity in addition to the uncertainty of our measuring. Black lines are the mass–distance relation come from $\pi_{\rm E}$.

## 3.7 Lens Properties

In this section, we constrain the lens properties from microlens parallax and the lens flux. All results are summarized in Table 3.3.

We have two mass–distance relations for the parallax model. One is the lens absolute magnitude,

$$M_{H,L} = H_L - A_{H,L} - 5\log\frac{D_L}{10\mathrm{pc}}, \quad (H_L = H_{\rm excess} - 2.5\log(1-f)) \qquad (3.10)$$

where $f$ is the fraction of contamination flux to excess flux and $A_{H,L}$ is an extinction for the lens located at $D_L$ and we adopted $A_{H,L} = A_H D_L/D_S$ following to Fukui et al. (2015). This is converted to a relationship between the host mass $M_{\rm host}$ and the distance $D_L$ by using isochrone models from the PARSEC isochrones, version 1.2S (Bressan et al. 2012, Chen et al. 2014, Tang et al. 2014, Chen et al. 2015).

The other mass–distance relation is from the microlens parallax $\pi_{\rm E}$:

$$M_{\rm host} = \frac{1}{1+q}\frac{\pi_{\rm rel}}{\kappa \pi_{\rm E}^2} \tag{3.11}$$

where $\kappa = 8.144$ mas $M_\odot^{-1}$ and $\pi_{\rm rel} = {\rm AU}\ (1/D_L - 1/D_S)$.

Figure 3.6 shows these two relations for the parallax close+ model. Black lines are the mass–distance relation come from $\pi_{\rm E}$. The red, blue and green lines indicate the relation from $M_{H,L}$ for the case of $f$=0, 0.5 and 0.9, respectively. Dashed lines indicate 1 $\sigma$ errors and they include the uncertainty of the distance to the source of $D_S = 8.0 \pm 1.6$ kpc, the lens age of $< 13$ Gyr and the lens metallicity of [Fe/H] $= -0.05 \pm 0.20$ in addition to the uncertainty of our measurements. We adopt the metallicity distribution of nearby M- or late K-dwarf stars (e.g., Gaidos et al. 2014) for the metallicity. Note that the dependency on age is much weaker than that on metallicity in the region of the parallax solution.

The region overlapping these two relations corresponds to the allowed solution. For $f = 0$, the host mass is $M_{\rm host} = 0.57^{+0.06}_{-0.10} M_\odot$ and the distance is $D_L = 2.6^{+0.5}_{-0.7}$ kpc, and the planet mass is $M_{\rm p} = 35^{+10}_{-6} M_\oplus$, its projected separation is $r_\perp = 2.6^{+0.3}_{-0.5}$ AU and the three-dimensional star-planet separation is statistically estimated as $a = 3.1^{+1.5}_{-0.7}$ AU with a circular orbit assumption (Gould & Loeb 1992). From this solution, we can calculate the angular Einstein radius and the relative lens-source proper motion as $\theta_{\rm E} = 1.09^{+0.16}_{-0.10}$ mas and $\mu_{\rm rel} = 5.8^{+0.8}_{-0.6}$ mas/yr, respectively. The solution of $M_{\rm host} = 0.50^{+0.05}_{-0.09} M_\odot$, $D_L = 2.9^{+0.6}_{-0.8}$ kpc for $f = 0.5$ is consistent with that for $f = 0$ within $1\sigma$. In addition, the solution for $f = 0.9$ is $M_{\rm host} = 0.33^{+0.05}_{-0.08} M_\odot$, $D_L = 3.6^{+0.6}_{-0.8}$ kpc. Our estimate for these contamination probabilities is discussed in Section 3.6.3 and summarized also in Table 3.3.

In any case, the host star is an M/K dwarf and the planet is a Neptune/sub-Saturn mass planet. All solutions of the other degenerate parallax models are similar to these results as shown in Table 3.3. We present the mean value of the 8 parallax solutions with $f = 0$ and $f = 0.5$ without any weight as "Mean" in Table 3.3. Here the contributions of solutions with $f > 0.5$ are negligible.

## 3.8 Discussion and Conclusion

We analyzed the microlensing event OGLE-2012-BLG-0950. A negative perturbation in the microlensing light curve consistent with a low-mass planet was detected (Abe et al. 2013). All the models we analyzed have a planetary mass ratio, $q \simeq 2 \times 10^{-4}$. We could not detect a significant finite source effect because the source did not cross any caustic, but detect a parallax signal. The parallax solutions indicate a Neptune/sub-Saturn mass planet with mass of $M_{\rm p} = 35^{+17}_{-9} M_\oplus$ around an M/K-dwarf host with mass of $M_{\rm host} = 0.56^{+0.12}_{-0.16} M_\odot$. We measured the

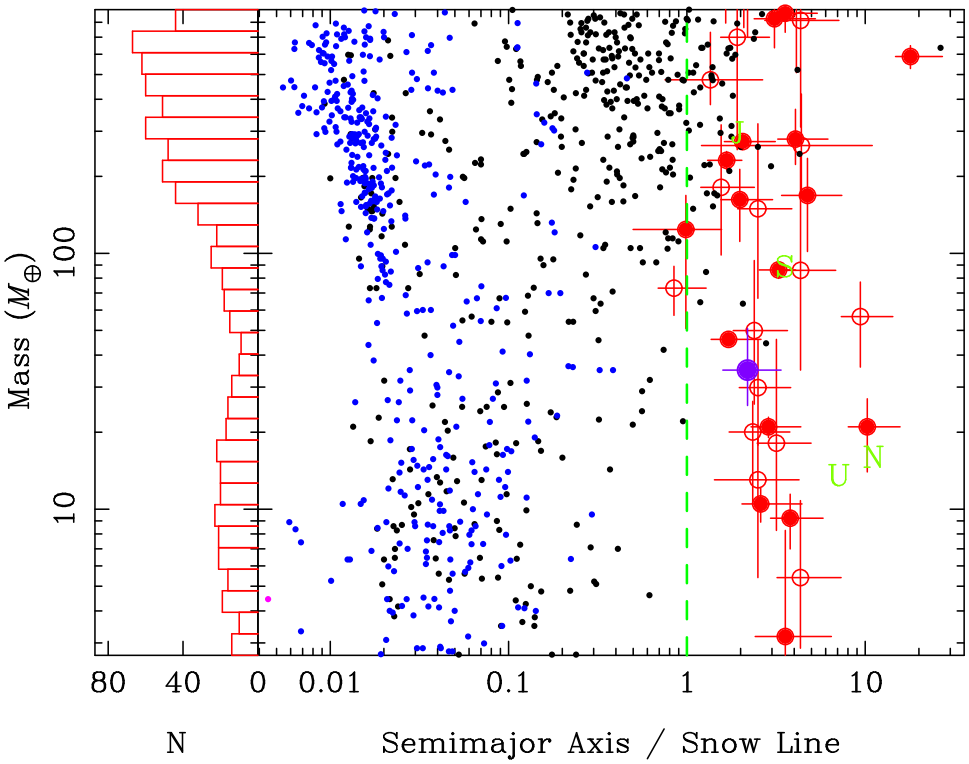


Figure 3.7: Mass versus semi-major axis normalized by the snow-line of discovered exoplanets so far. Here the snow line is estimated by the host star mass as $\sim 2.7\mathrm{AU}\,(M/M_\odot)$ (Kennedy & Kenyon 2008). The black and blue dots and red circles indicate planets found by the radial velocity, transit and microlensing, respectively. The result of this work is indicated as the purple circle. In microlensing planets, filled circles indicates that their masses are measured and open circles indicate that their masses are estimated by a Bayesian analysis. Green letters indicate solar system planets.

lens mass by combining microlens parallax and the lens flux obtained by Keck AO observations. This is the first case in which the lens mass was measured using only microlens parallax and the lens flux.

The planet orbits outside of the snow line of the host star and has a mass between that of Neptune and Saturn, $M_{\rm p} = 35^{+17}_{-9} M_{\oplus}$. Planets with this mass range (intermediate mass, hereafter) are predicted to be rare inside the snow line, but to be common like Neptune- or Saturn- mass planets outside the snow line according to the core accretion theory (Ida & Lin 2004, Ida et al. 2013). A paucity of intermediate mass planets orbiting close to their metal-poor host stars is confirmed (Beaugé & Nesvorný 2013). On the other hand, the predicted relative abundance outside the snow line has not been confirmed yet. Figure 3.7 shows the distribution of the exoplanets[1] discovered so far. The solution of our parallax model is indicated as the purple filled circle located just around the valley of the bimodal mass distribution histogram on the left side of the figure. Note that this distribution is not corrected for detection efficiency. Only a few intermediate mass planets orbiting outside the snow line have been discovered by the RV and microlensing methods. The parallax model of this work could be the second such intermediate mass exoplanet with mass measurement, following OGLE-2012-BLG-0026Lb (Han et al. 2013, Beaulieu et al. 2016). The masses of other intermediate-mass planets are estimated by Bayesian analysis (Miyake et al. 2011, Poleski et al. 2014, Skowron et al. 2016b). However, the Bayesian estimates depend on the choice of prior (Bennett et al. 2014, Skowron et al. 2015).

In a future space-based microlensing survey by *WFIRST* (Spergel et al. 2015) and *Euclid* (Penny et al. 2013), in the survey of Campaign 9 of the *K2* Mission (Henderson et al. 2016) conducted from April 2016 to July 2016, or *Spitzer* microlensing campaign from 2014 (Yee et al. 2015), it is very important and easier to determine the lens mass for each event by combining microlens parallax and lens flux as pointed out by Yee (2015) for the following reasons. First, space- and ground-based simultaneous observations are expected to obtain microlens parallax for a significant fraction of events regardless of number of the lens bodies, in contrast to the finite source effect which can be obtained only by observing the peak of high-mag event or caustic crossing. Second, for low-mass and nearby lenses, the mass–distance relations derived from flux and from $\theta_{\rm E}$ are partially degenerate (see Figure 2 in Yee 2015 or Figure 7 in Fukui et al. 2015) although we can obtain $\theta_{\rm E}$ by the measurement of astrometric microlensing effects with the precision of *WFIRST* (Gould & Yee 2014). Third, the cases without detection of $\theta_{\rm E}$ like this event are expected to increase even for planetary events because a higher precision and higher cadence survey can detect more subtle planetary signals including cases without crossing caustics (Zhu et al. 2014). Finally, it is possible to measure the

[1] http://exoplanet.eu

lens fluxes even after the events by follow-up observations with high angular resolution, and ultimately, *WFIRST* and *Euclid* can routinely measure the lens fluxes as part of the survey observations. Our analysis for the parallax model is the first demonstration of the mass measurement from only microlens parallax and the lens flux, and thus, it has particular significance for the developing era of space-based microlensing.

# Chapter 4

# MOA-2016-BLG-227Lb: A Massive Planet Characterized by Combining Lightcurve Analysis and Keck AO Imaging

We report the discovery of a microlensing planet — MOA-2016-BLG-227Lb — with a large planet/host mass ratio of $q \simeq 9 \times 10^{-3}$. This event was located near the *K2* Campaign 9 field that was observed by a large number of telescopes. As a result, the event was in the microlensing survey area of a number of these telescopes, and this enabled good coverage of the planetary light curve signal. High angular resolution adaptive optics images from the Keck telescope reveal excess flux at the position of the source above the flux of the source star, as indicated by the light curve model. This excess flux could be due to the lens star, but it could also be due to a companion to the source or lens star, or even an unrelated star. We consider all these possibilities in a Bayesian analysis in the context of a standard Galactic model. Our analysis indicates that it is unlikely that a large fraction of the excess flux comes from the lens, unless solar type stars are much more likely to host planets of this mass ratio than lower mass stars. We recommend that a method similar to the one developed in this paper be used for other events with high angular resolution follow-up observations when the follow-up observations are insufficient to measure the lens-source relative proper motion.

## 4.1 Introduction

Gravitational microlensing is a powerful method for detecting extrasolar planets (Mao & Paczynski 1991, Gould & Loeb 1992, Gaudi 2012). Compared to other

detection techniques, microlensing is sensitive to low-mass planets (Bennett & Rhie 1996) orbiting beyond the snow line around relatively faint host stars like M dwarfs or brown dwarfs (Bennett et al. 2008, Sumi et al. 2016), which is complementary to other methods.

A difficulty with the microlensing method is the determination of the mass of a lens $M_L$ and the distance to the lens system $D_L$. If we have an estimate for the angular Einstein radius $\theta_E$ and the microlens parallax $\pi_E$, the mass is directly determined by

$$M_L = \frac{\theta_{\rm E}}{\kappa \pi_{\rm E}} \ , \tag{4.1}$$

where $\kappa = 8.144$ mas $M_\odot^{-1}$ (Gould 1992, Gaudi et al. 2008, Muraki et al. 2011). When the source distance, $D_S \sim 8$ kpc, is known, the distance to the lens is given by

$$D_L = \frac{\rm AU}{\pi_E \theta_E + \pi_S}, \tag{4.2}$$

where $\pi_S \equiv {\rm AU}/D_S$. However, the microlens parallax can be observed for a fraction of planetary events, while the angular Einstein radius is observed for most planetary events.

One strategy to estimate $M_L$ and $D_L$ for events in which microlens parallax cannot be detected is to use a Bayesian analysis based on probability distributions from a standard Galactic model (e.g., Beaulieu et al. 2006; Bennett et al. 2014; Koshimoto et al. 2014; Shvartzvald et al. 2014). However, such an analysis must necessarily make an assumption about the probability that stars of a given mass and distance will host a planet. The most common assumption is that all stellar microlens stars are equally likely to host a planet with the properties of the microlens planet in question. It may be that the probability of hosting a planet of the measured mass ratio and separation depends on the host mass or the distance from the Galactic center. But, without mass and distance measurements, these quantities are determined by our Bayesian prior assumptions. As a case in point, Bennett et al. (2014) analyzed MOA-2011-BLG-262 and found a planetary mass host orbited by an Earth-mass "moon" model had almost the same likelihood as a star+planet model. But, since we have no precedent for such a rogue planet+moon system, they selected the more conventional star+planet system as the favored model. Also, the first discovered microlensing planet, OGLE-2003-BLG-235Lb, was at first thought to be a giant planet orbiting an M dwarf with a mass of $M_* \sim 0.36 M_\odot$ from a Bayesian analysis (Bond et al. 2004). Such a system is predicted to be rare according to the core accretion theory of planet formation (Laughlin et al. 2004, Kennedy & Kenyon 2008). Follow-up *HST* images revealed a more massive host star with mass of $M_* = 0.63^{+0.07}_{-0.09} M_\odot$ by detecting excess flux in multiple passbands (Bennett et al. 2006).

When we measure the lens flux with high angular resolution *HST* or adaptive optics (AO) images (e.g., Bennett et al. 2006, 2007, 2015; Batista et al. 2015), we can then calculate the lens mass $M_L$ using a mass-luminosity relation combined with the mass–distance relation derived from $\theta_E$ measurement. High angular resolution images are needed because microlensed source stars are generally located in dense Galactic bulge fields where there are usually multiple bright main sequence stars per ground-based seeing disk.

Because the size of the angular Einstein radius is $\lesssim 1\,\mathrm{mas}$, and the lens-source relative proper motion is typically $\mu_{\rm rel} \sim 6\,\mathrm{mas/yr}$, it is possible that the lens and source stars will remain unresolved even in high angular resolution images taken within a few years of the microlensing event. In such cases, there will be excess flux above that contributed by the source star and this excess flux must include the lens star flux. Some studies (Batista et al. 2014, Fukui et al. 2015, Koshimoto et al. 2017a), which detected an excess flux, have assumed that this excess flux is dominated by the lens flux, and they have derived the lens mass under this assumption.

With this method, it might seem that no assumptions are required regarding the probability of the microlens stars to host planets, and there would be no biases due to any inadequacies of the Galactic model used. However, Bhattacharya et al. (2017) use *HST* imaging to show that the excess flux at the position of the MOA-2008-BLG-310 source is *not* due to the lens star, and Koshimoto et al. (2018, in preparation)have developed a Bayesian method to study the possibility of excess flux from stars other than the lens star. Possibilities include unrelated stars, and companions to the source and lens stars. They find that it can be difficult to exclude all these contamination scenarios, especially for events with small angular Einstein radii. In those cases where we cannot exclude the contamination scenarios, we can again use a Bayesian analysis similar to the one described above to estimate the probability distribution of the lens properties. This means that we need to assume prior distributions for stellar binary systems and the stellar luminosity function even when we have detected excess flux in high angular resolution images. In cases where the lens properties are confirmed by a measurement of the lens-source relative proper motion (Bennett et al. 2015, Batista et al. 2015) or microlensing parallax measurements (Gaudi et al. 2008, Beaulieu et al. 2016, Bennett et al. 2016), this contamination can be ruled out. Attempts at lens-source relative proper motion measurements can also confirm contamination (Bhattacharya et al. 2017) in cases where the measured proper motion of the star responsible for the excess flux does not match the microlensing light curve prediction.

In this paper, we report the discovery of the planetary microlensing event MOA-2016-BLG-227. Observations and data reduction are described in Sections 4.2 and

4.3. Our modeling results are presented in Section 4.4. In Section 4.5, we model the foreground extinction by comparing observed color magnitude diagrams (CMDs) to different extinction laws and compare the results from the different extinction laws. Then, we use the favored extinction law to determine the angular Einstein radius, $\theta_{\rm E}$. In Section 4.6, we describe our Keck AO observations and photometry, and we determine the excess flux at the position of the source. In Section 4.7, we describe our Bayesian method to determine the probability that this excess flux is due to lens star and various combinations of other "contaminating" stars. The posterior probabilities for this MOA-2016-BLG-227 planetary microlensing event are presented, and we consider the effect of different planet hosting probability priors. Finally, we discuss and conclude the results of our work in Section 4.8.

## 4.2 Observations

The Microlensing Observations in Astrophysics (MOA; Bond et al. 2001, Sumi et al. 2003) group conducts a high cadence survey towards the Galactic bulge using the 2.2-deg$^2$ FOV MOA-cam3 (Sako et al. 2008) CCD camera mounted on the 1.8 m MOA-II telescope at the University of Canterbury Mt. John Observatory in New Zealand. The MOA group alerts about 600 microlensing events per year. Most observations are conducted in a customized MOA-Red filter which is similar to the sum of the standard Cousins $R$-and $I$-band filters. Observations with the MOA $V$ filter (Bessell $V$-band) are taken once every clear night in each MOA field.

The microlensing event MOA-2016-BLG-227 was discovered and announced by the MOA alert system (Bond et al. 2001) at (R.A., Dec.)$_{J2000}$ = (18:05:53.70, -27:42:51.43) and $(l, b) = (3.303°, -3.240°)$ on 5 May 2016 (HJD$' \equiv$ HJD - 2450000 $\sim$ 7514). This event occurred during the microlensing Campaign 9 of the *K2* Mission (*K2*C9; Henderson et al. 2016) and it was located close to (but not in) the area of sky that was surveyed for the *K2*C9. This part of the *K2* field that was downloaded at 30-min intervals is known as the "superstamp." Because this event was so close to the superstamp, several other groups conducting observing campaigns coordinated with the *K2*C9 observations also observed this event.

The Wise group used the Jay Baum Rich telescope, a Centurion 28 inch telescope (C28) at the Wise Observatory in Israel, which is equipped with a 1 deg$^2$ camera. The group monitored the *K2*C9 superstamp during the campaign with six survey fields that were observed 3–5 times per night with the Astrodon Exo-Planet BB (blue-blocking) filter. Although the MOA-2016-BLG-227 target was just outside the *K2*C9 superstamp, it was still within the Wise survey footprint.

The event was also observed with the wide-field near infrared (NIR) camera (WFCAM) on the UKIRT 3.8m telescope on Mauna Kea, Hawaii, as part of a NIR microlensing survey in conjunction with the *K2*C9 (Shvartzvald et al. 2017a)

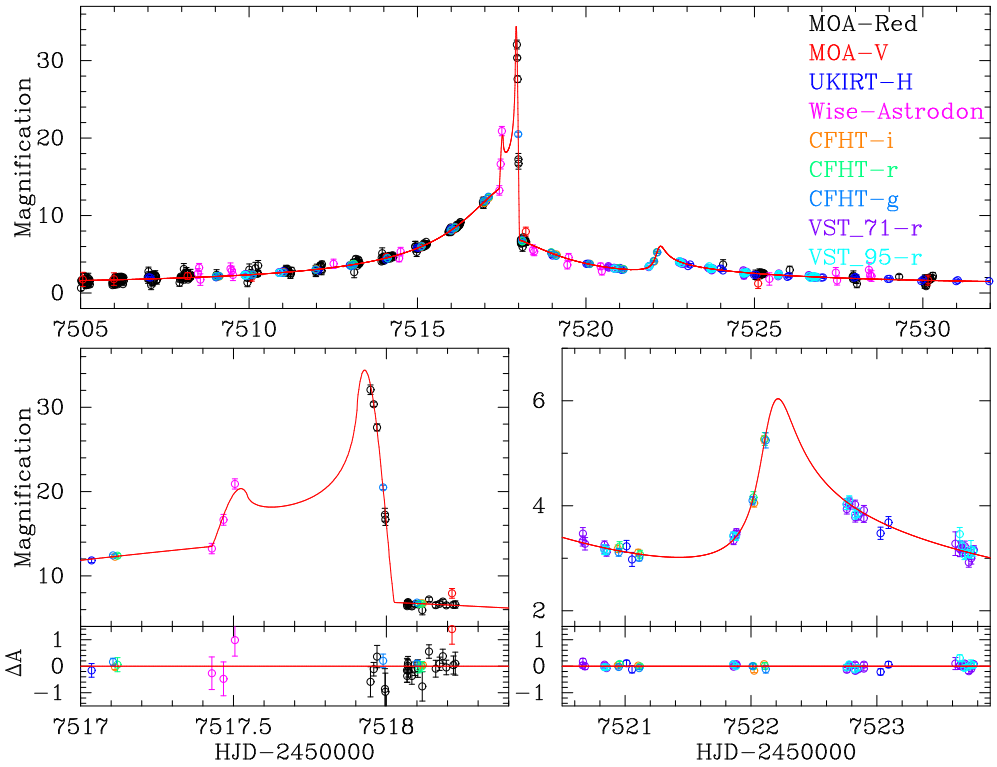


Figure 4.1: The light curve data for MOA-2016-BLG-227 is plotted with the best-fit model. The top panel shows the whole event, the bottom left and bottom right panels highlight the caustic crossing feature and the second bump due to the cusp approach, respectively. The residuals from the model are shown in the bottom insets of the bottom panels.

survey. The UKIRT survey covered 6 deg$^2$, including the entire *K2*C9 superstamp and extending almost to the Galactic plane, with a cadence of 2–3 observations per night. Observations were taken in $H$-band, with each epoch composed of sixteen 5-second co-added dithered exposures (2 co-adds, 2 jitter points, and $2 \times 2$ microsteps).

The Canada France Hawaii Telescope (CFHT), also on Mauna Kea, serendipitously observed the event during the CFHT-*K2*C9 Microlensing Survey. The CFHT operated a multi-color survey of the *K2*C9 superstamp using the Megacam Instrument (Boulade et al. 2003). The CFHT observations for the event were conducted through the $g$-, $r$- and $i$-band filters.

The VLT Survey Telescope (VST) is a 2.61m telescope installed at ESO's Paranal Observatory, and it carried out *K2*C9 observations as a 99-h filler program (Arnaboldi et al. 1998, Kuijken et al. 2002). Observations for such a filler program could only be carried out whenever the seeing was worse than 1 arcsec or conditions were non-photometric. The main objective of the microlensing program was to monitor the *K2*C9 superstamp in an automatized mode to improve the event coverage and to secure color-information in SDSS $r$ and Johnson $V$ passbands. Due to weather conditions, Johnson $V$ images were only taken in the second half of the *K2*C9 survey, and therefore MOA-2016-BLG-227 is only covered by SDSS $r$. The exact pointing strategy was adjusted to cover the superstamp with 6 pointings and to contain as many microlensing events from earlier seasons as possible. In addition, a two-point dither was obtained to reduce the impact of bad pixels and detector gaps. Consequently, some events, like MOA-2016-BLG-227, received more coverage and have been observed with different CCDs.

Figure 4.1 shows the observed MOA-2016-BLG-227 light curve. MOA announced the detection of a light curve anomaly for this event on 9 May 2016 (HJD$'$ = HJD $-2450000 \sim 7518$), and identified the anomaly as a planetary signal 4.5 h after the anomaly alert. Although MOA detected a strong planetary caustic exit, the observing conditions were poor at the MOA observing site both immediately before and after this strong light curve feature. Fortunately, the additional observations from the Wise, UKIRT, CFHT and VST telescopes covered the other important features of the light curve.

## 4.3 Data Reduction

Photometry of the MOA, Wise and UKIRT data were conducted using the offline difference image analysis pipeline of Bond et al. (2017) in which stellar images are measured using an analytical PSF model of the form used in the DoPHOT photometry code (Schechter, Mateo, & Saha 1993).

Differential flux light curves of the CFHT data were produced from Elixir

Table 4.1: Data and parameters for the modeling.

| Dataset | Number of data | $k$ | $e_{\min}$ | $u_\lambda$ |
|---|---|---|---|---|
| MOA-Red[a] | 1804 | 0.938 | 0 | 0.5585 |
| MOA $V$ | 60 | 1.224 | 0 | 0.6822 |
| Wise Astrodon[b] | 44 | 1.267 | 0 | 0.6015[b] |
| UKIRT $H$ | 127 | 1.072 | 0.015 | 0.3170 |
| CFHT $i$ | 77 | 1.673[c] | 0.003 | 0.5360 |
| CFHT $r$ | 77 | 3.028[c] | 0 | 0.6257 |
| CFHT $g$ | 78 | 2.105[c] | 0 | 0.7565 |
| VST-71 $r$[d] | 193 | 1.018 | 0 | 0.6257 |
| VST-95 $r$[d] | 97 | 1.080 | 0 | 0.6257 |

**Notes.** Parameters $k$ and $e_{\min}$ are used for the error normalization, and $u_\lambda$ is the limb darkening coefficient.

[a] Approximately Cousins $R + I$.

[b] This filter blocks $\lambda < 500\,\mathrm{nm}$, and we use the limb darkening coefficient $u_R$ to describe limb darkening in this filter.

[c] The CFHT error estimates were underestimated by a constant factor of 1.54, resulting in larger values of the $k$ parameters.

[d] These use the same SDSS $r$ filter, but different detectors, numbers 71 and 95, respectively.

calibrated images[1] using a custom difference imaging analysis pipeline based on ISIS version 2.2 (Alard & Lupton 1998, Alard 2000) and utilizing an improved interpolation routine[2] (Siverd et al. 2012, Bertin & Arnouts 1996). Further details of the CFHT data reduction will be presented in a future paper.

Since there is no public VST instrument pipeline, calibration images from ESO's archive were used and combined. Restrictive bad pixel masks were extracted to prevent inclusion of flatfield pixels with $> 1\,\%$ nightly variation or with $> 10\,\%$ deviation from the average. The calibrated images were reduced with the difference imaging package DanDIA (Bramich 2008), which uses a numerical kernel for difference imaging and the routines from the RoboNet pipeline for photometry(Tsapras et al. 2009).

It is known that error bars estimated by crowded field photometry codes can be under or overestimated depending on the specific details of event. The error bars provided by the photometry codes are sufficient to find the best fit models, but they do not allow a proper determination of the microlensing light curve model

[1] http://www.cfht.hawaii.edu/Instruments/Elixir/

[2] http://verdis.phy.vanderbilt.edu/

parameter uncertainties. Therefore, we empirically normalize the error bars for each data set. We used the formula presented in Yee et al. (2012) for normalization, $\sigma_i' = k\sqrt{\sigma_i^2 + e_{\rm min}^2}$ where $\sigma_i$ is the original error of the $i$th data point in magnitudes, and the parameters for normalization are $k$ and $e_{\rm min}$. The parameters $k$ and $e_{\rm min}$ are adjusted so that the cumulative $\chi^2$ distribution as a function of the number of data points sorted by each magnification of the preliminary best-fit model is a straight line of slope 1.

The dataset used for our analysis and the obtained normalization parameters are summarized in Table 4.1.

## 4.4 Modeling

The modeling of a binary-lens event requires following parameters: the time of the source closest approach to the lens center of mass, $t_0$, the impact parameter, $u_0$, of the source trajectory with respect to the center of mass of the lens system, the Einstein radius crossing time $t_{\rm E} = \theta_{\rm E}/\mu_{\rm rel}$, the lens mass ratio, $q \equiv M_{\rm p}/M_{\rm host}$ the separation of the lens masses, $s$, the angle between the trajectory and the binary lens axis, $\alpha$, and the source size $\rho \equiv \theta_*/\theta_{\rm E}$. The parameters $u_0$, $s$, and $\rho$ are given in units of the Einstein radius, and $M_{\rm host}$ and $M_{\rm p}$ are the masses of the host star and its planetary companion. With these seven parameters, we can calculate the magnification as a function of time $A(t)$. In the crowded stellar fields where most microlensing events are found, most source stars are blended with one or more other stars, so that we cannot determine the source star brightness directly from images where the source is not magnified. Therefore, we add another set of linear parameters for each data set, the source and blend fluxes, $f_S$ and $f_b$, which are related to the observed flux by $F(t) = f_S A(t) + f_b$.

When we include the finite source effect, we must consider limb darkening effects. We adopt a linear limb-darkening law with one parameter, $u_\lambda$, for each data set. From the intrinsic source color, discussed in Section 4.5.1, we choose the atmospheric parameters for stars with similar intrinsic color from Bensby et al. (2013). This yields an effective temperature of $T_{\rm eff} \sim 5500$ K, a surface gravity of $\log\ [g/({\rm cm\ s^{-2}})] = 4.0$, a metallicity of [M/H] = 0.0, and a microturbulence velocity of $\xi = 1.0$ km s$^{-1}$. We select the limb-darkening coefficients from the ATLAS model by Claret & Bloemen (2011) using these atmospheric parameters. We have $u_{\rm MOA-Red} = 0.5585$ for MOA-Red, $u_V = 0.6822$ for MOA-$V$, $u_R = 0.6015$ for Wise Astrodon, $u_H = 0.3170$ for UKIRT $H$, $u_i = 0.5360$ for CFHT $i$, $u_r = 0.6257$ for CFHT $r$, VST-71 $r$ and VST-95 $r$, and $u_g = 0.7565$ for CFHT $g$. We used the mean of the $u_I$ and $u_R$ values for the limb-darkening coefficients for the MOA-Red passband. Here we adopted the $R$-band limb-darkening coefficient for the Wise Astrodon data. As the Wise Astrodon filter is non-standard, our

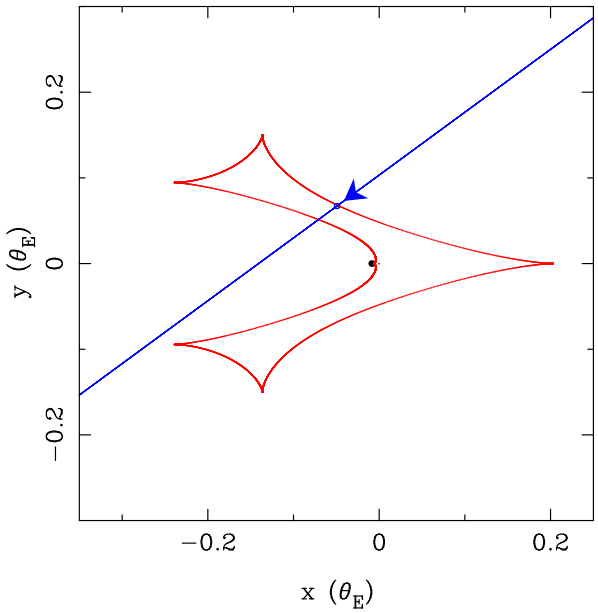


Figure 4.2: Caustic curve for the best-fit model. The blue arrowed line indicates the source trajectory and the tiny blue circle on the caustic entry indicates the source size.

choice is not perfect. However, we note that even if we adopt $u = 0$ for the limb darkening coefficient used with the Wise data, our $\chi^2$ value changes by only 1.5. The limb-darkening coefficients are also listed in Table 4.1.

To find the best-fit model, we conduct a global grid search using the method of Sumi et al. (2016) where we fit the light curves using the Metropolis algorithm (Metropolis et al. 1953), with magnification calculations from the image centered ray-shooting method (Bennett & Rhie 1996, Bennett 2010). From this, we find a unique model in which the source crosses the resonant caustic. We show the model light curve in Figure 4.1, the caustic and the source trajectory in Figure 4.2 and the best-fit model parameters in Table 4.2 along with the parameter error bars, which are calculated with a Markov Chain Monte Carlo (MCMC) (Verde et al. 2003).

We also model the light curve including the microlensing parallax effect due to the Earth's orbital motion (Gould 1992, Alcock et al. 1995) although this event is unlikely to reveal a significant microlensing parallax signal because of its relatively short timescale. We find that the inclusion of the parallax effect improves the fit by $\Delta\chi^2 \sim 14$. However, the parts of the light curve which contribute to this decrease in $\chi^2$ have a scatter similar to the variability of the MOA baseline data, and the best fit microlensing parallax parameter is abnormally large, $\pi_E = 1.3^{+2.1}_{-0.3}$, yielding a very small lens mass of $M_L \sim 0.02 M_\odot$. Therefore, we conclude that

Table 4.2: Parameters for the best-fit binary lens model.

| Parameter | Unit | Value |
|---|---|---|
| $t_0$ | HJD - 2450000 | $7517.5078^{+0.007}_{-0.006}$ |
| $t_E$ | days | $17.03^{+0.08}_{-0.20}$ |
| $u_0$ | $10^{-2}$ | $-8.33^{+0.08}_{-0.16}$ |
| $q$ | $10^{-3}$ | $9.28^{+0.20}_{-0.11}$ |
| $s$ | | $0.9312^{+0.0004}_{-0.0009}$ |
| $\alpha$ | rad | $2.509^{+0.003}_{-0.004}$ |
| $\rho$ | $10^{-3}$ | $3.01^{+0.09}_{-0.05}$ |
| $\chi^2$ | | 2538.9 |
| dof | | 2538 |

**Notes.** Superscripts and subscript indicates the 84th and 16th percentile from the best-fit values, respectively.

the improvement of the fit by the parallax effect is due to systematic errors in the MOA baseline data.

## 4.5 Angular Einstein Radius

Because we have measured the finite source size, $\rho$, to a precision of $\sim 2\,\%$, the determination of the angular source star radius $\theta_*$ will yield the angular Einstein radius $\theta_E = \theta_*/\rho$. This, in turn, provides the mass–distance relation, (Bennett 2008, Gaudi 2012)

$$M_L = \frac{c^2}{4G}\theta_E^2 \frac{D_S D_L}{D_S - D_L} = 0.9823\,M_\odot \left(\frac{\theta_E}{1\,\mathrm{mas}}\right)^2 \left(\frac{x}{1-x}\right)\left(\frac{D_S}{8\,\mathrm{kpc}}\right)\,, \qquad (4.3)$$

where $x = D_L/D_S$. We can empirically derive $\theta_*$ from the intrinsic source magnitude and the color (Kervella et al. 2004, Boyajian et al. 2014).

### 4.5.1 Calibration

Our first step is to calibrate the source magnitude to a standard photometric system. We cross referenced stars in the event field between our DoPHOT photometry catalog of stars in the MOA image and the OGLE-III catalog (Szymański et al.

Table 4.3: Source and RGC magnitude and colors.

| | $I$ | $V-I$ | $V-H$ | $I-H$ |
|---|---|---|---|---|
| RGC (measured from CMD) | $15.33 \pm 0.05$ | $1.88 \pm 0.02$ | $4.03 \pm 0.06$ | $2.11 \pm 0.03$ |
| RGC (intrinsic) | $14.36 \pm 0.05$ | $1.06 \pm 0.03$ | $2.36 \pm 0.09$ | $1.30 \pm 0.06$ |
| Source (measured from light curve) | $19.54 \pm 0.02$ | $1.60 \pm 0.03$ | $3.33 \pm 0.03$ | $1.73 \pm 0.02$ |
| Source (intrinsic) [a] | $18.54 \pm 0.09$ | $0.78 \pm 0.06$ | $1.70 \pm 0.11$ | $0.92 \pm 0.08$ |

[a] Extinction corrected magnitudes using the Nishiyama et al. (2008) extinction model from Table C.1

2011) to convert MOA-Red and MOA $V$ into standard magnitudes. Following the procedure presented in Bond et al. (2017), we find the relations

$$I_{\rm OGLE-III} - R_{\rm MOA} = (28.186 \pm 0.006) - (0.247 \pm 0.005)(V-R)_{\rm MOA} \quad (4.4)$$

$$V_{\rm OGLE-III} - V_{\rm MOA} = (28.391 \pm 0.004) - (0.123 \pm 0.004)(V-R)_{\rm MOA}. \quad (4.5)$$

Using these calibration formulae and the result of light curve modeling, we obtain the source star magnitude $I_S = 19.536 \pm 0.019$ and the color $(V-I)_S = 1.60 \pm 0.03$.

We follow a similar procedure to cross referenced stars in our DoPHOT photometry catalog of stars in the UKIRT images to stars in the VVV (Minniti et al. 2010) catalog which is calibrated to the Two Micron All Sky Survey (2MASS) photometric system (Carpenter 2001), thereby obtaining the relationship between these photometric systems. We use this same VVV catalog to plot CMDs in the next section and for the analysis of the Keck images in Section 4.6. Using the UKIRT $H$-band source magnitude obtained from the light curve model and the calibration relation, we find $H_S = 17.806 \pm 0.017$. We also measure the colors of the source star: $(V-H)_S = 3.33 \pm 0.03$ and $(I-H)_S = 1.730 \pm 0.017$.

### 4.5.2 Extinction and the angular Einstein radius

Next, we correct for extinction following the standard procedure (Yoo et al. 2004, Bennett et al. 2010) using the centroid of red giant clump (RGC) in the CMD as a standard candle.

#### RGC centroid measurement

Figure 4.3 shows the $(V-I,I)$ and $(V-H,H)$ CMDs for stars within 2 arcmin of the source star. The $V$ and $I$ magnitudes are taken from the OGLE-III photometry catalog (Szymański et al. 2011), and the VVV (Minniti et al. 2010) catalog to the

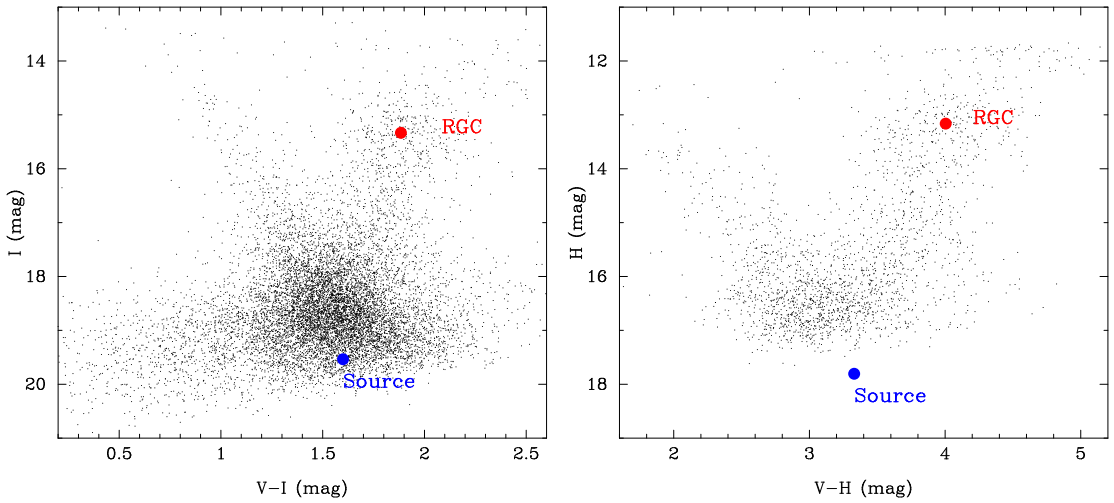


Figure 4.3: Color magnitude diagrams (CMDs) of stars within 2′ of the source star. The left panel shows $V-I$ vs $I$ for the stars in OGLE-III catalog (Szymański et al. 2011), and the right panel shows $V-H$ vs $H$ using stars from the OGLE-III catalog to the VVV catalog, which is calibrated to the 2MASS magnitude scale. The source star and the mean of red giant clump are shown as the blue and red dots, respectively.

2MASS photometry scale for $H$-band magnitudes. To plot the $V-H$ vs $H$ CMD, we cross referenced stars in the VVV catalog to stars in the OGLE-III catalog. For this cross reference, we use only isolated stars that are cross-matched to within 1 arcsec of stars in the OGLE-III catalog to ensure one-to-one matching between the two catalogs. We note that the 1-arcsec limits corresponds to the average seeing in the VVV images. We find the centroids of RGC in the $(V-I, I)$ and $(V-H, H)$ CMDs are $I_{\rm cl} = 15.33 \pm 0.05$, $(V-I)_{\rm cl} = 1.88 \pm 0.02$, $(V-H)_{\rm cl} = 4.03 \pm 0.06$ and $(I-H)_{\rm cl} = 2.11 \pm 0.03$.

### RGC intrinsic magnitude and color

We use $(V-I)_{\rm cl,0} = 1.06 \pm 0.03$ and $I_{\rm cl,0} = 14.36 \pm 0.05$ for the intrinsic $V-I$ color and $I$ magnitude of the RGC (Bensby et al. 2013, Nataf et al. 2016) at the Galactic longitude of this event. Following Nataf et al. (2016), we calculate the intrinsic color of $V-H$ and $I-H$ in the photometric system we are using now (i.e., Johnson $V$, Cousins $I$ and 2MASS $H$) by the tool provided by Casagrande & VandenBerg (2014) which is based on a grid of MARCS model atmospheres (Gustafsson et al. 2008). Assuming the stellar atmospheric parameters [Fe/H] $= -0.07 \pm 0.10$ (Gonzalez et al. 2013), log $g = 2.3 \pm 0.1$ and $[\alpha/{\rm Fe}] = 0.20 \pm 0.05$

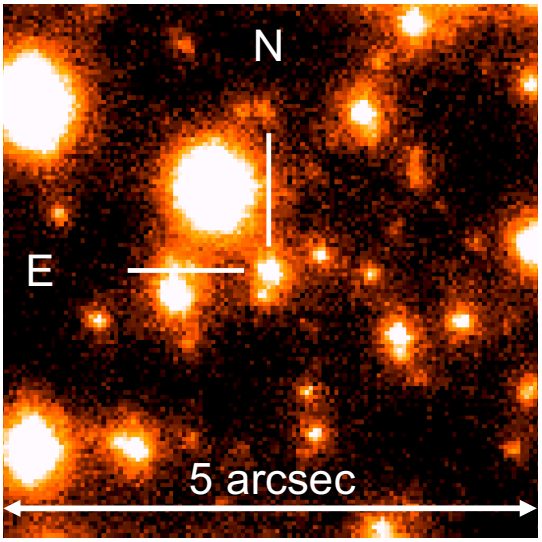


Figure 4.4: Co-added Keck II AO image of the event field. The target is indicated.

(Hill et al. 2011, Johnson et al. 2014) for the RGC in the event field, we derive $(V-H)_{\rm cl,0} = 2.36 \pm 0.09$ and $(I-H)_{\rm cl,0} = 1.30 \pm 0.06$ by adjusting the last atmospheric parameter $T_{\rm eff}$ so that the $(V-I)$ value is in the range of $1.03 < (V-I) < 1.09$. We summarize the magnitude and colors for the RGC centroid and the source in Table 4.3.

### Angular Einstein radius

By subtracting the intrinsic RGC color and magnitude values from the measured RGC positions in our CMDs, we find an extinction values of $A_{I,\rm obs} = 0.98 \pm 0.07$, and color excess values of $E(V-I)_{\rm obs} = 0.82 \pm 0.04$, $E(V-H)_{\rm obs} = 1.67 \pm 0.11$ and $E(I-H)_{\rm obs} = 0.81 \pm 0.07$. Following the method of Bennett et al. (2010), we fit these values to the extinction laws of Cardelli et al. (1989), Nishiyama et al. (2009) and Nishiyama et al. (2008) separately and compared the results. We present this analysis in Appendix C. From this comparison of models, we choose the Nishiyama et al. (2008) extinction law, which yields an H-band extinction of $A_H = 0.19 \pm 0.02$ and a source angular radius of $\theta_* = 0.68 \pm 0.02$ $\mu$as. This $\theta_*$ value implies an angular Einstein radius of $\theta_E = \theta_*/\rho = 0.227^{+0.006}_{-0.009}$ mas and a lens-source relative proper motion of $\mu_{\rm rel} = \theta_E/t_E = 4.88^{+0.14}_{-0.17}$ mas/yr.

## 4.6 Excess Flux from Keck AO Images

On August 13, 2016 (HJD′ = 7613.85) we observed MOA-2016-BLG-227 using the NIRC2 camera and the laser guide star (LGS) adaptive optics (AO) system mounted on the Keck II telescope at Mauna Kea, Hawaii. Observations were conducted in the $H$-band using the wide-field camera (0.04"/pix). We took four dithered frames with 5 sec exposures and three additional dithered frames with a total integration time of 90 sec (6 co-adds of 15 sec exposures). The first set of these images allows photometric calibration using unsaturated bright stars, and the second set provides the increased photometric sensitivity to provide a high signal-to-noise flux measurement of the target. Standard dark and flat field corrections were applied to the images, and sky subtraction was done using a stacked image from a nearby empty field. Each set of images was then astrometrically aligned and stacked. Finally, we use SExtractor (Bertin & Arnouts 1996) to extract the Keck source catalog from the stacked images.

A calibration catalog was extracted using an $H$-band image of the target area taken by the VISTA Variables in the Via Lactea survey (VVV; Minniti et al. 2010) reprocessed following the approach described in Beaulieu et al. (2016). We apply a zero-point correction for the Keck source catalog using common VVV and Keck sources. The estimated zero-point uncertainty is 0.05. Figure 4.4 shows the Keck II AO image of the field. It indicates a bright star close to the target. As a result, the dominant photometry error comes from the background flux in the wings of the PSF of the nearby star.

We determine the source coordinates from a MOA difference image of the event while it was highly magnified. We then identify the position of the microlensing target (source+lens) on the Keck image (see Figure 4.4). The measured brightness of the target is $H_{\rm Keck} = 17.63 \pm 0.06$. Due to technical problems in the AO system, the stellar images display sparse halo around each object. Thus, the FWHM of the Keck image is $0.184''$ (measured as the average of isolated bright stars near the target). This sets a limit on our ability to exclude flux contribution from stars unrelated to the source and the lens, as we discuss below.

The light curve analysis of the UKIRT data $H$-band data implies an (extinction uncorrected) $H$-band source magnitude of $H_S = 17.806 \pm 0.017$ (see Section 4.5.1). Because the Keck observations were taken after the event reached its baseline brightness ($t_{\rm obs,Keck} - t_0 = 5.7\ t_E$), we can extract the excess flux by subtracting the source flux from the target flux. That is, $H_{\rm ex,obs} = H_S - 2.5\log(F_{\rm Keck}/F_S - 1) = 19.7 \pm 0.4$, where $F_{\rm Keck}/F_S = 10^{-0.4(H_{\rm Keck} - H_S)}$.

Table 4.4: Assumptions and undetectable limits used for the prior probability distributions

| Priors of | Assumption | Closer limit | Wider limit | Used observed values |
|---|---|---|---|---|
| $H_L$ | Galactic model | – | – | $t_{\rm E}$, $\theta_{\rm E}$ |
| $H_{\rm amb}$ | Luminosity function | – | 0.8 FWHM | FWHM, Number density |
| $H_{SC}$ | Binary distribution [a] | $\theta_E/4$ | 0.8 FWHM | FWHM, $\theta_E$, $H_S$ |
| $H_{LC}$ | Binary distribution [a] | $w_{LC}$[b]$< u_0$ | 0.8 FWHM | FWHM, $\theta_E$, $u_0$, $M_L$[c] |

[a] The binary distribution used by Koshimoto et al. (2018, in preparation), based on Duchêne & Kraus (2013).
[b] The caustic size created by the hypothetical companion to the lens, $w_{LC} = 4q_{LC}/(s_{LC} - s_{LC}^{-1})^2$.
[c] The $M_L$ value extracted from the prior probability distributions to calculate the $H_L$ value.

## 4.7 Lens Properties through Bayesian Analysis

Koshimoto et al. (2018, in preparation)present a systematic Bayesian analysis for the identification of the star or stars producing excess flux at the position of the source seen in high-angular resolution images. This analysis gives us the posterior probability distributions for the lens mass and the distance by combining the results of the light curve modeling and the measured excess flux value. The method is summarized as follows.

1. Determine prior probability distributions for four possibilities for the origin of the excess flux: the lens star, unrelated ambient stars, source companions or lens companions. We denote these fluxes by $F_L$, $F_{\rm amb}$, $F_{SC}$ and $F_{LC}$, respectively.

2. Determine all combinations of the flux values for each type of star in the prior distribution that are consistent with the observed excess flux, $F_{\rm excess} = F_L + F_{\rm amb} + F_{SC} + F_{LC}$.

The extracted combinations at step 2 corresponds to the posterior probability distributions for the MOA-2016-BLG-227 event.

### 4.7.1 Prior probability distributions

Now, we must determine the prior probability distributions of the four types of stars that can contribute to the excess flux at the position of the source. We use all the information we have about this event — except for the value of excess flux — to create our prior probability distributions. This means that we include the

FWHM of the Keck images, but not the measured magnitude of the object at the location of the microlensing event. Table 4.4 shows a summary of our assumptions.

### Lens flux prior

For the lens flux prior distribution, we conduct a Bayesian analysis using the observed $t_E$ and $\theta_E$ values and the Galactic model, which has been used in a number of previous papers (Alcock et al. 1995, Beaulieu et al. 2006) to estimate lens properties for events with no microlensing parallax signal. We use the Galactic model of Han & Gould (1995) for the density and the velocity models and use the mass function presented in the Supplementary Information section of Sumi et al. (2011). Using this result and the mass-luminosity relation presented in Koshimoto et al. (2018, in preparation), we obtain the prior distribution for the lens apparent magnitude, $H_L$. We adopt the formula for the extinction to the lens, $A_{H,L} = (1 - e^{-D_L/h_{\rm dust}})/(1 - e^{-D_S/h_{\rm dust}})\ A_{H,S}$, following Bennett et al. (2015), where $h_{\rm dust} = (0.1\ {\rm kpc})/\sin|b|$ is the scale length of the dust toward the Galactic bulge, assuming a scale height of 0.1 kpc. Note that this Bayesian analysis gives us prior distributions for $M_L$, $D_L$ and $D_S$, in addition to the $H_L$ prior distribution, but based on the observed $t_E$ and $\theta_E$ values. These values are needed for the calculation of the probability distributions below.

### Ambient star flux prior

In order to determine the prior probability distribution for the flux of any unrelated ambient stars, we determine the number density of stars in Keck AO images, centered on the target, within a magnitude range selected to have high completeness and divide that number by the area of the image. Then we use the luminosity function of Zoccali et al. (2003) to derive the number density of stars as a function of $H$ magnitude, normalized to this measured number density in the Keck AO image. In this calculation, we correct for the differences in extinction and distance moduli between our field and that of Zoccali et al. (2003), using the distance moduli from Table 3 of Nataf et al. (2013) and extinction values for both fields.

When correcting for the extinction difference, we also consider the difference between the extinction laws used. Zoccali et al. (2003) derived an $A_H$ value using the C89 extinction law with $R_V = 3.1$, whereas our preferred N08 extinction law implies a significantly different $A_H$ value. To correct for this difference, we calculate the $A_H$ value towards their field using the N08 extinction law fit to the RGC centroid in the OGLE-III CMD and the $R_{JKVI}$ value from Table 3 of Nataf et al. (2013) for their field. The $A_H$ value we derived here is $A_H = 0.122$, which is different from the value of $A_H = 0.265$ used by Zoccali et al. (2003). Therefore, we convert their extinction corrected $H$-band luminosity function to a luminosity func-

tion with our preferred extinction model by adding $\Delta A_H = 0.265 - 0.122 = 0.142$ to their extinction corrected magnitudes, and then add the extinction appropriate for our field, $A_H = 0.19$.

We assume that stars can be resolved only if they are separated from the source by $\geq 0.8\,\mathrm{FWHM} = 148\,\mathrm{mas}$. Under this assumption, the expected number of ambient stars within the circle is derived by multiplying the area of this unresolvable region by the total number density derived above. We determine the number of stars following the Poisson distribution with the mean value of the expected number of stars. We use the corrected luminosity function to determine the magnitude of each star.

**Source and lens companion flux priors**

We calculate the source and lens companion flux priors with the stellar binary distribution described in Koshimoto et al. (2018, in preparation). The binary distribution is based on the summary in a review paper (Duchêne & Kraus 2013), which provides distributions of the stellar multiplicity fraction, and mass ratio and semi-major axis distributions.

For the flux of source companions, we calculate the source mass $M_{SC} = q_{SC} M_S$ and then convert that into a source companion magnitude, $H_{SC}$, using a mass-luminosity relation. The mass ratio $q_{SC}$ is derived from the binary distribution. We derive the source mass, $M_S$, from the combination of $H_S$, $D_S$ and using the mass-luminosity relation. Similarly, we calculate the lens companion' s magnitude, $H_{LC}$, from $M_{LC} = q_{LC} M_L$, where the lens mass $M_L$ comes from the same distribution that was used to obtain the lens flux probability distribution.

We consider companions to the lens or source located in the same unresolvable regions in the vicinity of the source, just as in the case of ambient stars. Stellar companions have a separation distribution that is much closer to logarithmic than the uniform distribution expected for ambient stars. As a result, we must now exclude companions that are too close to the source and lens as well as companions that are so widely separated that they will be resolved. Companions that are too close to the source could be magnified themselves, and companions that are too close to the lens could serve as an additional lens star. Such a constraint would have no effect on the ambient star probability, because the probability of an ambient star very close to the source or lens is much smaller than that of a stellar companion. Following Batista et al. (2014), we adopt $\theta_E/4$ as the close limit for source companions and $w_{LC} < u_0$ as the close limit for lens companions, where $w_{LC} = 4q_{LC}/(s_{LC} - s_{LC}^{-1})^2$ (Chung et al. 2005) and $q_{LC}$ and $s_{LC}$ and are the stellar binary lens mass ratio and separation, respectively. We take 0.8 FWHM as the maximum unresolvable radius.

We also consider triple and quadruple systems when estimating the effect of

companions to the source and lens, following Koshimoto et al. (2018, in preparation), but we find no significant difference from the case of only considering binary systems. We therefore do not include triple and quadruple systems in this analysis, for simplicity.

**Excess flux prior**

Figure 4.5 shows the prior probability distributions we derived following the procedure described above to calculate flux of each type of stars. In addition to the magnitude of the four types of stars that might contribute to the excess flux, we show the prior distributions for the total excess flux, $H_{\rm excess}$, the lens mass, $M_L$, and the distance to the lens $D_L$. Some of the panels in this figure have total probabilities $P_{\rm total} < 1$. This is because many stars do not have binary companions and there is a large probability of no measurable flux from an ambient star. The $H_{\rm excess}$ prior indicates a high probability at the observed magnitude of $H_{\rm ex,obs} = 19.7 \pm 0.4$. The three panels for individual stars, $H_L$, $H_{\rm amb}$ and $H_{SC}$ show similar probabilities at the observed excess flux value. This indicates that it will be difficult to claim that all of the excess comes from the lens itself.

### 4.7.2 Posterior probability distributions

We generate the posterior probability distributions shown in Figure 4.6 by extracting combinations of parameters which have values of $H_{\rm excess}$ consistent with the measured value of $H_{\rm ex,obs} = 19.7 \pm 0.4$ using a Gaussian distribution in fluxes (not magnitudes). The probability that $H_L \leq 20$ is almost same as the probability for $H_{\rm SC} \leq 20$ and slightly higher, but competitive with the probability that $H_{\rm amb} \leq 20$, which results in very loose constraints on $H_L$ and $M_L$. This result is consistent with our expectation as discussed in Section 4.7.1.

The third to sixth columns of Table 4.5 shows the median, the 1 $\sigma$ error bars, and the 2 $\sigma$ range for $H_L$, $M_L$ and $D_L$ for both the prior and posterior distributions. This same table also shows the values of the planet mass $M_{\rm p}$, the projected separation $a_\perp$ and the three-dimensional star-planet separation $a_{3d}$ calculated from the probability distributions, where $a_{3d}$ is statistically estimated assuming a uniform orientation for the detected planets. In the bottom three rows, we present the probabilities that the fraction of the excess flux due to the lens, $f_L$ is larger than 0.1, 0.5 and 0.9, which correspond to magnitude difference between the lens and the total flux excess of 2.5 mag, 0.75 mag and 0.11 mag, respectively.

The posterior distributions for the lens system properties are remarkably similar to the prior distributions. When we compare the $1\sigma$ ranges of the prior and posterior distributions, we see that the lens system is most likely to be composed an M or K dwarf star host and a gas-giant planet. However, the prior and posterior

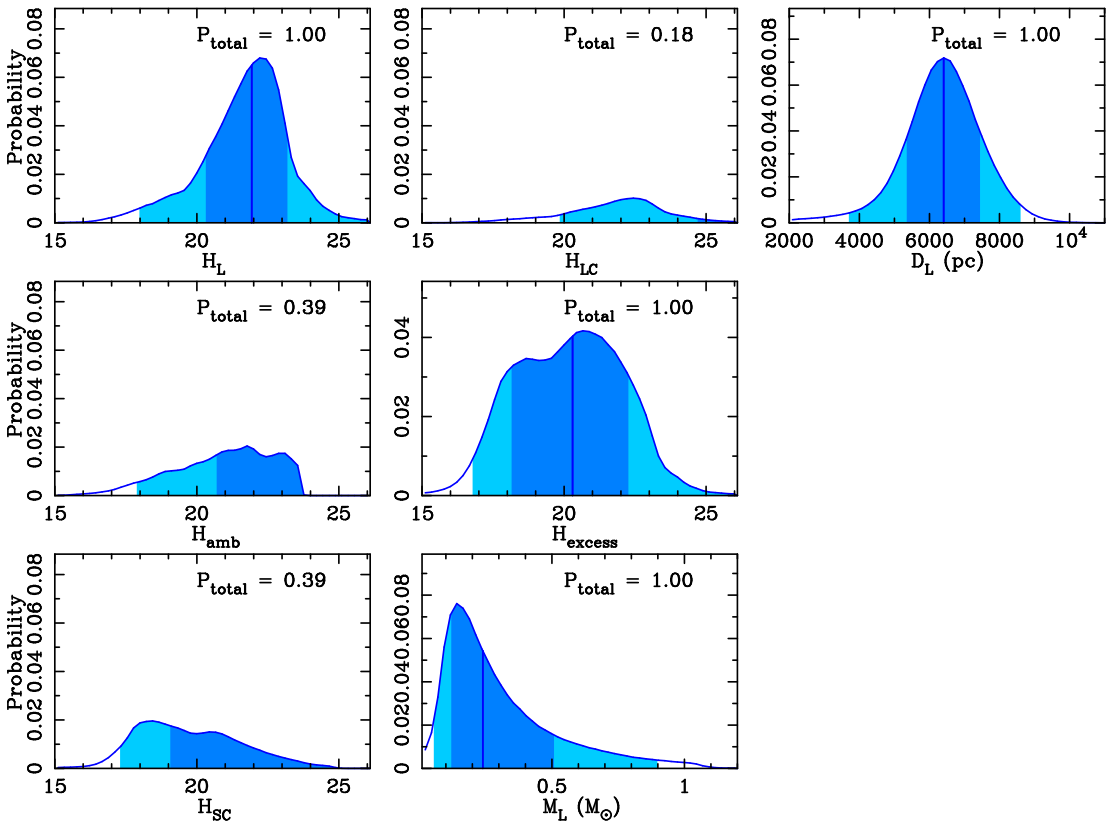


Figure 4.5: Prior probability distributions using the assumptions in Table 4.4 and light curve model constraints, as well as the seeing of the Keck AO image, but not the target flux. We assume that the planet hosting probability does not depend on the stellar mass. The borders between dark and light shaded regions indicate the $1\sigma$ limits and the borders between light shaded and white regions indicate $2\sigma$ limits. The $P_{\rm total}$ value in each panel is the probability that the object exists. The panels with $P_{\rm total} < 1$ indicate the probability that the companion or ambient star actually exists, and some of these do not have the borders of the $1\sigma/2\sigma$ limit within the plotted region.

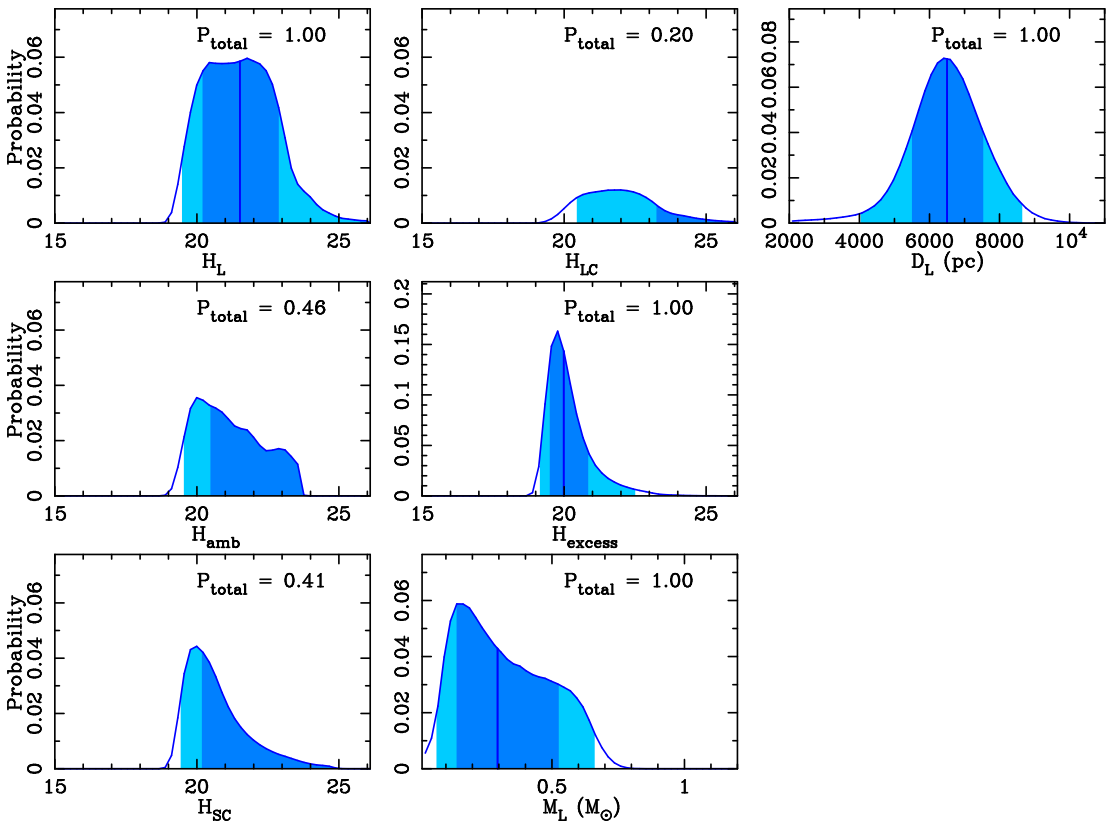


Figure 4.6: Posterior probability distributions generated by extracting combinations which have consistent excess flux values with $H_{\rm ex,obs} = 19.7 \pm 0.4$ (in flux unit) from the prior probability distributions in Figure 4.5.

distributions differ from each other when we consider the $2\sigma$ ranges and the tails of the distributions. The possibility of a G dwarf host star is ruled out by the posterior distribution while the host star can be a G dwarf according to the prior distribution. This implies that the host star is likely to be an M or K dwarf.

Table 4.5: Lens properties calculated from the prior and posterior probability distributions.

| Parameters | Unit | Prior $\alpha = 0$ | $2\sigma$ range | Posterior $\alpha = 0$ | $2\sigma$ range | Posterior $\alpha = 1$ | Posterior $\alpha = 2$ | Posterior $\alpha = 3$ |
|---|---|---|---|---|---|---|---|---|
| $H_L$ | mag | $21.9^{+1.3}_{-1.6}$ | 18.0-28.7 | $21.5^{+1.4}_{-1.3}$ | 19.5-27.5 | $20.8^{+1.3}_{-0.9}$ | $20.4^{+1.1}_{-0.7}$ | $20.2^{+0.8}_{-0.6}$ |
| $M_L$ | $M_\odot$ | $0.24^{+0.27}_{-0.12}$ | 0.06-0.90 | $0.29^{+0.23}_{-0.15}$ | 0.07-0.66 | $0.42^{+0.17}_{-0.20}$ | $0.50^{+0.13}_{-0.18}$ | $0.54^{+0.10}_{-0.15}$ |
| $M_{\rm p}$ | $M_{\rm Jup}$ | $2.3^{+2.6}_{-1.2}$ | 0.5-8.8 | $2.8^{+2.2}_{-1.5}$ | 0.6-6.4 | $4.1^{+1.7}_{-1.9}$ | $4.8^{+1.2}_{-1.8}$ | $5.3^{+1.0}_{-1.5}$ |
| $D_L$ | kpc | $6.4 \pm 1.0$ | 3.5-8.5 | $6.5 \pm 1.0$ | 3.9-8.6 | $6.8^{+1.0}_{-0.9}$ | $6.9^{+1.0}_{-0.9}$ | $7.1^{+1.0}_{-0.9}$ |
| $a_\perp$ | AU | $1.37 \pm 0.23$ | 0.76-1.84 | $1.39 \pm 0.22$ | 0.84-1.86 | $1.45^{+0.22}_{-0.20}$ | $1.49^{+0.22}_{-0.20}$ | $1.51^{+0.22}_{-0.20}$ |
| $a_{3d}$ | AU | $1.64^{+0.93}_{-0.36}$ | 0.89-6.49 | $1.67^{+0.94}_{-0.35}$ | 0.97-6.62 | $1.74^{+0.99}_{-0.35}$ | $1.79^{+1.02}_{-0.35}$ | $1.82^{+1.03}_{-0.36}$ |
| $P(f_L > 0.1)$[a] | % | 72.2 | - | 78.1 | - | 90.8 | 96.5 | 98.7 |
| $P(f_L > 0.5)$[a] | % | 48.0 | - | 41.4 | - | 56.7 | 69.6 | 78.4 |
| $P(f_L > 0.9)$[a] | % | 33.8 | - | 24.0 | - | 29.9 | 38.0 | 44.5 |

**Notes.** The values of posterior probability distributions are shown also for different $\alpha$ values, the slope of the probability of hosting planets $P_{\rm host} \propto M^\alpha$. The values given in form of the median with the 1 $\sigma$ uncertainty. The 2 $\sigma$ range is given for $\alpha = 0$.

[a] The probabilities that the fraction of the lens flux to the excess flux, $f_L \equiv F_L/F_{\rm excess}$, is larger than the indicated values. The fractions of 0.1, 0.5 and 0.9 correspond to the difference of magnitude, $H_L - H_{\rm excess} = -2.5\ \log(F_L/F_{\rm excess})$, of 2.5 mag, 0.75 mag and 0.11 mag.

### 4.7.3 Comparison of different planetary host priors

One assumption that we have made implicitly is that the properties of the lens star do not depend on the fact that we have detected a planet orbiting the star. This assumption could be false. Perhaps more massive stars are more likely to host planets of the measured mass ratio, or perhaps disk stars are more likely to host planets than bulge stars. The microlensing method can be used to address these questions, but we must be careful not to assume the answer to them.

We have assumed that this detection of the planetary signal does not bias any other property of the lens star, such as its mass or distance. If there was a strong dependence of the planet hosting probability at the measured mass ratio of $9.3^{+0.2}_{-0.1} \times 10^{-3}$, then this implicit prior could lead to incorrect conclusions. Some theoretical papers based on core-accretion (Laughlin et al. 2004, Kennedy & Kenyon 2008) and analyses of exoplanets found by radial velocities (Johnson et al. 2010) have argued that gas giants are less frequently orbiting low-mass stars, however, the difference disappears when the planets are classified by their mass ratio, $q$, instead of their mass. Nevertheless, since the host mass dependence of the planet hosting probability is not well measured, we investigate how our results depend on the choice of this prior.

We consider a series of prior distributions where the planet hosting probability follows a power law of the form $P_{\rm host} \propto M^{\alpha}$, and we conduct a series of Bayesian analyses with $\alpha = 1$, $\alpha = 2$ and $\alpha = 3$ in addition to the calculation with $\alpha = 0$, presented above. Figure 4.7 shows both the prior and posterior probability distributions for the lens mass, $M_L$, with these different values of $\alpha$. The lens property values for each posterior distribution are shown in Table 4.5. The median of expected lens flux approaches the measured excess flux as $\alpha$ increases (i.e., the power law becomes steeper), and consequently the median of the lens mass also increases and the parameter uncertainties decrease. Thus, larger $\alpha$ values imply that more of the excess flux is likely to come from the lens. Nevertheless, our basic conclusion that the host is a M or K-dwarf hosting a gas giant planet remains for all of the $1 \leq \alpha \leq 3$ priors.

## 4.8 Discussion and Conclusion

We have analyzed the planetary microlensing event MOA-2016-BLG-227 which was discovered next to the field observed by the microlensing campaign (Campaign 9) of the *K2* Mission. The event and planetary signal were discovered by the MOA collaboration and a significant portion of the planet signal was covered by the data from the Wise, UKIRT, CFHT and VST surveys, which observed the event as part of the *K2*C9 program. Analysis of these data yields a unique

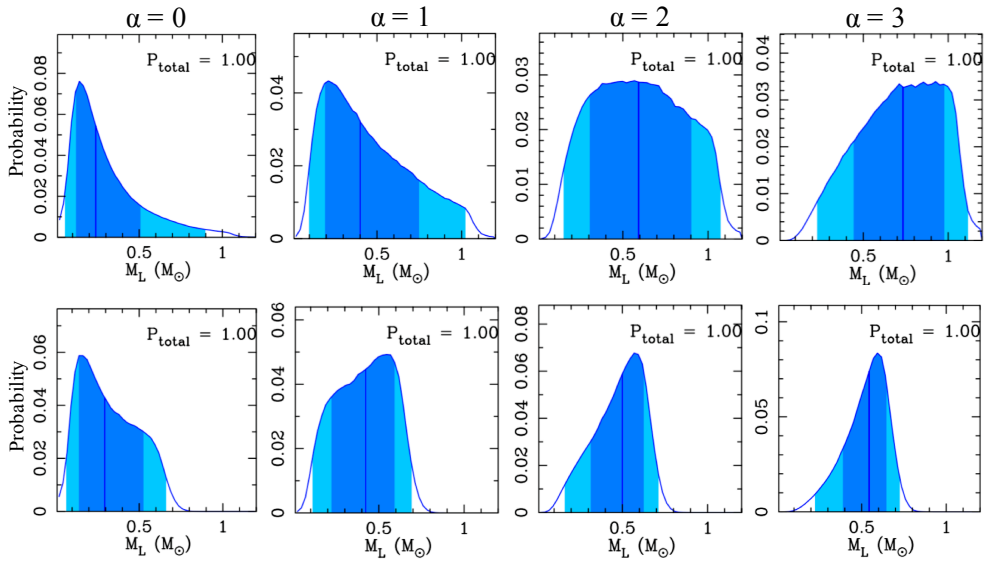


Figure 4.7: Prior (top) and posterior (bottom) probability distributions of the lens mass $M_L$ using different priors for the planet hosting probability, which is assumed to follow a power law, $P_{\rm host} \propto M^{\alpha}$. The $\alpha = 0$ plots are repeated from Figures 4.5 and 4.6.

microlensing light curve solution with a relatively large planetary mass-ratio of $q = 9.28^{+0.20}_{-0.11} \times 10^{-3}$. We considered several different extinction laws and decided that the N08 (Nishiyama et al. 2008) law was the best fit to our data, although our results would not change significantly with a different law. With this extinction law, we derive an angular Einstein radius of $\theta_E = 0.227^{+0.006}_{-0.009}$ mas, which yields the mass–distance relation given in Equation 4.3. We detected excess flux at the location of the source in a Keck AO image, and we performed a Bayesian analysis to estimate the relative probability of different sources of this excess flux, such as the lens, an ambient star, or a companion to the host or source. Our analysis excludes the possibility that the host star is a G-dwarf, leading us to a conclusion that the planet MOA-2016-BLG-227Lb is a super-Jupiter mass planet orbiting an M or K-dwarf star likely located in the Galactic bulge. Such systems are predicted to be rare by the core accretion theory of planet formation. It is also thought that such a planet orbiting a white dwarf host at $a_{3d} \sim 2$ AU is unlikely (Batista et al. 2011).

If the planet frequency does not depend on the host star mass or distance, our Bayesian analysis indicates the system consists of a host star with mass of $M_L = 0.29^{+0.23}_{-0.15} M_\odot$ orbited by a planet with mass of $M_{\rm p} = 2.8^{+2.2}_{-1.5} M_{\rm Jup}$ with a three-dimensional star-planet separation of $a_{3d} = 1.67^{+0.94}_{-0.35}$ AU. The system is located at $D_L = 6.5 \pm 1.0$ kpc from the Sun. We also considered different priors for the planet hosting probability as a function of host star mass. We consider planet hosting prior probabilities that scale as $P_{\rm host} \propto M^\alpha$ with $\alpha = 1, 2, 3$, in addition to the $\alpha = 0$ prior that we use for our main results. As $\alpha$ increases, the median value of the lens mass also increases and the probability for the lens to be responsible for the excess $H$-band flux increases, as well. Johnson et al. (2010) found a linear (i.e., $\alpha = 1$) relationship between host mass and planet occurrence from 0.5 $M_\odot$ to 2.0 $M_\odot$ for giant planets within $\sim$ 2AU around host stars discovered by the radial velocity (RV) method. However, this analysis used a fixed minimum mass instead of a fixed mass ratio, and it does not appear that Johnson et al. (2010) did a detailed calculation of their detection efficiencies. Another result using RV planet data by Montet et al. (2014) gives $\alpha = 0.8^{+1.1}_{-0.9}$, using a sample more similar to the microlensing planets, i.e., gas giants orbiting at $0 < a < 20$ AU around M-dwarf stars. However, our basic conclusion that the MOA-2016-BLG-227L host star is an M or K-dwarf with a gas-giant planet located in the Galactic bulge would not change with a different $\alpha$ value, as indicated in Figure 4.7 and Table 4.5.

The probability that more than 90% of the excess flux seen in the Keck AO images comes from the lens is still 24.0% even assuming $\alpha = 0$. This is significant enough that we cannot ignore the possibility that most of the excess flux comes from the lens star. One approach for obtaining further constraints is to get the color of the excess flux. If the excess flux is not from the lens, the derived lens

mass and distance with $H_{\rm excess}$ may be inconsistent with the value derived using the excess flux in a different pass band, if we assume that all of the excess flux comes from the lens. However, such a measurement could also yield ambiguous results. Another, more definitive, approach is to observe this event in the future when we can expect to detect the lens-source separation through precise PSF modeling with high resolution space-based data (Bennett et al. 2007, 2015) or direct resolution with AO imaging (Batista et al. 2015). The lens-source relative proper motion value of $\mu_{\rm rel} = 4.88^{+0.14}_{-0.17}$ mas/yr indicates that we can expect to be able to resolve the lens, if it provides a large fraction of the excess flux in $\sim 2022$ using *HST* (Bhattacharya et al. 2017) and in 2026 using Keck AO (Batista et al. 2015). Observations by the James Webb Space Telescope (Gardner et al. 2006), the Giant Magellan Telescope (Johns et al. 2012), the Thirty Meter Telescope (Nelson & Sanders 2008) and the Extremely Large Telescope (Gilmozzi & Spyromilio 2007) could detect the lens-source relative proper motion much sooner. If the separation of the excess flux from the source is different from the prediction of the microlensing model in these future high angular resolution observations, it would indicate that the lens is not the main cause of the excess flux, implying a lower mass planetary host star.

# Chapter 5

# Summary and Discussion

In Chapters 3 and 4, the observations and analysis of two planets discovered via the gravitational microlensing method, OGLE-2012-BLG-0950Lb and MOA-2016-BLG-227Lb, were described. In this chapter, these two studies are summarized from two aspects, from the revealed lens property and from the characterization of the lens system. Further discussions are presented in addition to the summary in each section. Particularly, the discussion about how to estimate contamination probabilities in the detected excess flux is one of main points in this thesis, which is not sufficiently discussed in the above sections. In the discussion, the difference between the previous and new methods, used in Chapter 3 and Chapter 4 respectively, and the need for a new method, is discussed.

## 5.1 Revealed Lens Properties

### 5.1.1 OGLE-2012-BLG-0950Lb: An intermediate mass planet beyond the snow line, predicted to be common

In Chapter 3, OGLE-2012-BLG-0950Lb was found to have an intermediate mass of $M_{\rm p} = 35^{+17}_{-9} M_{\oplus}$, which is between masses of Saturn and Neptune, and an orbit at a planet-host projected separation of $r_{\perp} = 2.7^{+0.6}_{-0.7}$ AU around its host star, which itself has a mass of $M_{\rm host} = 0.56^{+0.12}_{-0.16} M_{\odot}$. As shown in Figure 3.7, this is a planet orbiting beyond the snow line, with a mass around the apparent valley in the mass distribution histogram. According to the standard core accretion theory (e.g., Ida & Lin 2004), planets in this mass range are predicted to be common outside the snow line, while they are thought to be rare inside the snow line. In contrast to the prediction, only a few planets orbiting beyond the snow line with an intermediate mass have been discovered, even when including RV planets. However, this kind of comparison is not fair at this stage because the

observed distributions are highly affected by the detection efficiency. Also, some of the plotted masses still have large uncertainties. As for the RV planets, the RV method measures just a lower limit of planet mass because of the unknown orbital inclination. As for the masses of the microlensing planets, about half of them are measured (filled circles in Figure 3.7) by a combination of any two or all the three physical values that provide mass–distance relations shown in Figure 2.13. The other half of them are estimated by Bayesian analysis (open circles in Figure 3.7) that uses a Galactic stellar distribution as the prior probability distribution. OGLE-2012-BLG-0950Lb is the second microlensing planet with a reliable mass measurement found to have an intermediate mass. More observations and reliable mass measurements are needed to conclude whether this kind of planet is common or not.

### 5.1.2 MOA-2016-BLG-227Lb: A massive planet around an M or K-dwarf, predicted to be rare

As described in Chapter 4, MOA-2016-BLG-227Lb was revealed as a super-Jupiter mass planet around an M or K-dwarf star. In contrast to the case of OGLE-2012-BLG-0950, gas giants around late-type stars are predicted to be rare by the standard core accretion theory (Laughlin et al. 2004, Ida & Lin 2005, Kennedy & Kenyon 2008). However, about one third of microlensing planets discovered so far, including MOA-2016-BLG-227Lb, are in such systems (e.g., Gaudi et al. 2008, Dong et al. 2009a,b, Koshimoto et al. 2014), which are indicated in the red shaded region in Figure 5.1. Note that the detection efficiency is higher for massive planets (the dependency is roughly $\propto q^{0.6}$) and that, again, more than half of their masses are estimated by Bayesian analysis (open circles in Figure 5.1), that assumes that the planetary frequency does not depend on their host' s mass. Nevertheless, it is likely that formation processes other than the core accretion scenario, such as the gravitational disk instability scenario (Boss 1997) and the tidal downsizing scenario (Nayakshin 2010), contribute to the microlensing sample in the red shaded region. This is because no planet with a mass ratio larger than $q = 9 \times 10^{-3}$, which is the mass ratio of MOA-2016-BLG-227Lb, forms around a host star less massive than $0.6 M_{\odot}$, according to the result of the planet population synthesis model of core accretion by Ida & Lin (2005), as shown in Figure 5.2. Boss (2006) studied the gravitational disk instability around an M-dwarf and found that massive planets can be formed around it, but at distances $\gtrsim 6$ AU which is beyond most of the discovered microlensing planets' orbit. The tidal downsizing scenario, in which gravitational instability and the effects of migration and tidal force are combined, may explain those microlensing planets, although this is a newly proposed kind of scenario and not many studies have been published.

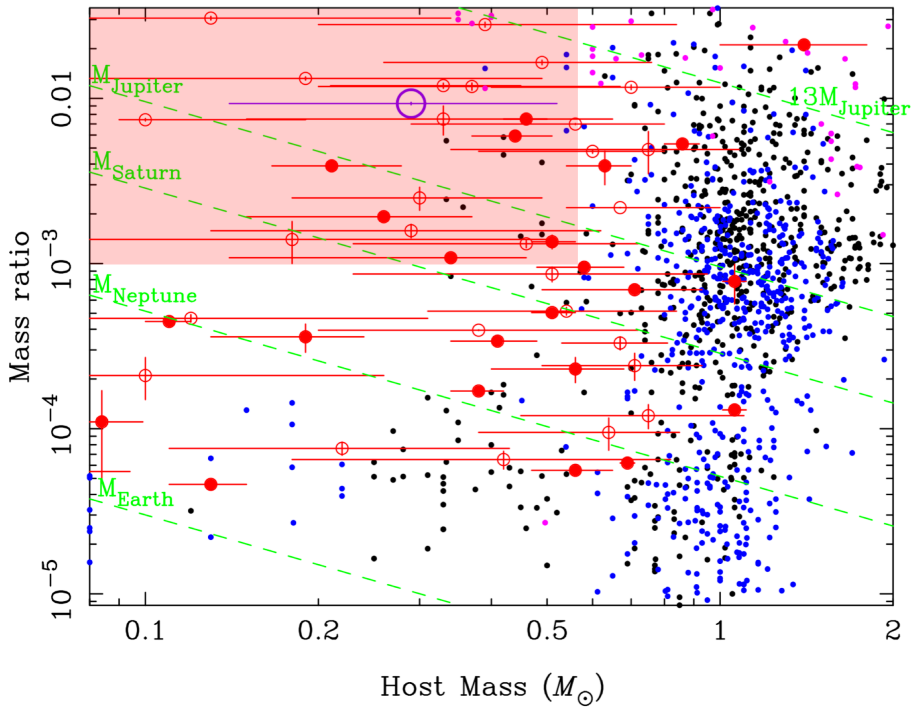


Figure 5.1: Same as Figure 3.7, but distribution of host mass versus mass ratio plane. The red shaded area of the parameter space indicates planets with a mass ratio larger than $10^{-3}$ around M-type host stars with $< 0.55\,M_\odot$. Here $10^{-3}$ is from the mass ratio between the Sun and Jupiter. The purple circle indicates MOA-2016-BLG-227Lb.

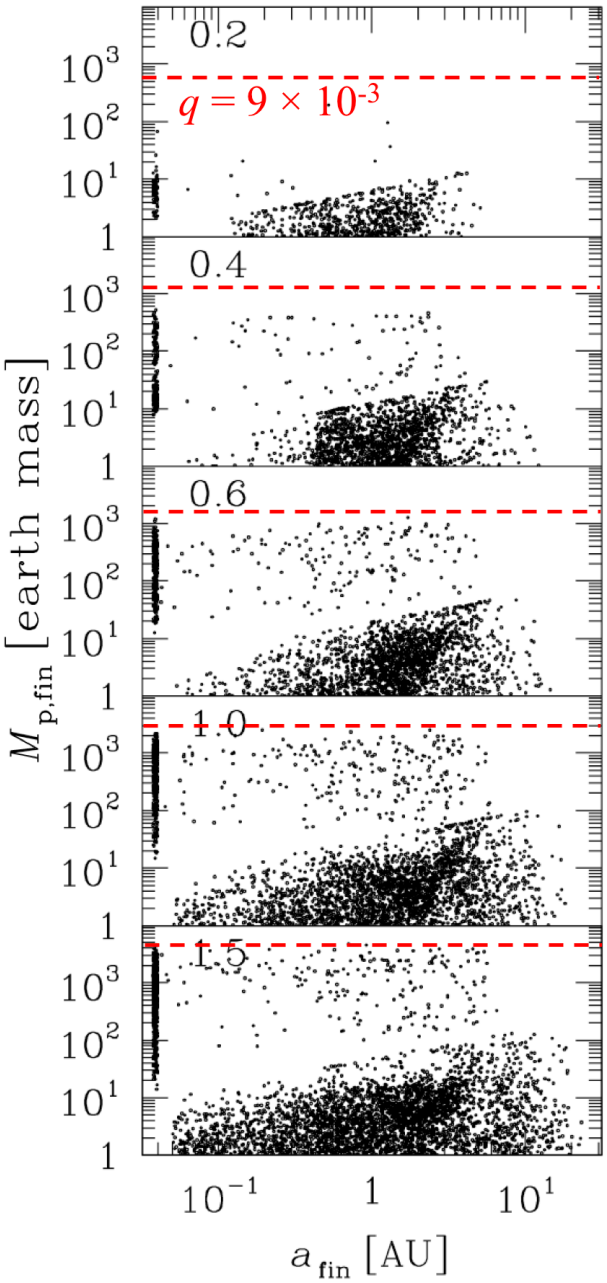


Figure 5.2: Prediction of the distribution of exoplanets, by the core accretion theory, around stars with different masses (Ida & Lin 2005). Each panel shows the distribution of exoplanets around the host star with each mass indicated on the top left (the unit is $M_\odot$). The red dashed horizontal lines indicate the mass ratio close to that of MOA-2016-BLG-227, $q = 9 \times 10^{-3}$. The figure is modified from Ida & Lin (2005).

## 5.2 The Way to Characterize Lens Properties

### 5.2.1 Combination of microlens parallax and lens flux

As discussed above, more reliable mass measurements of microlensing planets are needed to put a further constraint on the planet formation theory. In the analysis of OGLE-2012-BLG-0950, the lens mass was measured by combining only the microlens parallax and the lens flux. Although it is expected to become the most common combination in the era of space microlensing, this is the first measurement by the combination of mass–distance relations. The capability of measuring mass was demonstrated and some advantages of this method, compared with other methods using the angular Einstein radius as a mass–distance relation, were discussed in Section 3.8.

### 5.2.2 A new method to evaluate contamination probabilities

In Section 3.6.3, the contamination probability in the excess flux detected from the Keck AO image toward OGLE-2012-BLG-0950 was calculated, following previous studies (Janczak et al. 2010, Batista et al. 2014, Fukui et al. 2015) and it was concluded that the probability that a large part of the excess flux come from the lens star is high; $P(f = 0) = 62.6\%$, $P(f \leq 0.5) = 89.3\%$ and $P(f \leq 0.9) = 95.4\%$ for the parallax close+ model, where $f$ is the contamination fraction.

However, this kind of calculation has been found to be flawed because it mixes the prior probability with the posterior probability. Take the calculation of $P(f = 0) = 1 - P(0 < f < 1)$ for example, the $P(f = 0)$ on the left hand side indicates a "posterior" (or conditional) probability of $F_L = F_{\rm ex,obs}$, under the condition where an excess flux is observed as $F_{\rm excess} = F_{\rm ex,obs}$, or $P(F_L = F_{\rm ex,obs}|F_{\rm excess} = F_{\rm ex,obs})$. On the other hand, the $P(0 < f < 1) = P_{\rm amb}(0 < f < 1) + P_{SC}(0 < f < 1) + P_{LC}(0 < f < 1)$ on the right hand side is just the sum of the counts of each contaminant which have a brightness corresponding to $0 < f < 1$, by assuming each brightness distribution. This probability doesn't depend on whether an excess flux was observed or not, and thus it indicates the sum of "prior" probabilities or $P(0 < F_{\rm amb}/F_{\rm ex,obs} < 1) + P(0 < F_{SC}/F_{\rm ex,obs} < 1) + P(0 < F_{LC}/F_{\rm ex,obs} < 1)$. Figure 5.3 explains this calculation procedure by using the prior probability distributions from the analysis of MOA-2016-BLG-227, or from Figure 4.5 as an example. Therefore, the equation of $P(f \leq 0) = 1 - P(0 < f < 1)$ is problematic because it claims that a posterior probability can be calculated by subtracting a prior probability from 1. This problem is understood more easily when comparing Figure 5.3 with the next figure Figure 5.4 that shows the correct method for the calculation.

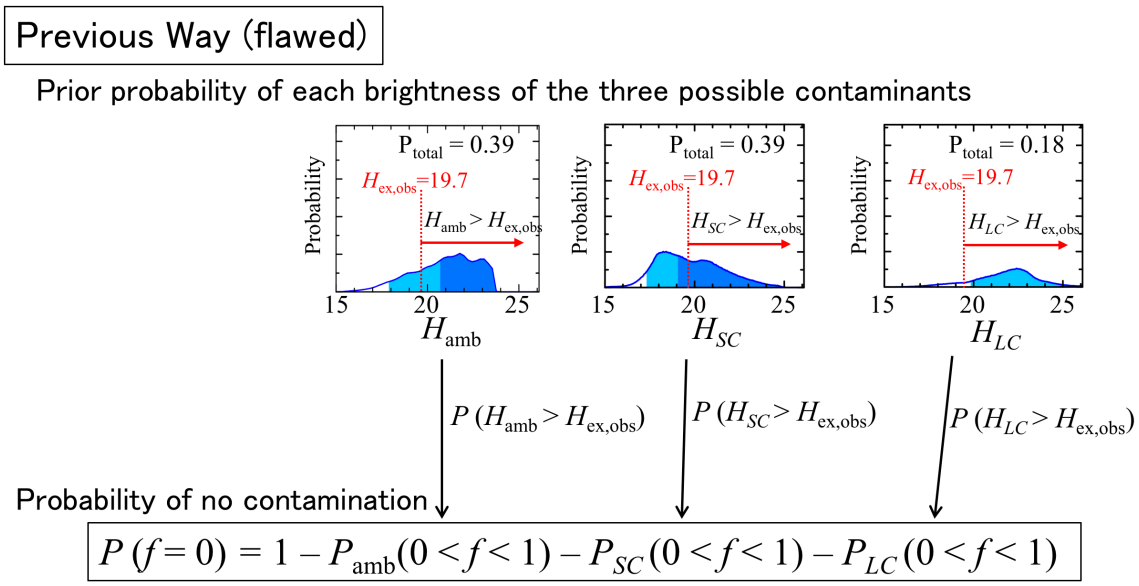


Figure 5.3: Explanation of the previous method of contamination probability calculation. Each panel is repeated from Figure 4.5. In the example case of MOA-2016-BLG-227, where we have an observed excess flux $H_{\rm ex,obs} = 19.7 \pm 0.4$, the previous way counts stars fainter than 19.7 mag from the prior probability distribution of each of the three contaminants, and then subtracts the sum of them from one. It then treats the remainder as the probability of no contamination, $P(f = 0)$.

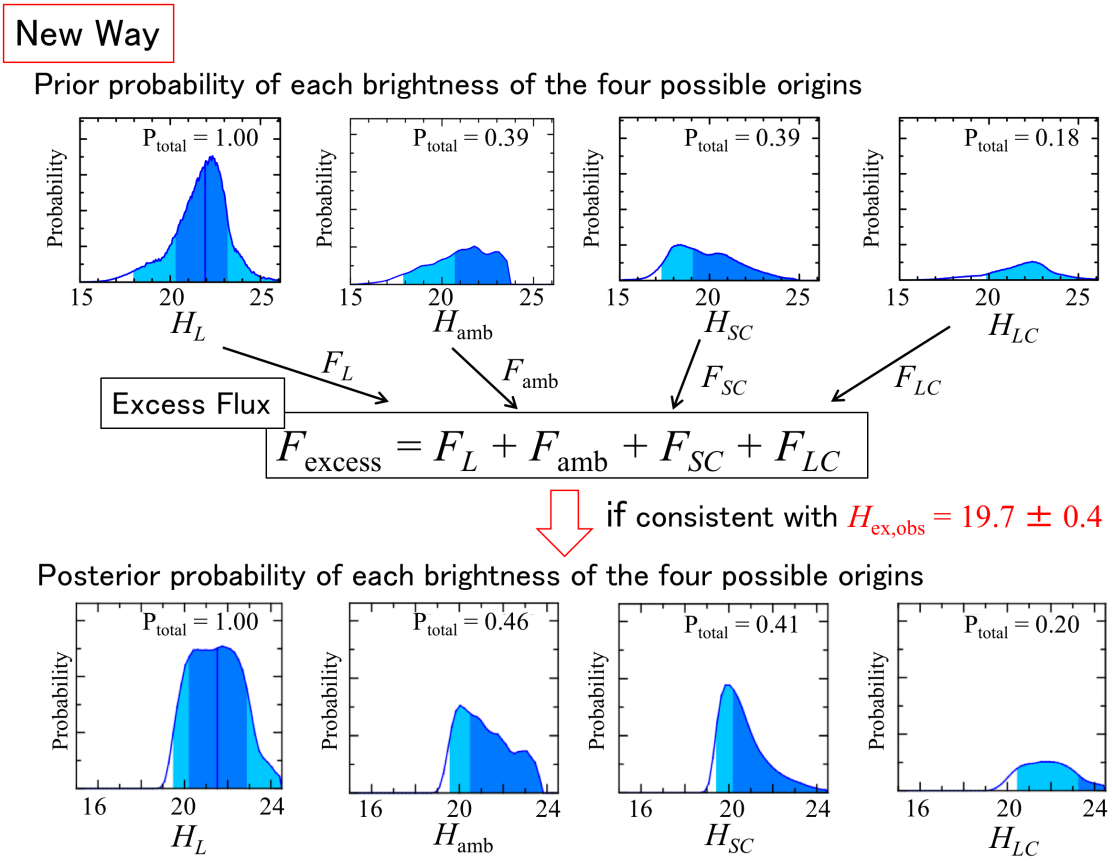


Figure 5.4: Explanation of the new method of contamination probability calculation. Each panel is repeated from Figures 4.5 and 4.6. The new method calculates the posterior probability distributions by accepting combinations of the four brightnesses, which are consistent with the observed excess flux value.

To calculate the posterior contamination probability correctly, the following method to calculate the posterior joint probability density function (PDF) is proposed in Koshimoto et al. (2018, in preparation),

$$f_{post}(F_L, F_{\rm amb}, F_{SC}, F_{LC} | F_{\rm excess} = F_{\rm ex,obs}) = \left. \frac{f_{pri}(F_L, F_{\rm amb}, F_{SC}, F_{LC})}{\int_{F_L, F_{\rm amb}, F_{SC}, F_{LC}} f_{pri}(F_L, F_{\rm amb}, F_{SC}, F_{LC})\ dF_L\, dF_{\rm amb}\, dF_{SC}\, dF_{LC}} \right|_{F_i \geq 0, F_{\rm excess} = F_{\rm ex,obs}}, \tag{5.1}$$

where $f_{pri}(F_L, F_{\rm amb}, F_{SC}, F_{LC})$ is the prior joint PDF of $F_L, F_{\rm amb}, F_{SC}$ and $F_{LC}$ and $F_{\rm excess} \equiv F_L + F_{\rm amb} + F_{SC} + F_{LC}$. In the analysis of MOA-2016-BLG-227, this probability was calculated following the procedure briefly summarized in Section 4.7 to study the possibility of excess flux from stars other than the lens star. The same procedure is also explained in Figure 5.4, which focuses on the difference from the previous way in Figure 5.3.

There has been a common assumption that, until this study, the excess flux detected at the source is likely to be largely comprised of that of the lens star. This is partly because the previous procedure for calculating the probability of contamination contains a flaw, explained above. This almost always gives a large probability of the lens as the origin of any excess flux. However, the analysis in Chapter 4 indicated that it is unlikely that a large fraction of the excess flux comes from the lens of MOA-2016-BLG-227. In Koshimoto et al. (2018, in preparation), this method is applied toward several planetary events previously published, including OGLE-2012-BLG-0950. As a result, there is only a small probability that the excess flux is due to the lens star for events with small angular Einstein radii, in contrast to conclusions presented by the original papers. This is because a small angular Einstein radius indicates relatively large prior probability of the lens being too faint ($H_L \gtrsim 20$) to be detected. Nevertheless, a very similar result to the one we presented in Chapter 3 for OGLE-2012-BLG-0950 is found, because its relatively large $t_E$ value indicates that the lens is likely to be a massive (i.e, bright) star, and this results in a large probability that the detected bright excess flux is due to the lens. In the *WFIRST* mission, the excess flux is considered as one of main tools to determine the lens mass because it is routinely obtained by its high angular resolution survey. Therefore, the new approach is crucial for the analysis of all microlensing events found by *WFIRST*, and would greatly contribute to the science goal of the completion of the statistical census of planetary systems in our galaxy.

# Acknowledgement

Many people contributed to my studies. I acknowledge for Professor H. Shibai who gives me a working environment and recommended this study area of microlensing. I would like to express my appreciation to Associate Professor T. Sumi who always gives me many valuable comments and proposes directions of my academic life. I would like to express my great gratitude to Dr. D. P. Bennett who accepted my visit to NASA/GSFC and supported my stay there. I could finish the work on MOA-2016-BLG-227 and come up with the idea of using a Bayesian analysis to calculate the contamination probabilities during the stay thanks to his many helps. Special thanks also go to Assistant Professor T. Matsuo who helps my study by giving comments from his very wide knowledge. I would like to thank to all members of MOA collaboration. Especially, Dr. D. Suzuki and Dr. A. Fukui give me a lot of advice of analysis and Dr. N. J. Rattenbury corrects English of my papers. I also grateful to the members of my laboratory in Osaka University and my office in NASA for sharing many discussions and my beneficial days.

# Appendix A

# Annual Parallax Effect

Here I describe the parallax effect in more detail. The following explanation is based on An et al. (2002).

## A.1 Introduction of needed parameters

When the proper motions of the source and the lens from the Sun are $\boldsymbol{\mu}_{S,hel}$ and $\boldsymbol{\mu}_{L,hel}$ and their positions at a reference time $t_c$ are $\boldsymbol{\varphi}_{S,c}$ and $\boldsymbol{\varphi}_{L,c}$, respectively, their positions at any given time $t$ from the Earth are expressed generally by

$$\boldsymbol{\varphi}_S(t) = \boldsymbol{\varphi}_{S,c} + (t - t_c)\boldsymbol{\mu}_{S,hel} + \pi_S \boldsymbol{s}(t), \tag{A.1}$$

$$\boldsymbol{\varphi}_L(t) = \boldsymbol{\varphi}_{L,c} + (t - t_c)\boldsymbol{\mu}_{L,hel} + \pi_L \boldsymbol{s}(t), \tag{A.2}$$

where $\pi_S = 1\mathrm{AU}/D_S$ and $\pi_L = 1\mathrm{AU}/D_L$. Here $\boldsymbol{s}(t)$ is the position vector of the Sun from the Earth projected onto the target sky normalized by an astronomical unit. Then, the angular separation vector of the source from the lens normalized by $\theta_E$ is

$$\boldsymbol{u}(t) = \boldsymbol{v}_c + (t - t_c)\frac{\boldsymbol{\mu}_{rel,hel}}{\theta_E} - \pi_E \boldsymbol{s}(t), \tag{A.3}$$

where

$$\begin{aligned} \boldsymbol{v}_c &= \frac{\boldsymbol{\varphi}_{S,c} - \boldsymbol{\varphi}_{L,c}}{\theta_E}, \\ \boldsymbol{\mu}_{rel,hel} &= \boldsymbol{\mu}_{S,hel} - \boldsymbol{\mu}_{L,hel}, \\ \pi_E &\equiv \frac{\pi_L - \pi_S}{\theta_E}. \end{aligned} \tag{A.4}$$

The third term of Eq. (A.3) represents the effect of the Earth's motion, and it is easy to understand the difference between the heliocentric and geocentric

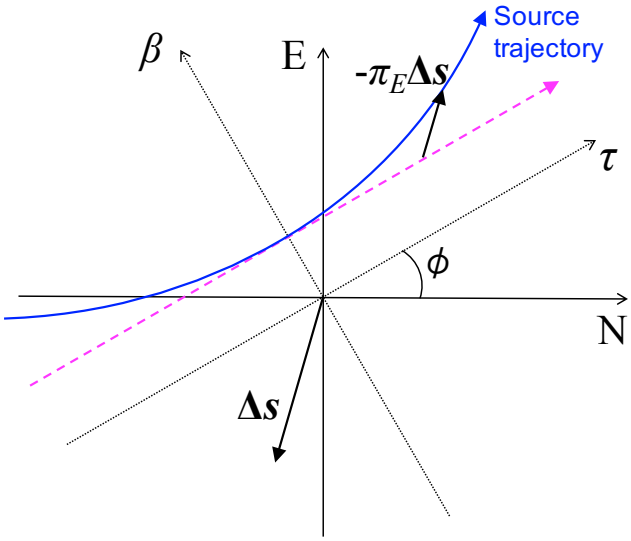


Figure A.1: Geometry of the introduced parameters for the annual parallax effect on the lens plane. The lens is at the origin, and the blue solid curved line and the magenta dashed line indicate the source trajectory with, and without the parallax effect, respectively.

reference frames from this formula. However, to treat the parallax effect, it is useful to divide the Earth's motion into two terms, one with linear motion and the other with non-linear motion. The Taylor series expansion of $\boldsymbol{s}(t)$ around $t = t_c$ is

$$\boldsymbol{s}(t) = \boldsymbol{s}(t_c) + \dot{\boldsymbol{s}}(t_c)(t - t_c) + \frac{\ddot{\boldsymbol{s}}(t_c)}{2}(t - t_c)^2 + \frac{\dddot{\boldsymbol{s}}(t_c)}{6}(t - t_c)^3 + \ldots, \tag{A.5}$$

thus

$$\begin{aligned}\boldsymbol{u}(t) &= (\boldsymbol{v}_c - \pi_E \boldsymbol{s}(t_c)) + (t - t_c)\left(\frac{\boldsymbol{\mu}_{rel,hel}}{\theta_E} - \pi_E \dot{\boldsymbol{s}}(t_c)\right) - \pi_E \Delta\boldsymbol{s}(t) \\ &= \boldsymbol{u_c} + (t - t_c)\frac{\boldsymbol{\mu}_{rel,geo,c}}{\theta_E} - \pi_E \Delta\boldsymbol{s}(t),\end{aligned} \tag{A.6}$$

where

$$\Delta\boldsymbol{s}(t) \equiv \boldsymbol{s}(t) - \boldsymbol{s}(t_c) - \dot{\boldsymbol{s}}(t_c)(t - t_c) = \frac{\ddot{\boldsymbol{s}}(t_c)}{2}(t - t_c)^2 + \frac{\dddot{\boldsymbol{s}}(t_c)}{6}(t - t_c)^3 + \ldots, \tag{A.7}$$

$$\boldsymbol{u_c} \equiv \boldsymbol{v}_c - \pi_E \boldsymbol{s}(t_c), \tag{A.8}$$

$$\boldsymbol{\mu}_{rel,geo,c} \equiv \boldsymbol{\mu}_{rel,hel} - (\pi_L - \pi_S)\dot{\boldsymbol{s}}(t_c). \tag{A.9}$$

If the reference time $t_c$ is taken as $t_c = t_0$, the $\boldsymbol{u_c}$ vector becomes perpendicular to the $\boldsymbol{\mu}_{rel,geo,c}$ vector, and the magnitudes of two vectors become $|\boldsymbol{u_c}| = u_0$ and $|\boldsymbol{\mu}_{rel,geo,c}| = \mu_{rel}$. Taking the $\tau$ axis to be along the $\boldsymbol{\mu}_{rel}$ vector, and the $\beta$ axis to be perpendicular to the $\tau$ axis vector, so that the coordinate becomes right-handed

(this is why $u_0$ can be a negative value), the $\boldsymbol{u}(t)$ can be divided into the two components of the new defined coordinate system of $\tau$-$\beta$ as

$$\boldsymbol{u}(t) = \begin{pmatrix} u_\tau(t) \\ u_\beta(t) \end{pmatrix} = \begin{pmatrix} \dfrac{t-t_0}{t_E} - \pi_E \Delta s_\tau(t) \\ u_0 - \pi_E \Delta s_\beta(t) \end{pmatrix}, \tag{A.10}$$

where $t_E = \theta_E/\mu_{rel}$ is used. While the $\tau$ and $\beta$ components of $\Delta\boldsymbol{s}$ are required to calculate the source trajectory of $\boldsymbol{u}(t)$, the north and east components of $\Delta\boldsymbol{s}$ vector, $\Delta s_n$ and $\Delta s_e$, can be calculated from the Earth's motion and the target direction. Here north and east can be defined in any celestial coordinates, although the equatorial system is normally used. Thus, we need an additional free parameter, $\phi$, to calculate $\boldsymbol{u}(t)$, which is the angle of the $\tau$ axis measured from the north direction on the sky toward the target. Figure A.1 shows the geometry on the lens plane. With the coordinate angle rotation of $\phi$,

$$\boldsymbol{u}(t) = \begin{pmatrix} \dfrac{t-t_0}{t_E} - \pi_E(\Delta s_n(t)\cos\phi + \Delta s_e(t)\sin\phi) \\ u_0 - \pi_E(\Delta s_e(t)\cos\phi - \Delta s_n(t)\sin\phi) \end{pmatrix} \tag{A.11}$$

and if a new vector is defined

$$\boldsymbol{\pi}_E \equiv \pi_E \frac{\boldsymbol{\mu}_{rel}}{\mu_{rel}} = (\pi_{E,N}, \pi_{E,E}) = (\pi_E \cos\phi, \pi_E \sin\phi) \tag{A.12}$$

where $\pi_{E,N}$ and $\pi_{E,E}$ are the north and the east components of $\boldsymbol{\pi}_E$, then

$$\boldsymbol{u}(t) = \begin{pmatrix} \dfrac{t-t_0}{t_E} - \pi_{E,N}\Delta s_n(t) - \pi_{E,E}\Delta s_e(t) \\ u_0 - \pi_{E,N}\Delta s_e(t) + \pi_{E,E}\Delta s_n(t) \end{pmatrix} \tag{A.13}$$

is derived. Therefore ($\pi_E$, $\phi$) or ($\pi_{E,N}$, $\pi_{E,E}$) are needed as additional fitting parameters to explain the annual parallax effect.

## A.2 Timescale of parallax event

Next, the timescale of the event in which the annual parallax effect can be seen is considered. The square of the magnitude of $\boldsymbol{u}(t)$ is

$$|\boldsymbol{u}(t)|^2 = t_n^2 - 2\pi_E \Delta s_\tau(t) t_n + \pi_E^2 |\Delta\boldsymbol{s}(t)|^2 \tag{A.14}$$

where $t_n = (t - t_0)/t_E$, considering the case of $u_0 \to 0$ for simplicity. Because the $t_n$ is $t_n \lesssim 1$ during a typical ongoing microlensing event, the parallax effect

of the second and the third terms is observable when $\pi_E|\Delta\boldsymbol{s}(t)|$ is larger than, or comparable to, $\lesssim 1$ under the condition of $t_n \lesssim 1$. Assuming the Earth's orbit is circular for simplicity, Equation (A.7) is rewritten as

$$\begin{aligned}\Delta\boldsymbol{s}(t) &= -\frac{\Omega^2\boldsymbol{s}(t_0)}{2}(t-t_0)^2 - \frac{\Omega^3(\dot{\boldsymbol{s}}(t_0)/\Omega)}{6}(t-t_0)^3 + \dots \\ &= -\frac{\boldsymbol{s}(t_0)}{2}(\Omega t_E t_n)^2 - \frac{(\dot{\boldsymbol{s}}(t_0)/\Omega)}{6}(\Omega t_E t_n)^3 + \dots \end{aligned} \tag{A.15}$$

where $\Omega = 2\pi/1\mathrm{yr}$ is the mean motion of the Earth's orbit. Because the $|\boldsymbol{s}(t_0)|$ takes between 0.1 - 1.0 depending on the Earth's season and $\pi_E \sim 0.1$ typically, the parallax effect can be seen when $t_E$ is comparable to $1/\Omega \simeq 58$ days.

# Appendix B

# Xallarap analysis for OGLE-2012-BLG-0950

If the source star is in a binary system, the orbital motion of the source star can also measurably affect the trajectory of the source during a microlensing event. This effect, called xallarap, requires additional parameters which define orbital elements of the source system whereas we know the Earth's orbital elements for the parallax effect. This model requires 7 additional fitting parameters to the standard binary model, the direction toward the Earth relative to the source orbital plane, $R.A._{\xi}$ and $Dec._{\xi}$, the orbital period $P_{\xi}$, the orbital eccentricity $\epsilon$ and the perihelion time $t_{\rm peri}$ in addition to $\boldsymbol{\xi_{\rm E}} = (\xi_{\rm E,N}, \xi_{\rm E,E})$ which is analogous to $\boldsymbol{\pi_{\rm E}}$ for microlens parallax. We omitted $\epsilon$ and $t_{\rm peri}$ as fitting parameters by assuming a circular orbit. Here we describe the results of our xallarap analysis and comparison with the parallax model, and discuss the possibility.

## B.1 Constraint by the companion mass upper limit

Kepler's 3rd law gives us a relation of the source orbit;

$$\xi_{\rm E} = \frac{\rm AU}{D_S \theta_* / \rho} \left( \frac{M_C}{M_\odot} \right) \left( \frac{M_\odot}{M_S + M_C} \frac{P_\xi}{1{\rm yr}} \right)^{2/3} \tag{B.1}$$

where $M_S$ and $M_C$ are the masses of the source and its companion, respectively. The $\xi$, $\rho$ and $P_\xi$ are fitting parameters, $\theta_*$ is measured, and $D_S$ and $M_S$ are reasonably constrained by the Galactic model combined with the source color and magnitude values. Then, for a given MCMC chain, $M_C$ can be calculated from this relation.

In xallarap fitting with no constraints, we found that the light curve prefers a solution with an unrealistically massive source companion with a mass of $M_C \sim 400\ M_\odot$. Thus, we conducted the fitting with the following constraint. We can place an upper limit of the companion mass $M_C < M_{C,\rm max}$ from Equation (3.6) of the excess flux with an assumption that the companion is not a stellar remnant. That corresponds to placing an upper limit of $\xi_{\rm E}$ as $\xi_{\rm E} < \xi_{\rm E,max}$ where $\xi_{\rm E,max}$ is defined as $\xi_{\rm E}$ of Equation (B.1) with $M_C = M_{C,\rm max}$ (Bennett et al. 2008, Sumi et al. 2010). We applied the additional $\chi^2$ penalty presented by Bennett et al. (2008) to each link of MCMC fitting;

$$\chi^2_{\rm orb} = \Theta(\xi_{\rm E} - \xi_{\rm E,max}) \left( \frac{\xi_{\rm E} - \xi_{\rm E,max}}{\sigma_{\xi_{\rm E,max}}} \right)^2 \tag{B.2}$$

where $\Theta$ is the Heaviside step function and we applied 7% to $\sigma_{\xi_{\rm E,max}}$, the uncertainty of $\xi_{\rm E,max}$, with the consideration of uncertainty on $\theta_*$ as given in Section 3.5.

We derive $D_S = 8.0 \pm 1.6$ kpc by a Bayesian analysis using the Galactic model (Han & Gould 1995) as the prior distribution constrained by the observed $t_{\rm E}$ value, $M_S = 1.02 \pm 0.12 M_\odot$ and $M_{C,\rm max} = 1.10 \pm 0.19 M_\odot$ from the color and brightness of the source and blending. To calculate $\xi_{\rm E,max}$, we use the lower or upper limit value for each parameter so that it makes $\xi_{\rm E,max}$ larger for a conservative constraint, namely, we use $D_S = 6.4$ kpc, $M_S = 0.9 M_\odot$, $M_{C,\rm max} = 1.2 M_\odot$ for the calculation of $\xi_{\rm E,max}$. Note that we adopt $1.2 M_\odot$ as $M_{C,\rm max}$ considering very few population of $M > 1.2 M_\odot$ stars in our galaxy (Gould 2000b, Bensby et al. 2013). For $\rho$ and $P_\xi$, we used each link's values to calculate the $\xi_{\rm E,max}$.

The "xallarap" models in Table 3.2 are our results of xallarap fitting with a circular orbit and the $\xi_{\rm E,max}$ constraint above. We find smaller $\chi^2$ values than that from the parallax models by $\Delta\chi^2 \gtrsim 27$. Note that including eccentricity intends to fit systematics in the baseline and does not improve a model significantly, therefore, we do not consider eccentric orbits according to Occam's razor.

## B.2 Constraint on $\rho$ and lens properties

Xallarap models place a lower limit on $\rho$ whereas the parallax models do not. This is because the $\xi_{\rm E,max}$ constraint is equivalent to placing a lower limit of $\rho$ as

$$\xi_{\rm E} < \xi_{\rm E,max} \Leftrightarrow \rho > \rho_{\rm min} \equiv \frac{\theta_* D_S \xi_{\rm E}}{M_{C,\rm max}(M_{C,\rm max} + M_S)^{-2/3} P_\xi^{2/3}}. \tag{B.3}$$

Combining it with the upper limit from the finite source effect, we can constrain the $\rho$ value with $\sim 30\%$ uncertainty. This is the first case of $\rho$ being constrained

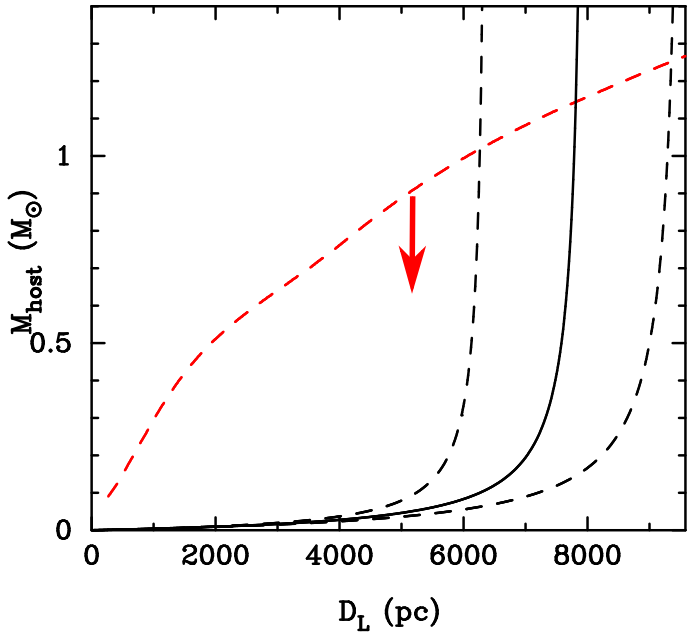


Figure B.1: Same as Figure 3.6 but for the xallarap close+ model. The relation from $M_{H,L,\mathrm{low}}$ (i.e., 1 $\sigma$ brighter limit of $M_{H,L}$ ) is shown in red. The red arrow means that the red dashed line is just an upper limit. Black lines are the mass–distance relation come from $\theta_{\mathrm{E}}$ .

with neither a significant finite source effect nor a parallax effect. Then we can calculate a $\theta_{\mathrm{E}}$ value from $\rho$ and $\theta_*$,

$$\theta_{\mathrm{E}} = 0.20^{+0.04}_{-0.08}\ \mathrm{mas}, \quad \mu_{rel} = 1.1^{+0.2}_{-0.4}\ \mathrm{mas/yr}$$

for the xallarap close+ model. Table 3.3 shows these values for all degenerate models using each models' values.

In principle, we can determine a mass and distance of the lens star by combining the $\theta_{\mathrm{E}}$ and $H_L$, the lens flux in $H$-band extracted from Keck AO observations (Batista et al. 2014, Fukui et al. 2015:e.g.) because $\theta_{\mathrm{E}}$ gives us a mass–distance relationship;

$$M_{\mathrm{host}} = \frac{1}{1+q}\frac{\theta_{\mathrm{E}}^2}{\kappa\pi_{\mathrm{rel}}} \tag{B.4}$$

and we can convert the lens flux into another mass–distance relationship using a mass-luminosity relation. However, we encounter a problem with this. As shown in Table B.1, the uncertainty of the mass of the companion to the source star in the xallarap models is very large and the upper limit of $\sim 1.8 M_\odot$ is larger than $M_{C,\mathrm{max}} = 1.2 M_\odot$, the maximum mass of the companion we use in the $\xi_{\mathrm{E,max}}$ constraint. In other words, the lower limit of $H_C$, the apparent $H$ magnitude of

Table B.1: 1 $\sigma$ possible value ranges of mass and $H$ magnitude of the source companion for xallarap models.

| Model | $M_C$ ($M_\odot$) | $H_C$ (mag) |
|---|---|---|
| Xallarap | | |
| close+ | 0.57 - 1.71 | 16.3 - 20.4 |
| close− | 0.56 - 1.71 | 16.3 - 20.5 |
| wide+ | 0.62 - 1.81 | 16.1 - 20.7 |
| wide− | 0.60 - 1.76 | 16.2 - 20.2 |

**Notes.** The range of 1 $\sigma$ error is shown for each parameter.

the companion, is brighter than the brightness limit as $H_C \simeq 16.2$ mag $< H_{\rm excess} \simeq 17.5$ mag where $H_{\rm excess}$ value comes from Equation (3.6). It means we cannot place a fainter limit on $H_L$, the lens brightness in the $H$-band.

These excesses are attributed to the uncertainties of the parameters that determine $\xi_{\rm E,max}$, i.e., the uncertainties of $D_S$, $M_S$ and $\theta_*$. Especially, it is more sensitive to the uncertainties of $\theta_*$ and $D_S$ rather than $M_S$ due to the relation between $M_C$ and the other parameters, $\xi_{\rm E} \propto (D_S\theta_*)^{-1} M_C (M_S + M_C)^{-2/3}$. We calculate a $\xi_{\rm E,max}$ value with the most conservative combination of $D_S$ and $M_S$ in their 1 $\sigma$ uncertainties, $D_S = 6.4$ kpc and $M_S = 0.9 M_\odot$, so that they make the $\xi_{\rm E,max}$ largest in the 1 $\sigma$ range. Then we judge a set of ($\rho$, $P_\xi$, $\xi_{\rm E}$) by the conservatively large $\xi_{\rm E,max}$ value and accept them up to 7% larger $\xi_{\rm E}$ than $\xi_{\rm E,max}$ considering the uncertainty on $\theta_*$. Thus the $M_C$ value range derived from the accepted parameters with $D_S = 8.0 \pm 1.6$ kpc and $M_S = 1.02 \pm 0.12 M_\odot$ can exceed its limit, $M_{C,\rm max} = 1.2 M_\odot$.

We can obtain only brighter limit of $H_L$ by subtracting the source brightness and the fainter limit of $H_C$ from $H_{\rm target}$ of Equation (3.5),

$$H_L > H_{L,\rm low} = 17.66. \tag{B.5}$$

Then we can place a lower limit of $M_{H,L}$ of $M_{H,L,\rm low} = H_{L,\rm low} - A_{H,L} - 5\log(D_L/10{\rm pc})$ by using Equation (3.10) with $H_{L,\rm low}$. Figure B.1 shows the mass–distance relation obtained from Equation (B.4) and $M_{H,L,\rm low}$. From their overlapped region, we obtain constraints on the host mass and the distance as $M_{\rm host} < 1.16 M_\odot$ and $D_L < 9.3$kpc, respectively. These constraints are very weak.

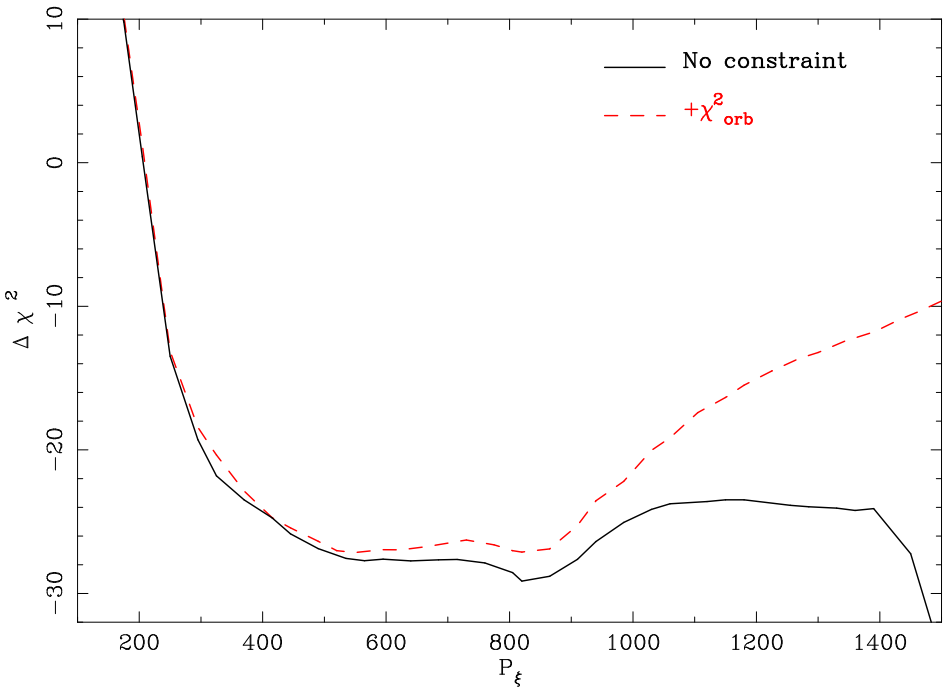


Figure B.2: $\Delta\chi^2$ between a xallarap model and the parallax close+ model as a function of orbital period. The black solid and red dashed lines indicate xallarap models with no constraint and the $\chi^2_{\rm orb}$ constraint, respectively, see text.

## B.3 Comparison with parallax model

Xallarap models have $\chi^2$ differences from the parallax models by $\Delta\chi^2 > 27$ for 3 dof difference. Poindexter et al. (2005) analyzed 22 events where a parallax model improves their light curve fittings compared to the standard model. According to their analysis, there are 3 events that prefer a xallarap model to a parallax model by $\Delta\chi^2 > 25$ in all events they analyzed. They regard it as a strong indication that the light curves of the 3 events have been distorted by xallarap. Here, we investigate whether the xallarap signal is real or unreal by the analyses bellow.

We first plot $\chi^2$ values of the best-fit xallarap model at a fixed $P_\xi$ value within $100 \leq P_\xi({\rm days}) \leq 1500$ in Figure B.2. They are shown as $\Delta\chi^2$ values compared to the parallax close+ model. One of standard ways to exclude a xallarap scenario is to show that just a narrow range of $P_\xi$ indicates a (small) preferences of xallarap model to parallax model, then showing very small probability that a binary system whose period is in such the narrow range happens to be microlensed (Bennett et al. 2008). For this event, however, the favored $P_\xi$ region compared to the parallax

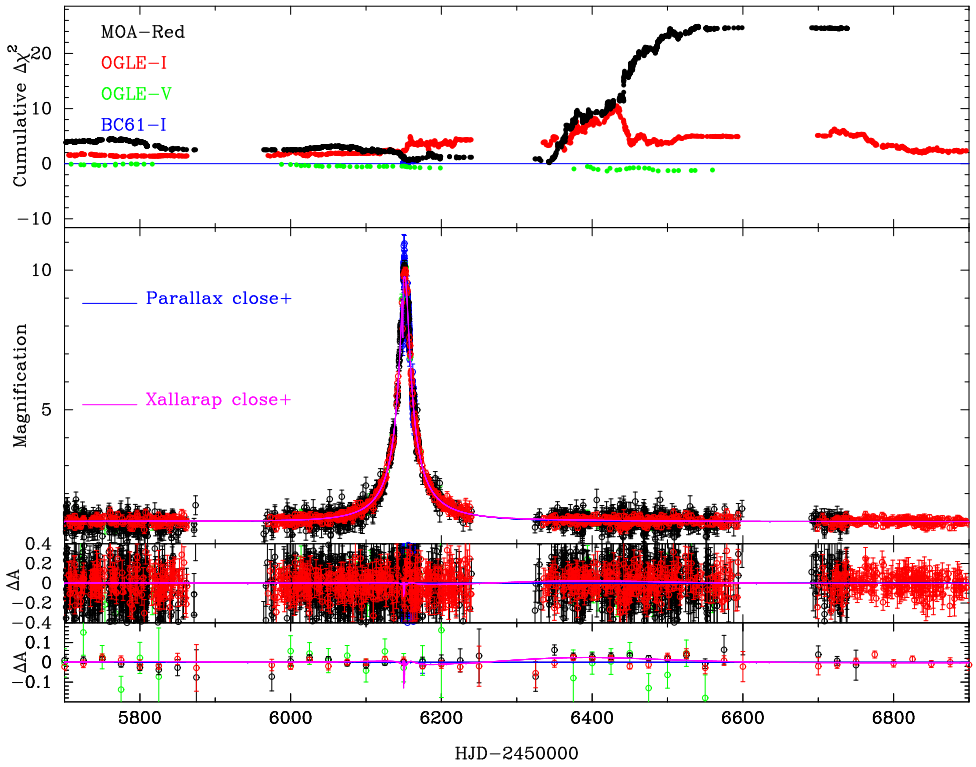


Figure B.3: As for Figure 3.3, but showing the difference between the parallax close+ model and the xallarap close+ model. A positive $\Delta\chi^2$ value indicates a smaller $\chi^2$ of the xallarap close+ model.

model is very broad even with $\chi^2_{\rm orb}$ constraint. Therefore, we cannot exclude the xallarap scenario by this approach.

Next, we investigate where the signal comes from in the light curve. Figure B.3 shows the same one as Figure 3.3, but shows the difference between the xallarap close+ model and the parallax close+ model. The $\chi^2$ difference comes from the data in 2013 which is slightly magnified. However, the preference to the parallax model comes almost exclusively from MOA data and the preference from OGLE data is only $\Delta\chi^2 \sim 2$. The MOA data is more easily affected by systematics especially in a low-magnification part because the average seeing on the MOA site is worse than that on the OGLE site. In addition to this inconsistency between MOA and OGLE, as shown in Table B.1, a significant fraction of MCMC chains of every xallarap model indicates unphysically large mass of the companion even with the mass constraint imposed. These two facts are strong evidence against the xallarap model as the true model. Thus, we conclude that the xallarap models are very likely to be the results due to low level systematics in the MOA data.

Finally, we fit the data consisting of only anomaly part of MOA data (39 points) and entire OGLE $I$ data (1273 points) with both parallax and xallarap with no constraint models because the results are expected to be less affected by systematics. Note that we use a portion of MOA data so that the best fit will not change largely except $\pi_{\rm E}$ or $\xi_{\rm E}$. The xallarap model improves the fit by $\Delta\chi^2 = 6.5$ compared to the parallax model for 3 dof difference. This indicates that the xallarap model is preferred by only $< 2\sigma$. Moreover, we compared these two models by the Bayesian information criterion (BIC), which is another common statistical criterion including penalty term for the number of fitting parameters, $BIC = \chi^2 + n_{\rm param} \ln(N_{\rm data})$ (Burnham & Anderson 2002). The $\Delta BIC$ is $BIC_{\rm para} - BIC_{\rm xalla} \sim -15$ and this criterion prefers the parallax model rather than the xallarap model.

Considering these facts, we conclude that the parallax model is preferred over the xallarap model. Thus, we dealt with only parallax scenario in the main part of the paper.

# Appendix C

# Comparison of Different Extinction Laws for MOA-2016-BLG-227

In Section 4.5.2, we obtained the observed extinction value, $A_{I,\rm obs} = 0.98 \pm 0.07$, and color excess values of $E(V-I)_{\rm obs} = 0.82 \pm 0.04$, $E(V-H)_{\rm obs} = 1.67 \pm 0.11$ and $E(I-H)_{\rm obs} = 0.81 \pm 0.07$. Then, we fit these values to the extinction laws of Cardelli et al. (1989), Nishiyama et al. (2009) and Nishiyama et al. (2008) separately and compared the results. This was motivated by the fact that Nataf et al. (2016) reported a clear difference of their extinction law towards the Galactic bulge from the standard law of Cardelli et al. (1989). Hereafter, we refer to these papers as C89, N09 and N08, respectively. Note that the four observed extinction parameters (1 extinction and 3 color excess) are not independent. They can be derived from the three independent extinction values: $A_{I,\rm obs}$, $A_{V,\rm obs}$ and $A_{H,\rm obs}$.

The C89 law is given by equations (1) - (3b) in their paper, and $A_V$ and $R_V$ serve as the parameters of their model.

Unlike C89, N09 does not provide a complete extinction model. They provide only ratios of extinctions for wavelengths longer than the $J$-band. So, we need additional information relating $A_V$ or $A_I$ and $A_J$, $A_H$ or $A_K$ in order to calculate the values that we need for this paper: $A_I$, $A_V$ and $A_H$. Therefore, we used the $R_{JKVI} \equiv E(J-K_s)/E(V-I)$ values from Nataf et al. (2013) in addition to the N09 extinction law. The $R_{JKVI}$ value at the nearest grid point to the MOA-2016-BLG-227 event in Table 3 of Nataf et al. (2013) is 0.3089. However, the quality flag for this value is 1, which indicates an unreliable measurement, so we use a conservative uncertainty of $R_{JKVI} = 0.31 \pm 0.03$. We adjust $A_I$ and $E(V-I)$ to minimize the $\chi^2$ value between the observed $A_{I,\rm obs}$, $E(V-I)_{\rm obs}$, $E(V-H)_{\rm obs}$, and $E(I-H)_{\rm obs}$ values and those values derived using the ratio $A_{H,\rm 2MASS}/E(J-K_s)_{\rm 2MASS} = 0.89$ from N09, in conjunction with the $R_{JKVI}$ value from Nataf et al. (2013). We

Table C.1: Comparison of the extinction and angular Einstein radius based on different extinction laws.

| Extinction law | None[a] | Cardelli et al. (1989) | Nishiyama et al. (2009) | Nishiyama et al. (2008) |
|---|---|---|---|---|
| Relation | - | $\frac{A_\lambda}{A_V} = a(x) + \frac{b(x)}{R_V}$ [b] | $\frac{A_H}{E(J-K_s)}$, $R_{JKVI}$ [c] | $\frac{A_J}{A_V}$, $\frac{A_H}{A_V}$, $\frac{A_{K_s}}{A_V}$ |
| $A_V$ | $1.80 \pm 0.08$ | $1.87 \pm 0.12$ | $1.83 \pm 0.12$ | $\mathbf{1.82 \pm 0.12}$ |
| $A_I$ | $0.98 \pm 0.07$ | $1.04 \pm 0.10$ | $1.01 \pm 0.08$ | $\mathbf{1.00 \pm 0.08}$ |
| $A_H$ | $0.17 \pm 0.10$ | $0.30 \pm 0.04$ | $0.23 \pm 0.04$ | $\mathbf{0.19 \pm 0.02}$ |
| $E(V-I)$ | $0.82 \pm 0.04$ | $0.83 \pm 0.05$ | $0.82 \pm 0.05$ | $\mathbf{0.82 \pm 0.05}$ |
| $E(V-H)$ | $1.67 \pm 0.11$ | $1.57 \pm 0.10$ | $1.60 \pm 0.11$ | $\mathbf{1.63 \pm 0.11}$ |
| $E(I-H)$ | $0.81 \pm 0.07$ | $0.73 \pm 0.06$ | $0.78 \pm 0.09$ | $\mathbf{0.81 \pm 0.08}$ |
| $\chi^2$/dof [d] | - | 2.39/1 | 0.56/1 | 1.19/2[e] |
| $\theta_{*,VI}$ ($\mu$as) | $0.65 \pm 0.04$ | $0.67 \pm 0.06$ | $0.66 \pm 0.05$ | $0.66 \pm 0.05$ |
| $\theta_{*,VH}$ ($\mu$as) | $0.67 \pm 0.04$ | $0.73 \pm 0.02$ | $0.70 \pm 0.02$ | $\mathbf{0.68 \pm 0.02}$ |
| $\theta_{*,IH}$ ($\mu$as) | $0.71 \pm 0.07$ | $0.79 \pm 0.06$ | $0.74 \pm 0.06$ | $0.72 \pm 0.06$ |
| $\mathrm{SD}_{\theta_*}$ [f] | 0.035 | 0.061 | 0.042 | 0.030 |
| $\theta_\mathrm{E}$ (mas) [g] | - | - | - | $\mathbf{0.227^{+0.006}_{-0.009}}$ |
| $\mu_\mathrm{rel}$ (mas/yr) [g] | - | - | - | $\mathbf{4.88^{+0.14}_{-0.17}}$ |

**Notes.** The values in boldface are used as final values.

[a] Result without using an extinction law. The $A_I$, $E(V-I)$, $E(V-H)$ and $E(I-H)$ values are determined directly from the data.

[b] Equation (1) of C89, see the paper for the detailed model.

[c] The $R_{JKVI}$ value comes from Table 3 of Nataf et al. (2013).

[d] When calculating the total $\chi^2$, we multiply each of the contributions from $E(V-I)$, $E(V-H)$ and $E(I-H)$ by 2/3, because these values are not independent.

[e] The dof = 2 is because we used the $R_{JKVI}$ value from Nataf et al. (2013) as an observed data point.

[f] Standard deviation of the three $\theta_*$ values.

[g] Calculations conducted only for the adopted $\theta_*$ value ($\theta_{*,VH}$ with N08).

explicitly use the $_{\rm 2MASS}$ subscript because N09 provides their result also in the IRSF/SIRIUS photometric system (Nagashima et al. 1999, Nagayama et al. 2003). Note that we calculate this $A_H/E(J-K_s)$ value using their result for the field S+ ($0^\circ < l < 3^\circ, -1^\circ < b < 0^\circ$), which is nearest of their fields to the MOA-2016-BLG-227 event position.

N08 also provide the ratio of extinctions towards the Galactic bulge ($l \sim 0^\circ, b \sim -2^\circ$). They find $A_J/A_V = 0.183 \pm 0.015$, $A_H/A_V = 0.103 \pm 0.008$ and $A_{K_s}/A_V = 0.064 \pm 0.005$. (These values are slightly different from the original values given by N08 because the values used in N08 were in the OGLE II and IRSF/SIRIUS photometric systems, so we converted them into the standard systems that we use here.) These values are well fit by a single power law, $A_\lambda/A_V \propto \lambda^{-2}$. Nevertheless, we use the ratios themselves, instead of the single power law, because N08 does not test that their power law accurately reproduces $A_I/A_V$, which we have now. As in the case of N09, we keep these ratios fixed, and adjust $A_I$ and $E(V-I)$ to minimize the $\chi^2$ between these relations and the observed $A_{I,\rm obs}$, $E(V-I)_{\rm obs}$, $E(V-H)_{\rm obs}$, and $E(I-H)_{\rm obs}$ values. Notice that N08 had $V$-band data and it was not necessary to use the $R_{JKVI}$ as a constraint. Therefore, we used the $R_{JKVI}$ value as the additional observed data instead here in addition to $A_{I,\rm obs}$, $A_{V,\rm obs}$ and $A_{H,\rm obs}$ to increase number of degrees of freedom (dof).

Table C.1 shows the results of fitting our extinction measurements to these three different extinction laws. This table also shows the angular source radius calculated from the extinction–corrected source magnitudes and colors using formulae from the analysis of Boyajian et al. (2014). We determine $\theta_{*,IH}$ using Equations (1)-(2) and Table 1 of Boyajian et al. (2014), but the other relations were provided by private communications from Boyajian with a special analysis restricted to stellar colors that are relevant for the Galactic bulge sources observed in microlensing events. We use Equation (4) of Fukui et al. (2015) to determine $\theta_{*,VI}$, and we use Equation (4) of Bennett et al. (2015) to determine $\theta_{*,VH}$. Those formulae are

$$\log\ [2\theta_{*,VI}/(1{\rm mas})] = 0.5014 + 0.4197(V-I)_{S,0} - 0.2I_{S,0}, \qquad \text{(C.1)}$$

$$\log\ [2\theta_{*,VH}/(1{\rm mas})] = 0.5367 + 0.0727(V-H)_{S,0} - 0.2H_{S,0}, \qquad \text{(C.2)}$$

$$\log\ [2\theta_{*,IH}/(1{\rm mas})] = 0.5303 + 0.3660(I-H)_{S,0} - 0.2I_{S,0}. \qquad \text{(C.3)}$$

If we compare the $\chi^2$ value for each model fit in Table C.1, we see that the $\chi^2$/dof for the N09 and N08 laws are smaller than the value from the C89 extinction law, although the C89 is not disfavored by a statistically significant amount. (The $p$-value of $\chi^2 = 2.39$ for dof $= 1$ remains at $\sim$0.12.) Note that a contribution of 0.96 to the total value of $\chi^2 = 1.19$ arises from fitting the $R_{JKVI}$ value to the N08 extinction law. Therefore, the remaining contribution of 0.23 to $\chi^2$ arises from fitting the N08 model to our measurements of the RGC centroids. This indicates that the extinction law of N08 agrees with our measurement of the red clump

centroids very well, but that well with the $R_{JKVI}$ value, which comes from Nataf et al. (2013).

From the point of view of consistency among the three $\theta_*$ values, the standard deviation of the three values ($\mathrm{SD}_{\theta_*}$ in the table) is the smallest using the N08 extinction laws. The N08 extinction law also yields the smallest error bars for $A_H$ and $\theta_{*,VH}$.

Based on this analysis, we have decided to use the results from the N08 extinction laws in our analysis. We use $\theta_{*,VH}$ for the final angular source radius, which is $\theta_* = 0.68 \pm 0.02$ $\mu$as. We show the source magnitudes and colors corrected for extinction using the N08 extinction laws in Table 4.3.

# Bibliography


Abe, F., Airey, C., Barnard, E., et al. 2013, MNRAS, 431, 2975

Alard, C. 2000, A&AS, 144, 363

Alard, C., & Lupton, R. H. 1998, ApJ, 503, 325

Alcock, C., Allsman, R. A., Alves, D., et al. 1995, ApJL, 454, L125

An, J. H., Albrow, M. D., Beaulieu, J.-P., et al. 2002, ApJ, 572, 521

Arnaboldi, M., Capaccioli, M., Mancini, D., et al. 1998, The Messenger, 93, 30

Batista, V., Gould, A., Dieters, S., et al. 2011, A&A, 529, A102

Batista, V., Beaulieu, J.-P., Gould, A., et al. 2014, ApJ, 780, 54

Batista, V., Beaulieu, J.-P., Bennett, D. P., et al. 2015, ApJ, 808, 170

Beaugé, C., & Nesvorný, D. 2013, ApJ, 763, 12

Beaulieu, J.-P., Bennett, D. P., Batista, V., et al. 2016, ApJ, 824, 83

Beaulieu, J.-P., Bennett, D. P., Fouqué, P., et al. 2006, Nature, 439, 437

Bennett, D.P, 2008, in Exoplanets, Edited by John Mason. Berlin: Springer. ISBN: 978-3-540-74007-0, (arXiv:0902.1761)

Bennett, D. P. 2010, ApJ, 716, 1408

Bennett, D. P., Anderson, J., Bond, I. A., Udalski, A., & Gould, A. 2006, ApJL, 647, L171

Bennett, D.P., Anderson, J., & Gaudi, B.S. 2007, ApJ, 660, 781

Bennett, D. P., Batista, V., Bond, I. A., et al. 2014, ApJ, 785, 155

Bennett, D. P., Bhattacharya, A., Anderson, J., et al. 2015, ApJ, 808, 169

Bennett, D. P., Bond, I. A., Udalski, A., et al. 2008, ApJ, 684, 663

Bennett, D. P., & Rhie, S. H. 1996, ApJ, 472, 660

Bennett, D. P., & Rhie, S. H. 2002, ApJ, 574, 985

Bennett, D. P., Rhie, S. H., Nikolaev, S., et al. 2010, ApJ, 713, 837

Bennett, D.P., Rhie, S.H., Udalski, A., et al. 2016, AJ, 152, 125

Bensby, T., Yee, J. C., Feltzing, S., et al. 2013, A&A, 549, A147

Bertin, E., & Arnouts, S. 1996, A&AS, 117, 393

Bertin, E., Mellier, Y., Radovich, M., et al. 2002, Astronomical Data Analysis Software and Systems XI, 281, 228

Bessell, M. S., & Brett, J. M. 1988, PASP, 100, 1134

Bhattacharya, A., Bennett, D. P., Anderson, J., 2017, AJ, submitted (arXiv:1703.06947)

Bond, I. A., Abe, F., Dodd, R. J., et al. 2001, MNRAS, 327, 868

Bond, I. A., Bennett, D. P., Sumi, T., et al., 2017, MNRAS, submitted.

Bond, I. A., Udalski, A., Jaroszyński, M., et al. 2004, ApJL, 606, L155

Bonfils, X., Delfosse, X., Udry, S., et al. 2013, A&A, 549, A109

Borucki, W. J., Koch, D., Basri, G., et al. 2010, Science, 327, 977

Borucki, W. J., Koch, D. G., Basri, G., et al. 2011, ApJ, 736, 19

Boss, A. P. 1997, Science, 276, 1836

Boss, A. P. 2006, ApJ, 643, 501

Boulade, O., Charlot, X., Abbon, P., et al. 2003, Proc. SPIE, 4841, 72

Boyajian, T. S., van Belle, G., & von Braun, K. 2014, AJ, 147, 47

Bramich, D. M. 2008, MNRAS, 386, L77

Bressan, A., Marigo, P., Girardi, L., et al. 2012, MNRAS, 427, 127

Burnham, K. P. & Anderson, D. R. 2002, Model Selection and Multimodel Inference (2nd ed.), Springer

Butler, R. P., Wright, J. T., Marcy, G. W., et al. 2006, ApJ, 646, 505

Calchi Novati, S., Gould, A., Udalski, A., et al. 2015, ApJ, 804, 20

Cardelli, J. A., Clayton, G. C., & Mathis, J. S. 1989, ApJ, 345, 245 (C89)

Carpenter, J. M. 2001, AJ, 121, 2851

Casagrande, L., & VandenBerg, D. A. 2014, MNRAS, 444, 392

Cassan, A., Kubas, D., Beaulieu, J.-P., et al. 2012, Nature, 481, 167

Chen, Y., Girardi, L., Bressan, A., et al. 2014, MNRAS, 444, 2525

Chen, Y., Bressan, A., Girardi, L., et al. 2015, MNRAS, 452, 1068

Chung, S.-J., Han, C., Park, B.-G., et al. 2005, ApJ, 630, 535

Claret, A. 2000, A&A, 363, 1081

Claret, A., & Bloemen, S. 2011, A&A, 529, A75

Cumming, A., Butler, R. P., Marcy, G. W., et al. 2008, PASP, 120, 531

Delfosse, X., Forveille, T., Ségransan, D., et al. 2000, A&A, 364, 217

Dominik, C., & Tielens, A. G. G. M. 1997, ApJ, 480, 647

Dong, S., Gould, A., Udalski, A., et al. 2009a, ApJ, 695, 970

Dong, S., Bond, I. A., Gould, A., et al. 2009b, ApJ, 698, 1826

Duchêne, G., & Kraus, A. 2013, ARA&A, 51, 269

Endl, M., Cochran, W. D., Kürster, M., et al. 2006, ApJ, 649, 436

Fukui, A., Gould, A., Sumi, T., et al. 2015, ApJ, 809, 74

Gaidos, E., Mann, A. W., Lépine, S., et al. 2014, MNRAS, 443, 2561

Gardner, J. P., Mather, J. C., Clampin, M., et al. 2006, Space Sci. Rev., 123, 485

Gaudi, B. S. 2012, ARA&A, 50, 411

Gaudi, B. S., Beaulieu, J. P., Bennett, D. P., et al. 2009, astro2010: The Astronomy and Astrophysics Decadal Survey, 2010,

Gaudi, B. S., Bennett, D. P., Udalski, A., et al. 2008, Science, 319, 927

Gilmozzi, R., & Spyromilio, J. 2007, The Messenger, 127, 11

González Hernández, J. I., & Bonifacio, P. 2009, A&A, 497, 497

Gonzalez, O. A., Rejkuba, M., Zoccali, M., et al. 2013, A&A, 552, A110

Gorbikov, E., Brosch, N., & Afonso, C. 2010, Ap&SS, 326, 203

Gould, A. 1992, ApJ, 392, 442

Gould, A. 2000a, ApJ, 542, 785

Gould, A. 2000b, ApJ, 535, 928

Gould, A., Dong, S., Gaudi, B. S., et al. 2010, ApJ, 720, 1073

Gould, A., & Loeb, A. 1992, ApJ, 396, 104

Gould, A., Udalski, A., An, D., et al. 2006, ApJL, 644, L37

Gould, A., Udalski, A., Monard, B., et al. 2009, ApJL, 698, L147

Gould, A., & Yee, J. C. 2014, ApJ, 784, 64

Gustafsson, B., Edvardsson, B., Eriksson, K., et al. 2008, A&A, 486, 951

Han, C., & Gould, A. 1995, ApJ, 447, 53

Han, C., Udalski, A., Choi, J.-Y., et al. 2013, ApJL, 762, L28

Hayashi, C., Nakazawa, K., & Nakagawa, Y. 1985, Protostars and Planets II, 1100

Henderson, C. B., Poleski, R., Penny, M., et al. 2016, PASP, 128, 124401

Hill, V., Lecureur, A., Gómez, A., et al. 2011, A&A, 534, A80

Howard, A. W., Marcy, G. W., Johnson, J. A., et al. 2010, Science, 330, 653

Ida, S., & Lin, D. N. C. 2004, ApJ, 604, 388

Ida, S., & Lin, D. N. C. 2005, ApJ, 626, 1045

Ida, S., Lin, D. N. C., & Nagasawa, M. 2013, ApJ, 775, 42

Jacob, W. S. 1855, MNRAS, 15, 228

Janczak, J., Fukui, A., Dong, S., et al. 2010, ApJ, 711, 731

Johns, M., McCarthy, P., Raybould, K., et al. 2012, Proc. SPIE, 8444, 84441H

Johnson, J. A., Aller, K. M., Howard, A. W., & Crepp, J. R. 2010, PASP, 122, 905

Johnson, J. A., Butler, R. P., Marcy, G. W., et al. 2007, ApJ, 670, 833

Johnson, C. I., Rich, R. M., Kobayashi, C., Kunder, A., & Koch, A. 2014, AJ, 148, 67

Kennedy, G. M., & Kenyon, S. J. 2008, ApJ, 673, 502

Kervella, P., Thévenin, F., Di Folco, E., & Ségransan, D. 2004, A&A, 426, 297

Kim, S.-L., Lee, C.-U., Park, B.-G., et al. 2016, JKAS, 49, 37

Koshimoto, N., Udalski, A., Beaulieu, J. P., et al. 2017a, AJ, 153, 1

Koshimoto, N., Shvartzvald, Y., Bennett, D. P., et al. 2017b, AJ, 154, 3

Koshimoto, N., Udalski, A., Sumi, T., et al. 2014, ApJ, 788, 128

Kuijken, K., Bender, R., Cappellaro, E., et al. 2002, The Messenger, 110, 15

Laughlin, G., Bodenheimer, P., & Adams, F. C. 2004, ApJL, 612, L73

Lin, D. N. C.,Bodenheimer, P., & Richardson, D. C. 1996, Nature, 380, 606

Lissauer, J. J. 1993, ARA&A, 31, 129

Mao, S., & Paczynski, B. 1991, ApJL, 374, L37

Marois, C., Macintosh, B., Barman, T., et al. 2008, Science, 322, 1348

Mayor, M., & Queloz, D. 1995, Nature, 378, 355

Metropolis, N., Rosenbluth, A. W., Rosenbluth, M. N., Teller, A. H., & Teller, E. 1953, J. Chem. Phys., 21, 1087

Minniti, D., Lucas, P. W., Emerson, J. P., et al. 2010, New A, 15, 433

Miyake, N., Sumi, T., Dong, S., et al. 2011, ApJ, 728, 120

Montet, B. T., Crepp, J. R., Johnson, J. A., Howard, A. W., & Marcy, G. W. 2014, ApJ, 781, 28

Mróz, P., Udalski, A., Skowron, J., et al. 2017, Nature, 548, 183

Muraki, Y., Han, C., Bennett, D. P., et al. 2011, ApJ, 741, 22

Muterspaugh, M. W., Lane, B. F., Kulkarni, S. R., et al. 2010, AJ, 140, 1657

Nagashima, C., Nagayama, T., Nakajima, Y., et al. 1999, Star Formation 1999, 397

Nagayama, T., Nagashima, C., Nakajima, Y., et al. 2003, Proc. SPIE, 4841, 459

Nataf, D. M., Gould, A., Fouqué, P., et al. 2013, ApJ, 769, 88

Nataf, D. M., Gonzalez, O. A., Casagrande, L., et al. 2016, MNRAS, 456, 2692

Nayakshin, S. 2010, MNRAS, 408, L36

Nelson, J., & Sanders, G. H. 2008, Proc. SPIE, 7012, 70121A

Nishiyama, S., Nagata, T., Tamura, M., et al. 2008, ApJ, 680, 1174-1179 (N08)

Nishiyama, S., Tamura, M., Hatano, H., et al. 2009, ApJ, 696, 1407 (N09)

Paczynski, B. 1986, ApJ, 304, 1

Penny, M. T., Kerins, E., Rattenbury, N., et al. 2013, MNRAS, 434, 2

Penny, M. T., Henderson, C. B., & Clanton, C. 2016, ApJ, 830, 150

Perryman, M., Hartman, J., Bakos, G. Á., & Lindegren, L. 2014, ApJ, 797, 14

Poindexter, S., Afonso, C., Bennett, D. P., et al. 2005, ApJ, 633, 914

Poleski, R., Skowron, J., Udalski, A., et al. 2014, ApJ, 795, 42

Pravdo, S. H., & Shaklan, S. B. 2009, ApJ, 700, 623

Raghavan, D., McAlister, H. A., Henry, T. J., et al. 2010, ApJS, 190, 1

Ryu, Y.-H., Yee, J. C., Udalski, A., et al. 2017, arXiv:1710.09974, accepted in AJ

Safronov, V. S. 1972, Evolution of the protoplanetary cloud and formation of the earth and planets., by Safronov, V. S.. Translated from Russian. Jerusalem (Israel): Israel Program for Scientific Translations, Keter Publishing House, 212 p.,

Sako, T., Sekiguchi, T., Sasaki, M., et al. 2008, Experimental Astronomy, 22, 51

Schneider, P., Ehlers, J., & Falco, E. E. 1992, Gravitational Lenses, XIV, 560 pp. 112 figs.. Springer-Verlag Berlin Heidelberg New York. Also Astronomy and Astrophysics Library,

Schechter, P. L., Mateo, M., & Saha, A. 1993, PASP, 105, 1342

Shvartzvald, Y., Bryden, G., Gould, A., et al. 2017, AJ, 153, 61

Shvartzvald, Y., Yee, J. C., Calchi Novati, S., et al. 2017, ApJL, 840, L3

Shvartzvald, Y., Maoz, D., Kaspi, S., et al. 2014, MNRAS, 439, 604

Shvartzvald, Y., Maoz, D., Udalski, A., et al. 2016, MNRAS, 457, 4089

Siverd, R. J., Beatty, T. G., Pepper, J., et al. 2012, ApJ, 761, 123

Skowron, J., Shin, I.-G., Udalski, A., et al. 2015, ApJ, 804, 33

Skowron, J., Udalski, A., Kozłowski, S., et al. 2016, Acta Astron., 66, 1

Skowron, J., Udalski, A., Poleski, R., et al. 2016, ApJ, 820, 4

Spergel, D., Gehrels, N., Breckinridge, J., et al. 2013, arXiv:1305.5422

Spergel, D., Gehrels, N., Baltay, C., et al. 2015, arXiv:1503.03757

Street, R. A., Udalski, A., Calchi Novati, S., et al. 2016, ApJ, 819, 93

Sumi, T., Abe, F., Bond, I. A., et al. 2003, ApJ, 591, 204

Sumi, T., Bennett, D. P., Bond, I. A., et al. 2010 ApJ, 710, 1641

Sumi, T., Kamiya, K., Bennett, D. P., et al. 2011 Nature, 473, 349

Sumi, T., Udalski, A., Bennett, D. P., et al. 2016, ApJ, 825, 112

Suzuki, D., Bennett, D. P., Sumi, T., et al. 2016, ApJ, 833, 145

Szymański, M. K., Udalski, A., Soszyński, I., et al. 2011, Acta Astron., 61, 83

Tang, J., Bressan, A., Rosenfield, P., et al. 2014, MNRAS, 445, 4287

Tsapras, Y., Street, R., Horne, K., et al. 2009, Astronomische Nachrichten, 330, 4

Udalski, A. 2003, ApJ, 590, 284

Udalski, A., Szymański, M. K., & Szymański, G. 2015, Acta Astron., 65, 1

Udalski, A., Yee, J. C., Gould, A., et al. 2015, ApJ, 799, 237

Verde, L., Peiris, H. V., Spergel, D. N., et al. 2003, ApJS, 148, 195

Ward-Duong, K., Patience, J., De Rosa, R. J., et al. 2015, MNRAS, 449, 2618

Weidenschilling, S. J., & Cuzzi, J. N. 1993, Protostars and Planets III, 1031

Yee, J. C. 2015, ApJL, 814, L11

Yee, J. C., Shvartzvald, Y., Gal-Yam, A., et al. 2012, ApJ, 755, 102

Yee, J. C., Udalski, A., Calchi Novati, S., et al. 2015, ApJ, 802, 76

Yee, J. C., Udalski, A., Sumi, T., et al. 2009, ApJ, 703, 2082

Yoo, J., DePoy, D. L., Gal-Yam, A., et al. 2004, ApJ, 603, 139

Zhu, W., Penny, M., Mao, S., Gould, A., & Gendron, R. 2014, ApJ, 788, 73

Zhu, W., Huang, C. X., Udalski, A., et al. 2017a, PASP, 129, 104501

Zhu, W., Udalski, A., Calchi Novati, S., et al. 2017b, AJ, 154, 210

Zhu, W., Udalski, A., Gould, A., et al. 2015, ApJ, 805, 8

Zhu, W., Udalski, A., Huang, C. X., et al. 2017c, ApJL, 849, L31

Zoccali, M., Renzini, A., Ortolani, S., et al. 2003, A&A, 399, 931